A comprehensive study of the AMR-induced microwave photovoltage, photocurrent and photoresistance in Permalloy microstrips

Dissertation
zur Erlangung des Doktorgrades
des Fachbereiches Physik
der Universität Hamburg

Vorgelegt von
Nikolai Mecking
aus Kiel

Hamburg
2008

Gutachter der Dissertation:	Prof. Dr. Detlef Heitmann Prof. Dr. Can-Ming Hu
Gutachter der Disputation:	Prof. Dr. Detlef Heitmann Prof. Dr. Hans Peter Oepen
Datum der Disputation:	19.03.2008
Vorsitzender des Prüfungsausschusses:	Dr. Tobias Kipp
Vorsitzender des Promotionsausschusses:	Prof. Dr. Günter Huber
Dekan des Fachbereiches für Mathematik, Informatik und Naturwissenschaften:	Prof. Dr. Arno Frühwald

Abstract

We investigate the microwave photovoltage, microwave photocurrent and microwave photoresistance in ferromagnetic thin films and show that these arise primarily from the anisotropic magnetoresistance (AMR). The underlying mechanism is thereby in the case of the microwave photovoltage and photocurrent that the magnetization precession partially rectifies the microwave voltage and current and that in case of the microwave photoresistance the AMR is altered due to the permanent misalignment of the precessing magnetization with respect to its equilibrium direction.

Additionally, in the case of microwave photovoltage there are also spin transfer effects and in the case of microwave photoresistance also the bolometric effect which both compete with the AMR-based effects. While the spin transfer effects only appear at interfaces between ferromagnetic and non-ferromagnetic media, the bolometric photoresistance effect is found to be distinguishable from the corresponding AMR-based effect due to its very different response time to changes in microwave intensity.

The magnetization precession - which is necessary to evoke the AMR-based effects - can be excited by the ferromagnetic resonance (FMR) but also by spin wave resonances. For the case of the FMR a theoretical model is developed which describes the AMR-induced microwave photovoltage as well as the corresponding microwave photoresistance. This enables us to calculate the underlying rf magnetic field vector and its phase with respect to the corresponding rf current. Thereby the phase is found to be directly reflected by the symmetry of the microwave photovoltage's FMR line shape which in magnetic field sweeps. Application in the field of rf magnetic field sensing is discussed.

As already indicated above - beside from the FMR - the microwave photovoltage can also arise from spin wave excitations which we are able to detect with a distinguished sensitivity by means of our experimental setup. Thereby on the one hand standing spin waves perpendicular to our ferromagnetic film are observed and on the other hand confined magnetostatic modes in the film plane are found, especially Damon-Eshbach and Forward-Volume modes. A discussion of the corresponding pinning conditions is also presented. The access to these relatively weak modes is especially meliorated by our use of an all on-chip technique. This is based on embedding our ferromagnetic structures into a coplanar waveguide which emits the microwaves.

Inhaltsangabe

Wir untersuchen die Mikrowellen-Photospannung, den Mikrowellen-Photostrom und den Mikrowellen-Photowiderstand in dünnen ferromagnetischen Filmen. Dabei zeigen wir, dass diese in erster Linie vom anisotropen Magnetowiderstand AMR verursacht werden. Der zugrundeliegende Mechanismus ist für die Photospannung und den Photostroms die partielle Gleichrichtung der Mikrowellen-induzierten Hochfrequenzspannung und des Hochfrequenzstroms durch die präzedierende Magnetisierung. Dagegen entsteht der Photowiderstand aufgrund der Änderung des AMRs durch die permanente Dezentrierung der präzedierenden Magnetisierung.

Zusätzlich gibt es auch noch Spin-Transfer Effekte die Mikrowellen-Photospannung generieren können und den bolometrischen Effekt der zu Mikrowellen-Photowiderstand führen kann. Während die Spin-Transfer Effekte nur an Grenzflächen zwischen ferromagnetischen und nicht-ferromagnetischen Medien auftreten, kann der bolometrische Photowiderstand von dem AMR-basierten aufgrund seiner deutlich anderen Reaktionszeit in Bezug auf Änderungen der Mikrowellenintensität unterschieden werden.

Die Magnetisierungs-Präzession - die für die AMR-basierten Effekte verantwortlich ist - kann sowohl von der ferromagnetischen Resonanz (FMR) als auch von Spinwellen-Resonanzen angeregt werden. Für den Fall der FMR haben wir ein theoretisches Modell entwickelt, dass sowohl die Mikrowellen-Photospannung als auch den Mikrowellen-Photowiderstand beschreibt. Dies ermöglicht uns die Berechnung des zugrundeliegenden Hochfrequenz-Magnetfeld Vektors inklusive seiner Phase in Bezug auf den zugehörigen Hochfrequenzstrom. Dabei wird die Phase direkt von der Symmetrie der FMR-Linienform in Magnetfeld-Sweeps widergespiegelt. Wir diskutieren daher die Anwendung des Effekts im Bereich der Hochfrequenz-Magnetfeld Detektion.

Wie bereits oben erwähnt, kann die Mikrowellen-Photospannung nicht nur durch die FMR sondern auch durch Spinwellen erzeugt werden. Diese detektieren wir speziell aufgrund der besonders guten Sensitivität unseres Messaufbaus. Wir finden zum einen stehende Spinwellen senkrecht zu unserem ferromagnetischen Film und zum anderen magnetostatische Moden, die in der Film-Ebene räumlich eingeschränkt sind, speziell Damon-Eshbach und Forward-Volume Moden. Wir diskutieren die zugrundeliegenden Pinning-Bedingung. Der Zugang zu diesen relativ schwachen Moden wurde speziell durch die Nutzung einer vollstänigen On-Chip Technik verbessert, für die wir unsere ferromagnetische Struktur in einen koplanaren Wellenleiter einbetten.

Contents

Chapter 1

Introduction

This work is dedicated to the investigation of the impact of microwave radiation on the dc electric properties of ferromagnetic thin films. Following Ohm's law there are three major electric quantities in normal conductors: voltage, current and resistance. As will be shown in this work all three can be manipulated in ferromagnetic films by external microwave radiation. In analogy to the language of infrared spectroscopy we will call the resulting effects microwave photovoltage, microwave photocurrent and microwave photoresistance to avoid confusion with the also present microwave induced rf voltage, rf current and the corresponding resistance.

The motivation for our work arises from the subject of spintronics, which is devoted to the investigation of electronic transport manipulation by means of the electronic spin. A special ambition is thereby the so-called spin-transistor [1]. In this context ferromagnetic materials are of crucial interest because they exhibit the valuable property of having an intrinsic spin polarization whose impact on the transport properties is described in terms of the magnetoresistive effects. These have already made their way into standard technical applications, especially in the case of the giant magnetoresistance (GMR) [2], which is for example used in hard disc read heads today and whose discoverers were honored with the Nobel-price in 2007.

A naturally arising question is now what happens to the dc electronic transport if the spin properties are no longer temporarily constant. This can be tackled by exciting the spins to precess around their equilibrium alignment. These excitations become resonant in the microwave frequency range, namely the ferromagnetic resonance and spin waves. Numerous groups have dedicated their work to the subject of dc effects in microwave-exposed ferromagnetic films [3–15] whereby most publications concentrate on the lateral transport through ferromagnetic films. However, for example Tulapurkar *et al.* [3] and Sankey *et al.* [4] investigated successfully the vertical transport

through ferromagnetic/normal metal multilayer structures with microwaves thereby realizing the concept of the spin-torque diode.

Concerning single layer ferromagnetic metal structures the first investigations were already performed four decades ago [5, 6] and resulted in the rectification of the microwave voltage in Nickel films by means of the FMR and later also by means of spin wave resonances [7]. Recently new interest has arisen along with the concept of spin pumping [16–19] which is visualizable by spin transfer effects in lateral microwave photovoltage experiments in hybrid ferromagnetic/normal metal devices [8, 10]. However, a major problem is to distinguish this effect from the anisotropic magnetoresistance (AMR)-based rectification which was already identified as the reason for the microwave photovoltage in the very early works [5–7]. An approach to explain both effects based on a consistent model was published recently by Kupferschmidt *et al.* [20]. In the present work we will have a focus on the microwave photovoltage and photocurrent from AMR-based rectification.

Indeed, there is yet another conformance which can be addressed in a single comprehensive model and which we will outline in this work, namely the conformance of the photovoltage from AMR-rectification with the AMR-based microwave photoresistance which was discovered recently by Costache *et al.* [14] and competes with the bolometric photoresistance [15, 21] that for example also appears in semiconductors [22] and was the original motivation for this work.

The photoresistive effects in semiconductors have been deeply investigated for long time by means of far-infrared light in our group. Thereby they provided us with a distinguished understanding of the underlying physics as featured in several publications [22–25]. This gave us a broad experience whose application on the subject of microwave-induced dc effects in ferromagnetic films provided us with the distinguished access which will be presented in this work and which accents our results compared to that of other groups.

Starting from the beginning of our work we have identified many microwave dc effects which can be either categorized as bolometric like their analogs in semiconductors or as AMR-based spin rectification which is special to ferromagnetic conductors. Although these effects were already sporadically featured in several publications [5–7,12–14] there was no comprehensive picture established concerning their general nature and no awareness of their importance. We have therefore issued a line of publications whose aim is to shed light onto the field.

In publication P2 (see section 6.1.1) we have demonstrated the exceptional properties of the AMR-based microwave photocurrent and photovoltage from spin-rectification in ferromagnetic films whereby also the compari-

son to corresponding effects in semiconductors is established. In publication P3 (see section 6.2.1) we have demonstrated the usability of the microwave photovoltage for the detection of an exceptionally broad range of spin wave resonances. Thereby an emphasis is put on the determination of the corresponding pinning conditions. In publication P4 (see section 6.3) the bridge is build to the bolometric photoresistance which is compared to the corresponding AMR-based effect and for which a response time-based method to distinguish the two is lined out. For the results in publications P2,P3 and P4 normally magnetized ferromagnetic films were used.

As a quintessence in publication P1 (see section 5.1) a theoretical model for a comprehensive analytical understanding of the microwave photovoltage, photoresistance and photocurrent is established whereby the reproducibility of the theoretical results is documented by its comparison to microwave photovoltage and photoresistance results which have been obtained in in-plane magnetized ferromagnetic films. Thereby a focus was on the fact that the microwave photovoltage can be used to detect the microwaves' magnetic field vector at the film stripe's position and also to detect its phase. This is discussed in the context of application in radio-frequency magnetic field sensing and verified in detail in a further publication [26].

The theory presented in publication P1 describes consistently both, the AMR-induced microwave photovoltage and the AMR-induced microwave photoresistance whereby indeed the underlying formalism is so general that it might be even used to describe the reverse effect of the microwave photovoltage, namely the generation of an rf voltage from a dc current in the presence of magnetization precession. This has been investigated recently by Kisilev *et al.* [27] in ferromagnetic films.

As indicated above in the time, during which this work was prepared, its results where gradually published in various physics journals and most of these publications are hence integrated into the present work to provide a comprehensive compendium. The measurement results where primarily derived in the group of Prof. Dr. Can-Ming Hu at the University of Manitoba in Winnipeg, Canada during a one-year stay abroad which was enabled by the Deutsche Akademische Austauschdienst DAAD.

This work is organized as follows: In section 2 the theoretical fundamentals of the anisotropic magnetoresistance AMR, of the ferromagnetic rf susceptibility and of the spin wave resonances are discussed. In section 3 and 4 the preparation of our ferromagnetic thin film structures and the setup of our experiments are described. In section 5 we present the experimental results concerning in-plane magnetized ferromagnetic films and in section 6 and 6.3 those concerning microwave photocurrent, photovoltage and photoresistance in normally magnetized ferromagnetic films. Finally in section 7 a

summary and outlook are provided.

Chapter 2

Theoretical Background

2.1 Ferromagnetism

A medium is ferromagnetic when exhibiting a permanent magnetic moment below its Curie temperature T_C [28]. The reason for the magnetic moment is global electronic spin alignment which arises if parallel spin alignment with respect to the neighboring atoms' spins is energetically favorable. The mechanism behind this is the exchange interaction. This arises from the Pauli principle which states that electrons of identical spin alignment cannot enter the same quantum state. In principle this means that if the spins of two neighboring electrons are aligned the electrons have to have an antisymmetric wave function to fulfill the Pauli principle. For electrons an antisymmetric wave function is usually energetically favorable because its probability distribution in the middle of the two single wave functions is especially low. Therefore the electrons are in average farer away from each other and their potential energy from Coulomb interaction decreases. There are, however, also cases in which a symmetric wave function is energetically favorable wherefore antiparallel spins are necessary. This is the case for antiferromagnetic materials. The result of the local favoritism of parallel spin alignment is global spin $\mathbf{s}$ alignment and hence also global alignment of all spins' magnetic moments $\mu = \frac{ge}{2m_e}\mathbf{s}$. Thereby e is the electron charge, m_e is the electron mass and g is the Landé g-factor with $g \approx 2$ for free electrons and $\gamma = \mu_0 \frac{ge}{2m_e}$ is called the gyromagnetic ratio. It is worth noting that, however, in large (macroscopic) scale ferromagnetic specimens the spins are not globally aligned but only locally within certain domains [28].

On the microscopic scale where all spins are aligned the strength of the magnetic moment, and therefore also that of the magnetization $\mathbf{M}$ which is the magnetic moment per volume, is constant: $|\mathbf{M}| = M_0$. Hence only the

direction of **M** can be changed what can be done directly by an external magnetic field with which the magnetization tries to align. However the crystal structure and shape of a ferromagnetic specimen are also decisive for its magnetization direction. This can be described in terms of easy and hard axis with the magnetization trying to align preferably with the easy axis. In the experiments presented in this work we use the external relatively strong magnetic fields that globally align all spins and so suppress the formation of a domain structure.

Elements exhibiting ferromagnetism above room temperature are Nickel, Iron and Cobalt. There is however also Gadolinium which has a Curie temperature of $T_C \approx 290$ K and several compound materials like CrO_2 for which T_C lies above room temperature. In this work we investigate Permalloy, an alloy of Nickel and Iron with the ratio 4 to 1. It is special in showing almost no crystalline anisotropy, almost no anomalous Hall effect and no magnetostriction [29] and thus provides us with a comfortably simple system to probe general characteristics of ferromagnetic media. The Landé g-factor in Permalloy is close to that of free electrons: $g \approx 2$. From this $\gamma \approx \mu_0 \cdot 176$ GHz/T follows. A detailed discussion of the microphysical origins of ferromagnetism can be found for example in the work of Morrish [29].

In the following we will continue with discussing the magnetoresistance effects in ferromagnetic materials, which describe the impact of the global spin alignment on the charge transport properties.

2.2 Anisotropic Magnetoresistance and Anomalous Hall Effect

The anisotropic magnetoresistance [30] (AMR) is found in ferromagnetic conductors and effects different resistivities parallel and perpendicular to the magnetization axis. The resistivity $\rho_0 + \rho_A$ parallel to the magnetization axis is usually higher than that (ρ_0) perpendicular to the magnetization. This means that when rotating the magnetization of a ferromagnetic conductor of length L, width W and thickness d this has maximal resistance $R_0 + R_A = (\rho_0 + \rho_A) \cdot (L/(d \cdot W))$ when the magnetization is aligned or antialigned to it and minimal resistance $R_0 = \rho_0 \cdot (L/(d \cdot W))$ when the magnetization lies perpendicular to it. The AMR can be described by a resistivity tensor $\hat{\rho}$. For this we define an orthogonal coordinate system with the z-axis aligned to the magnetization:

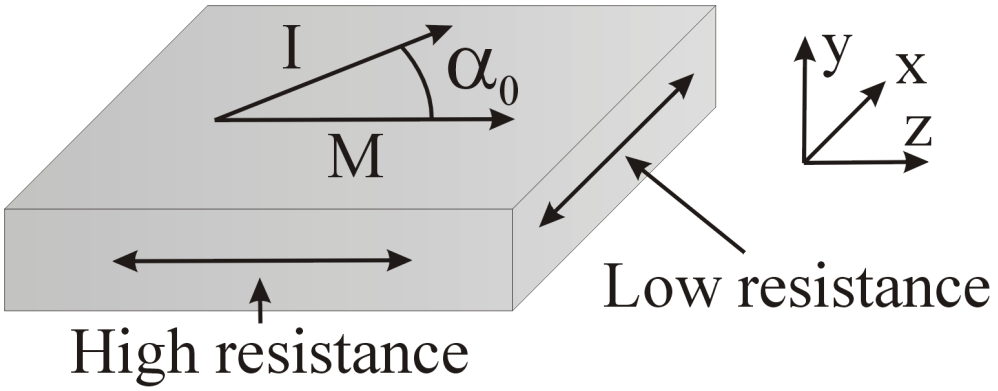

Figure 2.1: Geometry of the AMR in ferromagnetic films: The resistance parallel and antiparallel to the magnetization is higher than the resistance perpendicular to it. We define our coordinate to have the z-axis aligned to the magnetization, the y-axis aligned to the film normal and the x-axis perpendicular to both. A current $\mathbf{I} = (I \sin\alpha_0, 0, I \cos\alpha_0)$ of arbitrary direction within the film plane is considered. It encloses the arbitrary angle α_0 with the magnetization. In real films we define the current direction by means of photolithography as described in section 3.

$$\hat{\rho} = \begin{pmatrix} \rho_0 & 0 & 0 \\ 0 & \rho_0 & 0 \\ 0 & 0 & \rho_0 + \rho_A \end{pmatrix} \tag{2.1}$$

We consider a current density $\mathbf{J} = (J \sin\alpha_0, 0, J \cos\alpha_0)$ that encloses the angle α_0 with the magnetization $\mathbf{M}$ (and thus also with the z axis). The electric field is hence $\mathbf{E} = \hat{\rho}\mathbf{J} = (\rho_0 J \sin\alpha_0, 0, (\rho_0 + \rho_A) J \cos\alpha_0)$. Its component along the current $\mathbf{I}$ direction is ($\mathbf{I} = \mathbf{J} \cdot d \cdot W$):

$$E_L = \frac{\mathbf{E} \cdot \mathbf{J}}{J} = \frac{1}{J} \cdot \begin{pmatrix} \rho_0 J \sin\alpha_0 \\ 0 \\ (\rho_0 + \rho_A) J \cos\alpha_0 \end{pmatrix} \cdot \begin{pmatrix} J \sin\alpha_0 \\ 0 \\ J \cos\alpha_0 \end{pmatrix} = (\rho_0 + \rho_A \cos^2\alpha_0) \cdot J \tag{2.2}$$

From this we can calculate the longitudinal voltage drop $U_L = E_L \cdot L = (R_0 + R_A \cos^2\alpha_0) \cdot I$ along the current direction ($I = |\mathbf{I}|$). There appears also an electric field perpendicular to the current direction which also lies in the current-magnetization-(x-z-)plane. This corresponds to the in-plane Hall effect [31]:

$$\mathbf{E}_{IPHE} = \mathbf{E} - \frac{E_L}{J} \cdot \mathbf{J} = \rho_A J \sin\alpha_0 \cos\alpha_0 \begin{pmatrix} -\cos\alpha_0 \\ 0 \\ \sin\alpha_0 \end{pmatrix} \tag{2.3}$$

In contrast to the anomalous Hall effect which will be explained hereafter the in-plane Hall effect needs a magnetization component within the current-voltage plane.

The microphysical origin of the AMR is the fixed spin orientation in ferromagnetic materials which breaks the otherwise spherical symmetry of the total of the electrons' atomic orbitals and reduces it to cylindrical symmetry around the magnetization axis. Consequently the scattering cross section of the electrons, which is defined by their orbitals, is different parallel and perpendicular to the magnetization and so is the corresponding electric resistivity.

An effect that usually comes along with the AMR is the anomalous Hall effect (AHE). This adds two transversal components ρ_{AHE} within the x-y plane to the resistivity tensor in equation (2.1) [32]:

$$\hat{\rho} = \begin{pmatrix} \rho_0 & -\rho_{AHE} & 0 \\ \rho_{AHE} & \rho_0 & 0 \\ 0 & 0 & \rho_0 + \rho_A \end{pmatrix} \tag{2.4}$$

Its major difference compared to the normal Hall effect [28] which is found in every conductor is that it depends on the magnetization direction instead of on the strength of the static magnetic field H and that the AHE is much stronger than the normal Hall effect which can consequently in ferromagnetic materials only be observed at high $|H|$ because there the magnetization is constantly aligned to the magnetic field. Consequently no change of the superposing AHE can be observed anymore when changing H. However in the Permalloy which is generally used in this work the AHE is especially weak.

2.3 Giant and Tunneling Magnetoresistance

Even stronger magnetoresistive effects than the AMR and AHE, which usually exhibit a strength ($R_A/R_0 = \rho_A/\rho_0$ and ρ_{AHE}/ρ_0 respectively) in the order of some percent of the minimal resistance R_0, can be found in ferromagnetic multilayer structures. Especially famous examples are the giant magnetoresistance [2] (GMR) and the tunneling magnetoresistance (TMR). For both the basic principle is that a spin polarized current is flowing between two ferromagnetic layers through a very thin intermediate non-ferromagnetic

layer which is in case of the GMR metallic and in case of the TMR isolating. The effect occurs because of vertical currents being subject to a lower resistance in the case of alignment of the two ferromagnetic layers' magnetizations compared to the case of misalignment. This way high magnetization-induced resistance changes of several 10 % can be reached by GMR and TMR. This is why these effects are not only of academic but also of vast technical interest as they are for example applicable in hard disc read heads.

2.4 Dynamic Susceptibility in Ferromagnetic Media

In order to understand the dynamic properties of our ferromagnetic medium a semiclassical approach by means of the Landau-Liftshitz equation [34] is used. It addresses the fact that the magnetic field $\mathbf{H}$ applies a torque on the magnetization $\mathbf{M}$ what causes $\mathbf{M}$ to precess around the direction of $\mathbf{H}$ at the frequency of the ferromagnetic resonance (FMR):

$$\frac{d}{dt}\mathbf{M} = \gamma \mathbf{H} \times \mathbf{M} \tag{2.5}$$

In the equilibrium case: $\mathbf{M}_0 \parallel \mathbf{H}$ (if $|\mathbf{H}$ is high enough). Following the definition of our coordinate system $\mathbf{M}_0$ and $\mathbf{H}$ are hence lying along the z axis. However leaving this position by the small perturbation $\mathbf{m}_0 \perp \mathbf{M}_0$ results in a torque $\gamma \mathbf{H} \times \mathbf{m}_0$ that is applied to $\mathbf{M}$, so that the time-dependence of $\mathbf{M}$ becomes (in the case of an unlimited ferromagnetic medium): $\mathbf{M} = \mathbf{M}_0 + \mathbf{m}_0 \cos(\omega_r t) - \mathbf{z} \times \mathbf{m}_0 \sin(\omega_r t)$ with $H = |\mathbf{H}|$, the unit vector $\mathbf{z} \parallel \mathbf{M}$ along the z axis and $\omega_r = \gamma H$ the FMR frequency (in first order approximation $\mathbf{m}_0$ can only lie perpendicular to $\mathbf{M}_0$ because the length of $\mathbf{M}$ is constant).

To find the specimen's susceptibility an additional radio-frequency (rf) magnetic field $\Re(\mathbf{h}^{in} e^{-i\omega t})$ is added to the static magnetic field $\mathbf{H}$ inside the specimen: $\mathbf{H}_{total} = \mathbf{H} + \Re(\mathbf{h}^{in} e^{-i\omega t})$. It oscillates at the microwave frequency ω and has the complex amplitude $\mathbf{h}^{in} = (h_x^{in}, h_y^{in}, h_z^{in})$. Its real and imaginary part represent its contributions oscillating in-phase and 90° out-of-phase with respect to $\mathbf{m}_0 \cos(\omega t)$. $\mathbf{M}$ is then forced to precess with the frequency of the exciting field. Its precession can also be described by the complex vector $\mathbf{m} = (\mathbf{m}_0 - i\mathbf{z} \times \mathbf{m}_0) = (m_x, m_y, m_z)$ with $\mathbf{M} = \mathbf{M}_0 + \Re(\mathbf{m} e^{-i\omega t})$. Hence equation (2.5) becomes:

$$\frac{d}{dt}\mathbf{m} = \gamma(\mathbf{H} \times \mathbf{m} + \mathbf{h}^{in} \times \mathbf{M}) = \gamma \mathbf{z} \times (H\mathbf{m} - M_0 \mathbf{h}^{in}) \tag{2.6}$$

This can be resolved into three equations:

$$\begin{aligned} -i\omega m_x + \gamma H m_y &= \gamma M_0 h_y^{in} \\ -i\omega m_y - \gamma H m_x &= -\gamma M_0 h_x^{in} - i\omega m_z = 0 \end{aligned} \tag{2.7}$$

Solving these gives:

$$\mathbf{m} = \hat{\chi}\mathbf{h^{in}} = \begin{pmatrix} \chi_L & i\chi_T & 0 \\ -i\chi_T & \chi_L & 0 \\ 0 & 0 & 0 \end{pmatrix} \mathbf{h^{in}} \tag{2.8}$$

with

$$\chi_L = \frac{\omega_M \omega_r}{\omega_r^2 - \omega^2},\ \chi_T = \frac{\omega \omega_M}{\omega_r^2 - \omega^2}$$

and $\omega_M = \gamma M_0$. This is the Polder-tensor [35] which describes the rf magnetization inside a ferromagnetic medium.

2.5 Ferromagnetic Resonance in Thin Films

Although the Polder-tensor (equation (2.8)) is still valid inside thin ferromagnetic films, their FMR frequency changes due to the boundary conditions of the magnetic field at the film surface. The cases with the equilibrium magnetization $\mathbf{M}_0$ in the film plane and normal to it are different because in the case that $\mathbf{H}$ and hence $\mathbf{M}_0$ lie normal to the film plane, $\mathbf{B}$ (and not $\mathbf{H}$) is continuous at the film surface [36] and the internal magnetic field $\mathbf{H}^{in}$ inside the film is only $\mathbf{H}^{in} = \mathbf{H} - \mathbf{M}_0$. The impact on the FMR will be discussed in section 2.5.2. In contrast if $\mathbf{H}$ and hence $\mathbf{M}_0$ lie in the film plane $\mathbf{H}$ is continuous at the surface: $\mathbf{H}^{in} = \mathbf{H}$.

The boundary conditions for the rf magnetic field (inside the film $\mathbf{h}^{in}$ and outside $\mathbf{h} = (h_x, h_y, h_z)$) are the same as for the static field $\mathbf{H}$: The $\mathbf{h}$ components parallel and that of the magnetic induction $\mathbf{b}$ perpendicular to interfaces are continuous. However because only the components perpendicular to $\mathbf{H}$ matter the case of continuity now corresponds to the case of the magnetization lying normal to the ferromagnetic film. For our geometrical understanding we define the y axis of our coordinate system to lie normal to

the film plane, while the z axis is still aligned to the magnetization. In the in-plane magnetization case then discontinuity of h_y becomes relevant and like in the normal magnetization case also here the FMR frequency changes compared to the infinite medium case.

2.5.1 With In-Plane Magnetization

The discontinuous h_y results in elliptical precession of the magnetization and thus an increase in resonance frequency compared to the bulk material case with $\omega = \gamma H$. This becomes now:

$$\omega = \gamma\sqrt{H(H + M_0)} \tag{2.9}$$

Using this we find the resonance magnetic field:

$$H_0 = \sqrt{\frac{M_0^2}{4} + \omega^2/\gamma^2} - \frac{M_0}{2} \tag{2.10}$$

A detailed derivation of the resonance frequency and the corresponding susceptibility can be found in publication P1 presented in section 5.1.

2.5.2 With Normal Magnetization

Because of the rotational symmetry of an infinite film around its normal, the magnetization precession becomes circular when its equilibrium direction lies also normal the ferromagnetic film, in this case the rf magnetic field which lies perpendicular to the equilibrium magnetization which excites the FMR is continuous at the film surface. Therefore $\omega = \gamma H^{in}$. Because $B = \mu_0 H = \mu_0(H^{in} + M_0)$ is continuous at the film surface the magnetic field inside the ferromagnetic film becomes $H^{in} = H - M_0$. The FMR resonance condition can hence be described by the Kittel equation [33] for perpendicularly magnetized ferromagnetic planes:

$$\omega = \gamma(H - M_0) \tag{2.11}$$

Conclusively the resonance magnetic field is:

$$H_0 = M_0 + \omega/\gamma \tag{2.12}$$

This equation only applies for $H > M_0$, otherwise the magnetization is not

bent normal to the film, what is necessary to generate the conditions under which the Landau-Liftshitz equation (2.5) can be applied. This means that magnetic fields above $M_0 \approx 1$ T have to be generated in this case for Permalloy.

Although being a similarly simple example as the in-plane magnetized ferromagnetic film in section 2.5.1 the normally magnetized ferromagnetic film exhibits a special problem concerning the microwave photovoltage. This we use as a primary detection mechanism in this work. It is described in detail in publication P1 in section 5.1: The photovoltage vanishes if **M** and **I** are perpendicular. Hence the microwave photovoltage can only be observed when tilting the magnetization slightly with respect to the film perpendicular. In this case however the calculation of the FMR frequency by means of the Kittel formalism [33] is rather challenging because the equilibrium magnetization no longer lies along the principle axis of an ellipsoid. This is because a plane is a special case of an ellipsoid with the principle axis lying in-plane and normal to it. Therefore the obligatory magnetization bend for microwave photovoltage measurements renders the Kittel equation [33] only approximately applicable for our case. Consequently a comprehensive but plain theoretical analysis of the angle dependence of the microwave photovoltage - like that done in publication P1 for the in-plane case - is harder to be performed for an out-of-plane magnetization.

2.6 Spin Waves

Beside the FMR, which is characterized by a uniform precession of the individual spins all across the ferromagnetic medium, also other ferromagnetic excitations exist with spatially inhomogeneous magnetization precession which take the form of spin waves, meaning of waves of with spatially alternating spin precession phase. Thereby the misalignment of nearby spins in the context of the spin waves usually necessitates additional energy compared to the FMR (however, especially in the case of magnetostatic Backward-Volume modes for certain wave vectors a lower energy is found compared to that of the FMR). This compensates on the one hand for the increasing exchange energy from misalignment of neighboring spins and accounts on the other hand for the arising dipole-dipole interaction. For long spin wavelength dominantly the additional energy is dominantly due to the dipole-dipole interaction and for short wavelength due to exchange interaction. Confinement of the spin waves results in standing spin waves. Indeed because of the spin wave's generally much shorter wavelength (in the order of nm or μm) compared to that of electromagnetic waves of the same frequency (in the order

of cm) only standing spin waves can be excited because otherwise momentum conservation is not possible. However, it is also possible to investigate travelling spin waves. These can be addressed by means of their wave vector in Brillouin light-scattering experiments making use of electromagnetic radiation with much shorter wavelength (infrared/visible light) and hence much longer wave vector [37].

In thin ferromagnetic films the exchange and dipole-dipole interaction based spin waves coincide with two generally distinct geometrical cases: Standing spin waves perpendicular to the film (short wavelength, exchange interaction dominant) and standing spin waves with an in-plane wave vector (long wavelength, dipole-dipole interaction dominated). Also accounting for the impact from the magnetization direction (in-plane or normal to the film and parallel or perpendicular to the wave vector) on the two kinds of spin waves we get in total five distinct cases of which we will however only analyze four in this work because the Backward-Volume modes was not observed in our experiments. The five kinds of spin waves are:

1. Standing spin waves perpendicular to the ferromagnetic film plane with the magnetization also perpendicular to the plane (theory in section 2.7.2, measurements in publication P2 and P3 in section 6.1.1 and 6.2.1 respectively).

2. Standing spin waves perpendicular to the ferromagnetic film plane with the magnetization in-plane (theory in section 2.7.1, measurements in section 5.3).

3. Standing spin waves within the ferromagnetic film plane with the magnetization perpendicular to the film (Forward-Volume modes, theory in section 2.8.2, measurements in publication P3 in section 6.2.1).

4. Standing spin waves within the ferromagnetic film plane with their wave vector perpendicular to the in-plane magnetization (Damon-Eshbach modes, theory in section 2.8.1 and measurements in section 5.4).

5. Standing spin waves within the ferromagnetic film plane with their wave vector parallel to the in-plane magnetization (Backward-Volume modes with negative dispersion and thus lower energy than the FMR, these are not discussed in this work).

A sketch of these different kinds of spin waves can be found in figure 2.2 and figure 2.3.

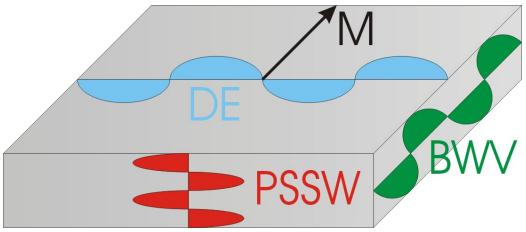

Figure 2.2: Sketch showing the forth order of different kinds of standing spin waves for $K = 0$ as pinning condition in an in-plane magnetized ferromagnetic film. PSSW: Perpendicular standing spin wave (wave vector perpendicular to the film). DE: Damon-Eshbach mode (wave vector in the film plane but perpendicular to the magnetization **M**). BWV: Backward volume mode (wave vector in the film plane parallel to the magnetization **M**). Note that all these modes also have to have wave vectors along the two other dimensions, too, due to the actually three-dimensional confinement. However, these are conventionally of lowest order and therefore not displayed here.

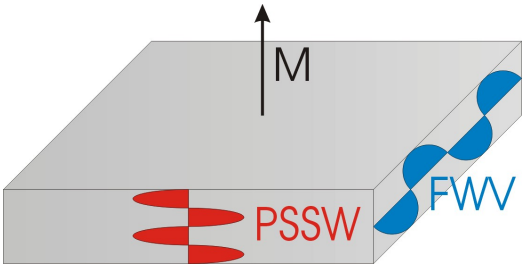

Figure 2.3: Sketch showing the forth order of different kinds of standing spin waves for $K = 0$ as pinning condition in a normally magnetized ferromagnetic film. PSSW: Perpendicular standing spin wave (wave vector perpendicular to the film). FWV: Forward volume mode (wave vector in the film plane perpendicular to the magnetization **M**). Note that all these modes also have to have wave vectors along the two other dimensions, too, due to the actually three-dimensional confinement where no bellies and knots are displayed. These are conventionally of lowest order and therefore not displayed here. However modes with simultaneously normal and in-plane wave vectors of higher order, which are usually only observed separately, are are found and presented in publication P3.

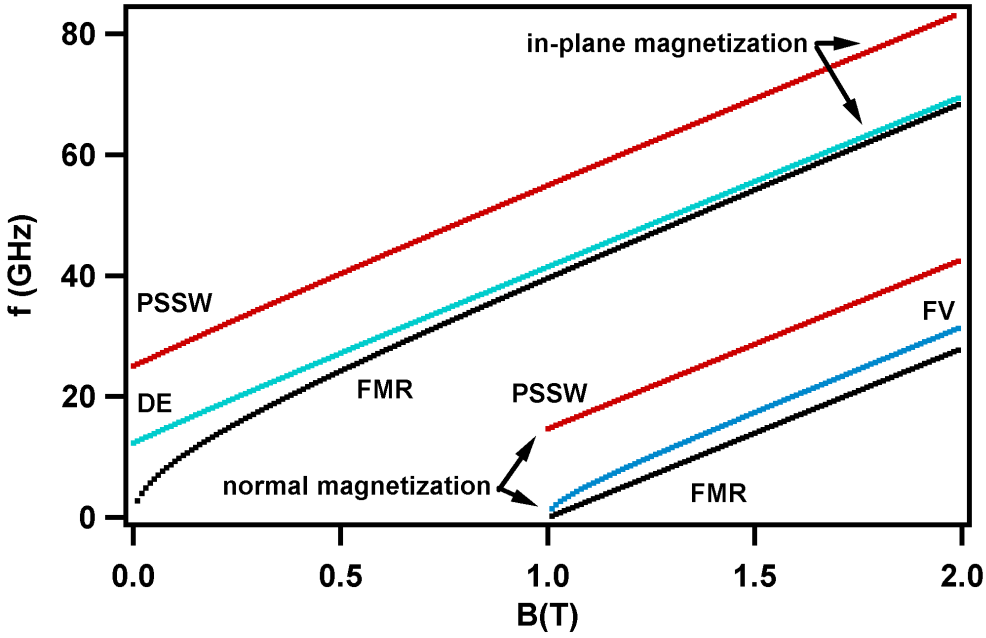

Figure 2.4: Plot of the magnetic field $H = B/\mu_0$ dependence of the frequency f of the FMR, perpendicular standing spin waves (PSSW) and magnetostatic modes (Damon-Eshbach modes (DE) and Forward-Volume modes (FV)) for in-plane and normally magnetized ferromagnetic films (see equations (2.10), (2.12), (2.18), (2.20), (2.24) and (2.29)). The parameters used are $M_0 = 1$ T, $\gamma = 176$ GHz/T, $A = 1.22 \cdot 10^{-11}$ N, $d = 12$ nm and $W = 50$ nm. These relatively small geometrical dimensions compared to those of the film stripes investigated in this work are chosen to enlarge the spacing of the spin wave modes from the FMR. It has to be noted that - although it will be ignored here for demonstrative purposes - in principle the impact from exchange on the Demon-Eshbach and Forward-Volume modes has to be minded, too. An interesting fact that becomes visible is that the Damon-Eshbach mode frequency approaches that of the FMR when increasing the magnetic field while for Forward-Volume modes the frequency difference compared to the FMR increases. This is also confirmed in our experiments (see section 5.4 and publication P3).

2.6.1 Pinning Condition

An additional important point concerning confined spin waves is their pinning conditions, meaning their boundary conditions at the confining interfaces of the ferromagnetic medium. In contrast to, for example, electromagnetic radiation, where the components of **H** parallel and that of **B** perpendicular to interfaces are continuous, for spin waves no such general boundary condition exists. Instead the boundary (pinning) condition depends very sensitively on the exact configuration of the interface (e.g. because of the presence of an antiferromagnetic oxide layer with fixed spin configuration). In our case this makes the pinning condition an unknown parameter. Defining the interface to lie normal to the y axis a general ansatz can be made by describing the pinning condition as [41]:

$$\mathbf{m} + K \cdot \frac{d\mathbf{m}}{dy} = 0 \tag{2.13}$$

where K is the fitting parameter which defines the pinning condition. A more detailed discussion concerning the pinning condition of perpendicular standing spin waves and confined Forward-Volume modes can be found in publication P3 in section 6.2.1.

We will describe now the magnetic field dependencies of the different spin wave modes enlisted above and want to point out their important properties (compare also figure 2.4). Especially the resonance frequency of exchange dominated spin waves with a wave vector of the length k can be easily calculated using the exchange stiffness A of the medium which reflects the strength of the magnetic field that arises from spatial rotation of the magnetization. Besides, the consideration of the FMR as a uniform mode discussed at the beginning of section 2.6, where the magnetization precesses everywhere with the same amplitude and phase is only possible for $K \to \infty$. This is in general an acceptable consideration for Permalloy films [38].

2.7 Standing Spin Waves Perpendicular to Ferromagnetic Films (Exchange Interaction Dominated)

The wavelength of standing spin waves perpendicular to a thin ferromagnetic film is obviously very short (nm-range) and therefore the exchange interaction becomes the dominant correction to the Landau-Liftshitz equation in this case. The exchange field of these spin wave modes arises from the tried

revoking of the misaligned of neighboring spins according to the basic principles of ferromagnetism and can be described on a macroscopic level by a Laplace operator ∇^2 based exchange interaction term [39] on the right side of the Landau-Liftshitz equation (2.5):

$$\frac{d}{dt}\mathbf{M} = \gamma\mathbf{H} \times \mathbf{M} + \frac{2A}{\mu_0 M_0^2}(\nabla^2\mathbf{M}) \times \mathbf{M} \tag{2.14}$$

whereby A is the exchange stiffness of the ferromagnetic medium. Considering that the rf magnetization $\mathbf{m} = \mathbf{M} - \mathbf{M}_0$ is a plane wave $\mathbf{m} \propto e^{-i\mathbf{kr}}$ the term becomes: $-\gamma(2A/\mu_0 M_0^2)(k^2\mathbf{m}) \times \mathbf{M}_0$, where $k = |\mathbf{k}|$. Thus:

$$\frac{d}{dt}\mathbf{m} = \gamma((\mathbf{H} + \frac{2Ak^2}{\mu_0 M_0^2}\mathbf{M}_0) \times \mathbf{m} + \mathbf{h} \times \mathbf{M}_0) \tag{2.15}$$

Consequently the change in the Landau-Liftshitz equation is limited to a correction $+\gamma(2Ak^2/\mu_0 M_0^2)\mathbf{M}$ which is added to $\mathbf{H}$ in equation (2.6). Hence the equation for the standing spin waves can be simply derived by replacing $\mathbf{H}$ by $\mathbf{H} + \gamma(2Ak^2/\mu_0 M_0)\mathbf{M}$. Because $\mathbf{H}$ and $\mathbf{M}_0$ are parallel the correction term

$$H_S = \gamma(2Ak^2/\mu_0 M_0) \tag{2.16}$$

can be directly subtracted from the resonance field H_0 of the FMR to find the PSSW's resonance frequency. The exchange dominated spin waves have therefore a lower resonance field compared to the FMR but their resonance frequency is analogously higher, meaning that additional energy is needed to excite them.

2.7.1 Modes in In-Plane Magnetized Films

As derived above the resonance condition of perpendicular standing spin waves with in-plane static magnetization $\mathbf{M}_0$ can be found by replacing H by $H + H_S$ in the corresponding equation (2.9) for the FMR [38]:

$$\omega = \gamma\sqrt{(H + M_0 + H_S)(H + H_S)} \tag{2.17}$$

From this we can calculate the resonance magnetic field $H_{0,PSSW}$ for the exciting microwave frequency ω:

$$H_{0,PSSW} = \sqrt{\frac{M_0^2}{4} + \omega^2/\gamma^2} - M_0/2 - H_S \tag{2.18}$$

The magnetic field spacing of the standing spin waves with respect to the FMR is $-H_S$ as already found above and therefore proportional to the square of their wave vector k. However for standing spin waves in a confinement the k-vector is limited to certain values, e.g. for $K \to 0$ or $K \to \infty$ pinning to integer n multiples of π/d, where d is the width of the confinement, in our case the thickness of the ferromagnetic film. So $H_S = A\pi^2 n^2/\mu_0 M_0 W^2$ and the difference in resonance field compared to the FMR scales with the square of the order n of the resonance.

2.7.2 Modes in Normally Magnetized Films

The resonance condition of standing spin waves confined normal to a normally magnetized ferromagnetic film can be found like above by replacing H by $H + H_S$ in the corresponding equation (2.11) for the FMR [28]:

$$\omega = \gamma(H + H_S - M_0) \tag{2.19}$$

and consequently we find the resonance field:

$$H_{0,PSSW} = \omega/\gamma + M_0 - H_S \tag{2.20}$$

This means that the difference in magnetic field of the standing spin wave resonances with respect to the FMR is again $-H_S$ like in the in-plane magnetization case, but due to the linear magnetic field dependence of the FMR now also the frequency difference of the spin waves with respect to the FMR is linear in H_S and thus in k^2, whereby k is again limited to certain discrete values which are defined by the pinning condition like above in the in-plane magnetization case.

2.8 Spin Waves in the Ferromagnetic Film Plane (Dipole-Dipole Interaction Dominated Magnetostatic Modes)

Beside the previously discussed spin waves perpendicular to our ferromagnetic film also spin waves with their wave vector within the film plane can

be generated. These have a much longer wavelength due to the much larger dimensions of our film stripe structures in this direction. That is why the short-ranged exchange interaction can be neglected when calculating their resonance frequency which is hence only determined by dipole-dipole interaction and much closer to the FMR frequency.

The dipole-dipole interaction dominated modes can be described analytically using a magnetostatic approximation. This is based on the Maxwell equation:

$$\nabla \times \mathbf{h} = d\mathbf{D}/dt + \mathbf{J} \tag{2.21}$$

whereby the limited dimensions of our ferromagnetic medium render propagation effects negligible and hence the right side vanishes [40]. Consequently $\nabla \times \mathbf{h} = 0$ and a regime similar to that in magnetostatics is found. As a consequence we can describe $\mathbf{h} = \nabla\Psi$ by the scalar potential Ψ. Then from the Maxwell equation $\nabla\mathbf{b} = 0$ follows

$$0 = \nabla(1 + \hat{\chi})\nabla\Psi = \left((1 + \chi_L)\left(\frac{d^2}{dx^2} + \frac{d^2}{dy^2}\right) + \frac{d^2}{dz^2}\right)\Psi \tag{2.22}$$

inside the ferromagnetic medium and

$$\nabla\Psi = 0 \tag{2.23}$$

outside. The solutions for these two equations strongly depend on the geometry of the ferromagnetic medium. For the case of a thin ferromagnetic film spin waves with their wave vector in the film plane are found. Their frequency depends, beside on their wave vector and the film thickness, overall on the magnetization direction. Therefore three different kinds of modes are found, namely those which were already enlisted above. Thereby the number three [38] arises from now two-dimensional freedom of the wave vector $\mathbf{k}_\parallel$ within the film plane. These are: (i) Spin waves parallel to a ferromagnetic film with normal magnetization (Forward-Volume modes, no frequency dependence on the in-plane wave vector $\mathbf{k}_\parallel$ direction due to the rotational symmetry around the magnetization $\mathbf{M}$ axis), (ii) spin waves with in-plane $\mathbf{k}_\parallel$ perpendicular to the in-plane magnetization (Damon-Eshbach modes) and (iii) spin waves with in-plane $\mathbf{k}_\parallel$ parallel to the in-plane magnetization (Backward-Volume modes).

2.8.1 Modes in In-Plane Magnetized Films (Damon-Eshbach Modes)

The Damon-Eshbach modes [42] have their wave vector $k_\parallel$ in the ferromagnetic film plane perpendicular to the magnetization. When the film is structured to have limited dimensions W in the direction of the wave vector, the Damon-Eshbach modes form standing waves of order n with the wave vector $k_\parallel = n\pi/W$. These can be excited by electromagnetic radiation. For this previously Brillouin scattering with visible or infrared light [37,38] was used.

The Damon-Eshbach mode frequency depends, beside on the in-plane wave vector $k_\parallel$, on the the thickness d of the ferromagnetic film [37,38]:

$$\omega_{DE} = \gamma\sqrt{H(H+M_0) + (M_0/2)^2 \cdot (1 - e^{-2k_\parallel d})} \tag{2.24}$$

Comparing this to the FMR frequency (Kittel equation for a plane 2.9) ($\omega = \gamma\sqrt{H(H+M_0)}$) it is visible that when $k_\parallel$ is reduced (e.g. by increasing W) ω_{DE} approaches the FMR frequency ω. The Damon-Eshbach modes are usually considered surface modes because their electromagnetic magnetic field distribution concentrates at the surface of the ferromagnetic medium whereby the field decays exponentially within the medium with an approximate decay length of $2\pi/k_\parallel$. This is, however, for our conditions in the μm range and thus much larger than our typical film thickness of about 100 nm [38].

When going away from the perpendicular case by reducing the initially right angle Θ between the magnetization and the Damon-Eshbach mode wave vector, ω_{DE} changes and the mode finally disappears at the angle [42]:

$$\Theta_{DE} = \arctan\sqrt{H/M_0} \tag{2.25}$$

In this regime instead of Damon-Eshbach modes Backward volume modes are observed which have a negative dispersion and thus a smaller frequency than the FMR.

2.8.2 Modes in Normally Magnetized Films (Forward-Volume Modes)

When the magnetization lies perpendicular to the ferromagnetic film instead of Damon-Eshbach modes, Forward-Volume modes appear [43]. As already implied by their name they are considered volume modes meaning that their electromagnetic field - in contrast to that of the Damon-Eshbach modes -

increases towards the center of the ferromagnetic film. Their frequency is again determined by their in-plane wave vector $k_\parallel$ and the thickness d of the ferromagnetic film [44]:

$$\tan\alpha|\frac{k_\parallel}{2}|d = \frac{1}{\alpha} \tag{2.26}$$

with

$$\alpha = \sqrt{\frac{M_0(H-M_0)}{(\omega/\gamma)^2-(H-M_0)^2}} \tag{2.27}$$

For long wavelength $\lambda = 2\pi/k_\parallel \gg d$ we can approximate equation (2.26) by

$$\frac{1}{\alpha^2} \approx \frac{k_\parallel d}{2} \tag{2.28}$$

and hence the resonance condition for the Forward-Volume modes is:

$$\omega = \gamma\sqrt{(H-M_0)^2 + \frac{M_0(H-M_0)}{1+2/k_\parallel d}} \tag{2.29}$$

It is obvious that for $k_\parallel \to 0$ the resonance condition becomes that of the FMR. If the Forward-Volume modes are again confined to a width wW, $k_\parallel$ becomes $k_\parallel = n\pi/wW$ like for the case of the Damon-Eshbach modes, where n is again the order of the confined mode.

A more detailed discussion of spin waves of arbitrary orientation of the magnetization and wave vector was exercised by Kalinikos and Slavin [41] who also integrate the possibility of the combination of the Forward-Volume mode with a higher order standing spin wave perpendicular to the ferromagnetic film. A comparison of their theoretical results with our experimental ones can be found in publication P3 which is presented in section 6.2.1.

2.9 Damping

The discussion of the FMR and the spin waves is still not complete up to this point because at the exact resonance magnetic fields H_0 and $H_{0,PSSW}$ (see section 2.5 and 2.7) the Polder tensor $\hat{\chi}$ diverges (see equation 2.8)). The reason is that in the Landau-Liftshitz equation (2.5) there is no term corresponding to energy dissipation meaning that without external energy input

(via h) the magnetization continues to precess with the resonance frequency at constant amplitude. However if there is energy input from the rf magnetic field h at the resonance frequency the precession builds up unlimitedly (however when going beyond the first order approximation of equation (2.6) a change in resonance frequency is found at high precession amplitudes [46]). Conclusively like for stored oscillation energy in general, there are also in this case damping mechanisms which tend to diminish the precession amplitude.

There are different ways to integrate these into the Landau-Liftshitz equation, e.g. Bloch and Gilbert damping. As an example we want to discuss Gilbert damping [47] here because we refer to it in publication P1,P2 and P3. To integrate Gilbert damping into the Landau-Liftshitz equation (2.5) an additional term is needed it:

$$\frac{d}{dt}\mathbf{M} = \gamma\mathbf{H} \times \mathbf{M} + \frac{\alpha_G}{M_0}\mathbf{M} \times \frac{d}{dt}\mathbf{M} \tag{2.30}$$

α_G is a phenomenological constant. Using again the first order approximation of equation (2.6), equation (2.30) becomes:

$$\frac{d}{dt}\mathbf{m} = \gamma\mathbf{z} \times (H\mathbf{m} - M_0\mathbf{h}^{in}) + \frac{\alpha_G}{M_0}\mathbf{M} \times \frac{d\mathbf{m}}{dt} \tag{2.31}$$

Hence equation (2.7) becomes:

$$\begin{aligned} -i\omega m_x + \gamma H m_y &= \gamma M_0 h_y^{in} + i\omega(\alpha_G/M_0)m_y \\ -i\omega m_y - \gamma H m_x &= -\gamma M_0 h_x^{in} - i\omega(\alpha_G/M_0)m_x \end{aligned} \tag{2.32}$$

Thus the impact from the additional damping term on the emerging calculations can be simply introduced by only replacing γH with $\gamma H - i\alpha_G\omega$. This avoids the divergence of the susceptibility tensor $\hat{\chi}$ at the exact resonance position and therefore enables us to e.g. calculate the line shape of the FMR and other ferromagnetic resonances. This is described in publication P1. The impact of the damping on the susceptibility is visualized in figure 2.5.

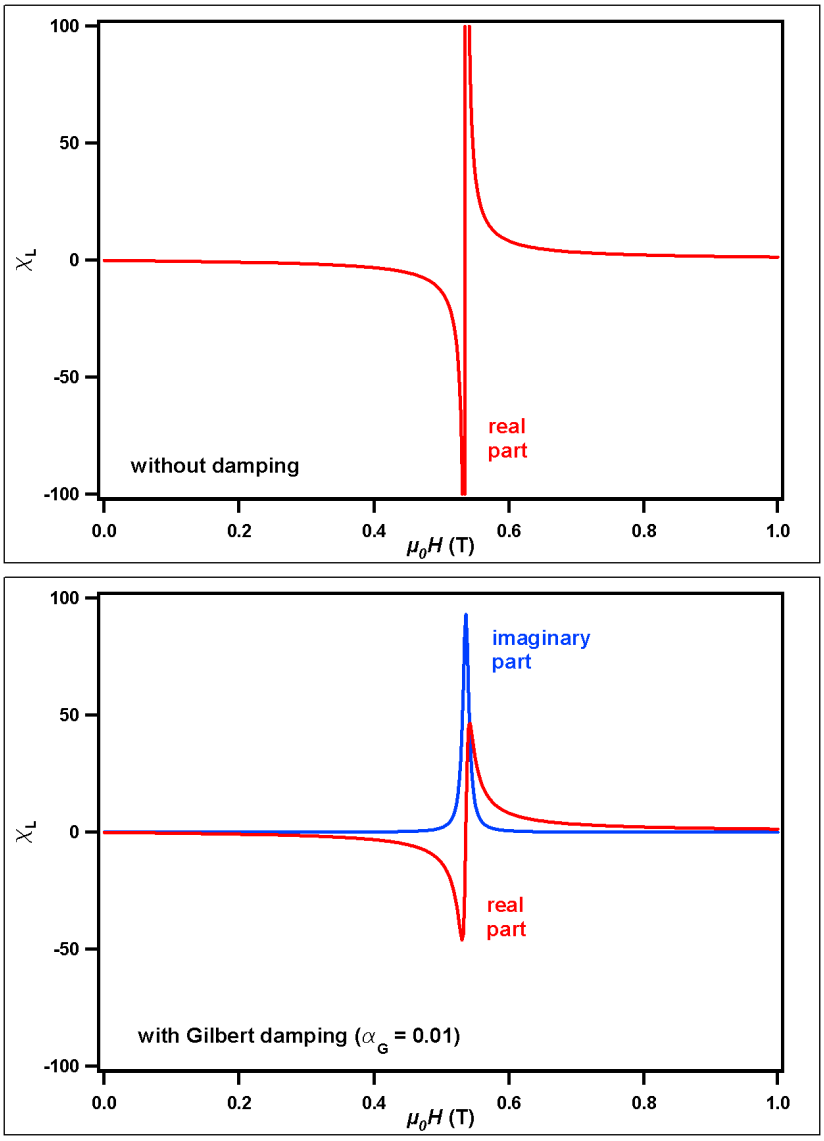

Figure 2.5: Impact of the damping on the susceptibility: The longitudinal component χ_L of the Polder tensor $\hat{\chi}$ (see equation (2.8)) is displayed without damping as well as with Gilbert damping ($\alpha_G = 0.01$). The following parameters are used: The saturation magnetization $\mu_0 M_0 = 1$ T, the gyromagnetic ratio $\gamma/\mu_0 = 2\pi \cdot 28$ GHz/T and the microwave frequency $\omega/2\pi = 15$ GHz. Due to the damping (see equation (2.32)) the previously diverging real part of the susceptibility becomes finite and additionally an imaginary part with Lorentz line shape emerges.

Chapter 3

Preparation of Permalloy Film Stripes

The structures we have prepared in view of the detection of the photovoltage and photoresistance are thin Permalloy ($Ni_{80}Fe_{20}$) films which are structured to stripe shape by photolithography. There are two different preparation techniques we use:

1. LIFT-OFF: An about 5×6 mm^2 Gallium arsenide (GaAs) single crystal substrate is covered with Shipley S1813 positive photoresist. Afterwards a negative image mask of the intended stripe structure is used to expose the photoresist. This is developed afterwards, so that the intended stripe structure is uncovered from photoresist. In the following the substrate is mounted in a high vacuum ($\approx 10^{-7}$ mbar) deposition chamber in which Permalloy is molten to generate a ballistic flux of Nickel-Iron clusters that slowly covers the sample with a typically 50 to 150 nm thick Permalloy layer. Afterwards the lift-off is processed, meaning that acetone is used to remove the still present photoresist below the Permalloy in the substrate regions which are not intended to be covered. During this process the Permalloy film is subject to ultrasonic and heating so that it breaks off above the photoresist and is dislodged. The remaining structure is a Permalloy stripe with Permalloy leads and contacts, a mask image of which can be seen in figure 3.1. The disadvantage of this method is that the lift-off process becomes rather challenging for thick ($d > 100$ nm) Permalloy layers, because the Permalloy layer becomes almost impossible to remove.

2. WET ETCHING: Again an about 5×6 mm^2 GaAs-single crystal substrate is used but now it is directly covered with Permalloy, again in

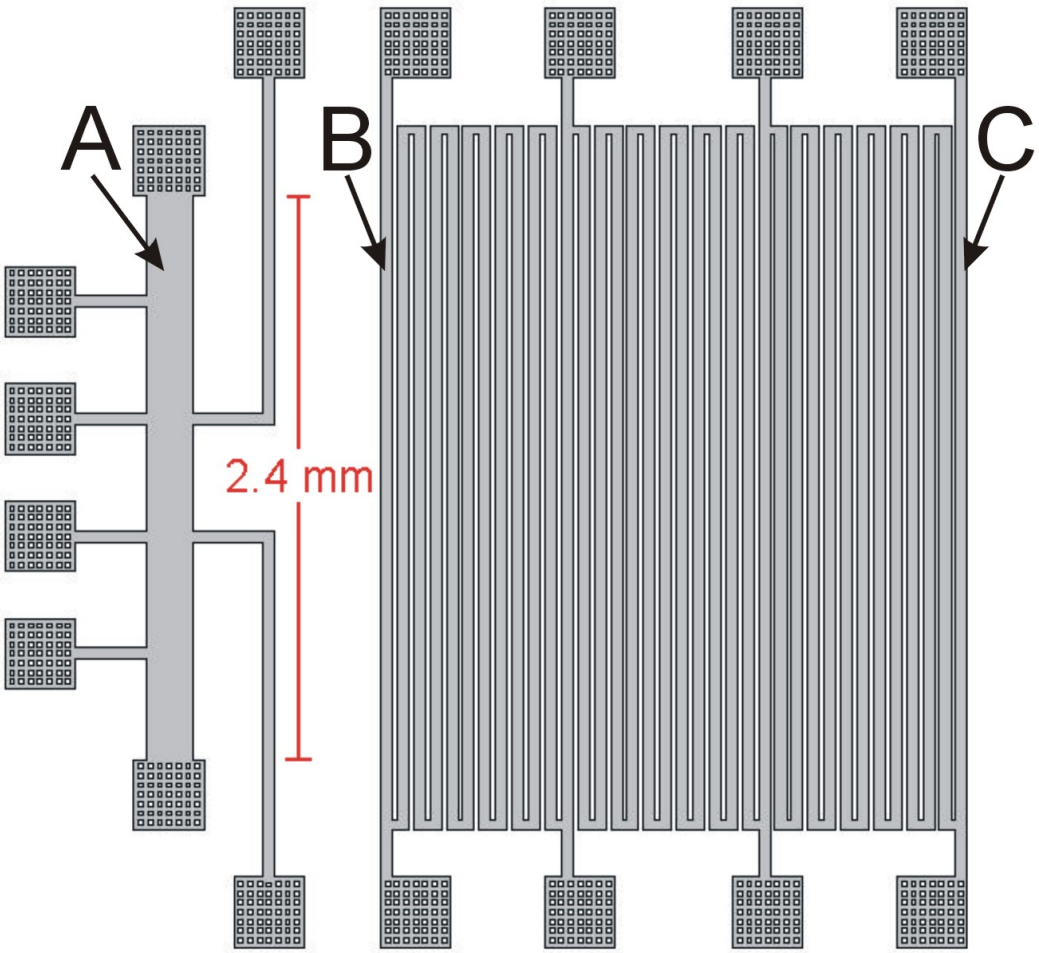

Figure 3.1: Image of the Permalloy stripe mask which was used for the photovoltage measurements in publication P1. The grey area is to be covered with Permalloy. There are two structures visible: The 200 μm wide single stripe (A) on the left side and an array of 50 μm wide stripes on the right side. The stripes are connected at alternating ends to form one long meandering stripe. In the measurements only the single stripe (A), the outer left (B) and the outer right stripe (C) were used. The contact pads are covered with matrices of quadratic holes which were added because the mask was also used for the preparation of two-dimensional electron gas stripes etched into GaAs heterostructures. In that case the holes can help improving the contact to metallic contact layers on top of the heterostructure. Thereby the Schottky barrier is to be overcome by annealing.

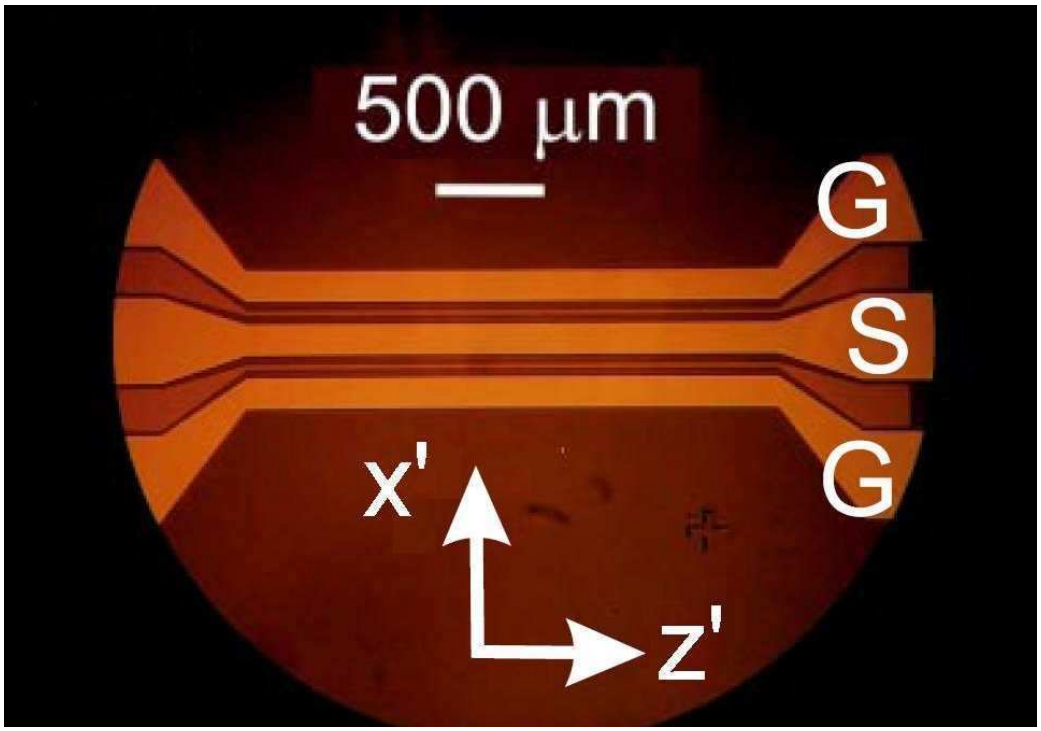

Figure 3.2: Microscope image of one of our coplanar waveguide (CPW) samples: The two Permalloy stripes (dark, thin) by means of which the microwave photovoltage and photoresistance are detected are deposited into the two slots of a Ground(G)-Signal(S)-Ground(G) Silver CPW (light, broad).

the deposition chamber as described above. Then the sample is subsequently covered with photoresist using now a positive mask of the intended stripe structure for the following exposure. After the following development only the stripe structure which is intended to last is covered with photoresist and the remaining Permalloy is uncovered and afterwards removed by a hydrochloric acid solution to which the whole sample is exposed. This process is applicable to Permalloy films of arbitrary thickness and therefore favorable for thick films.

Concerning the Permalloy stripes described in the experimental section of this work usually the LIFT-OFF technique was used. However experiments to also use the wet etching technique for very thick samples ($d > 100$ nm) were also performed. Further in some cases before preparing the Permalloy stripes as an additional preparation step a Gold/Silver/Chrom (5/550/5 nm) multi-layer forming a ground/signal/ground coplanar waveguide (CPW) [45] was prepared. The dimensions of the CPW were chosen to match its

impedance as good as possible to 50 Ω. In this context its ground and signal stripes have a width of 150 μm and the slots between them are 100 μm wide. Afterwards the Permalloy stripes were deposited into the CPW slots. As there are two slots, two identical Permalloy stripes were deposited into the two slots in order to maintain the symmetry of the structure. A microscope picture of the whole structure can be seen in figure 3.2. The CPWs are used to transmit the microwaves as close as possible to the Permalloy stripes.

All the preparation steps described above were performed under the supervision of Dr. Yongsheng Gui in the clean room of the Institut für Angewandte Physik of the University of Hamburg. Finally the structures were glued to typically 8-contact chip carriers and connected to the contacts by means of gold bonding wires.

Chapter 4

Measurement Setup

The measurements presented in this work were performed in the research group of Prof. Dr. Can-Ming Hu at the University of Manitoba, Canada. The setup consists primarily of an microwave generator for radio-frequency fields, an electromagnet for static magnetic fields and lock-in amplifiers for the measurement signal detection. A photo of the setup for microwave photovoltage and photoresistance measurements can be seen in figure 4.1: The sample that was prepared as described above in section 3 is mounted in between the two 10 cm diameter pole caps of an electromagnet that generates the static magnetic field H. Due to the necessary strong currents of up to 70 A the magnet has to be water cooled. The maximal static magnetic field H depends on the air gap between the two pole caps. The air gap can be adjusted continuously. If it is reduced to only about 1 cm fields as high as $\mu_0 H = 2$ T can be reached, whereas if it is increased to 10 cm only about $\mu_0 H = 0.5$ T can be reached.

A sketch of the mountings on the sample holder can be seen in figure 4.2. There are two possibilities of mounting the Permalloy film stripe: Parallel or perpendicular to the magnetic field.

1. In the parallel case the magnetic field lies in the Permalloy film plane and therefore in the sample holder plane (see figure 4.2). That is why in this direction a large air gap is needed ($\gg 2$ cm). Considering the resonance magnetic field H_0 (see equation (2.10)) it is obvious that this is not a severe problem because in this case already moderate magnetic fields ($\mu_0 H < 0.4$ T for $\omega/2\pi < 20$ GHz) are sufficient.

2. In the perpendicular case the magnetic field lies perpendicular to the sample holder and therefore only needs a small air gap (≈ 2 cm). Consequently higher magnetic fields can be achieved. These are indeed necessary in this case because $H > M_0 \approx 1$ T is already only needed

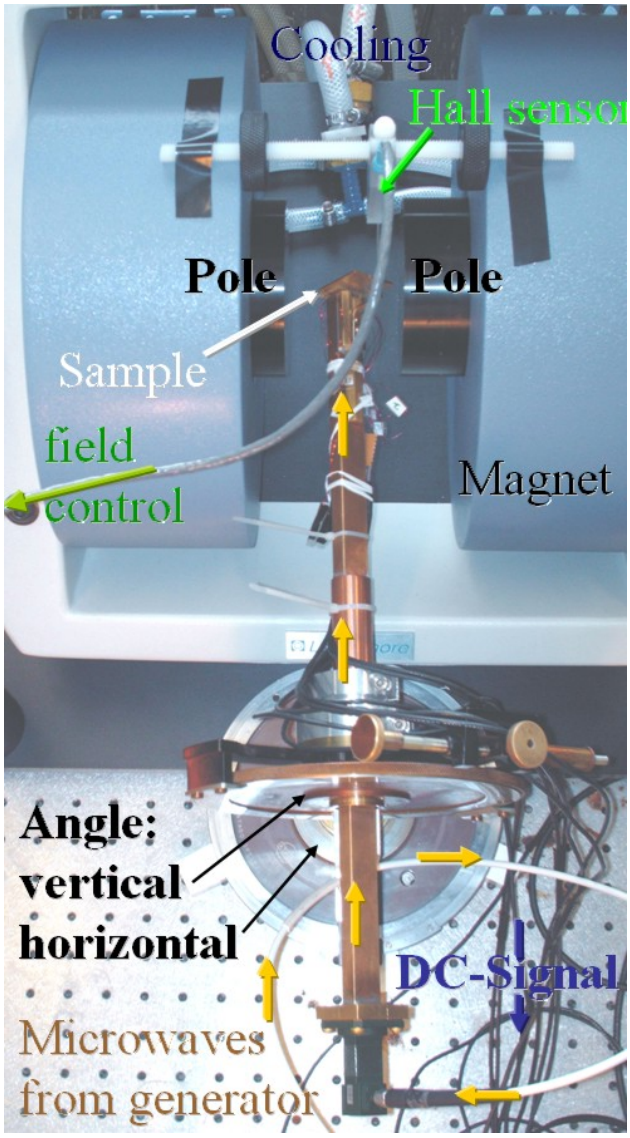

Figure 4.1: Measurement setup: The microwaves arrive through the white coaxial cable which is connected to the microwave generator as marked by arrows on the bottom of the photo. They are transferred onto a rectangular hollow waveguide which transmits them into the core of an electromagnet at the top of the photo. The hollow waveguide passes through a high precision angle readout that allows adjusting its angle and therefore that of the sample in two dimensions. Next to the sample a Hall sensor is mounted that allows magnetic field control via a feedback loop. The black cables connect the sample (film stripe) to the lock-in amplifiers which measure the photovoltage and photoresistance.

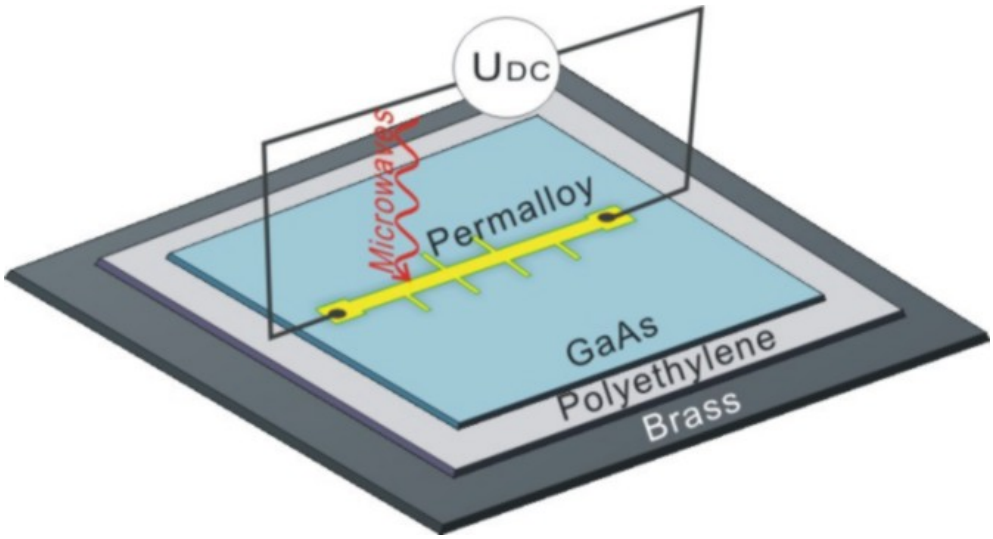

Figure 4.2: Sketch of our brass sample holder. The wiring of the Permalloy stripe (on top of the GaAs substrate) connects it to the lock-in amplifier which measures the photovoltage U_{DC} or alternatively - if a current I from a battery is injected in parallel - the photoresistance U_{DC}/I

to align the magnetization with the magnetic field and thus to enter the regime where equation (2.12) applies. This configuration has however the disadvantage that no microwave irradiation normal to the Permalloy film can be received because the pole caps are in the way. Consequently only irradiation by means of a CPW (on chip) is possible in this case.

As mentioned above a photo of the setup with the sample mounted with the magnetic field in the film and sample holder plane is displayed in figure 4.1. A rectangular hollow K_U-band (12 - 18 GHz) waveguide which is connected to a Hewlett Packard HP83624B microwave generator by means of a coaxial cable and SMA-connectors is used to expose the film stripe. This way the frequency range from 12 GHz to 20 GHz (generator maximum) can be covered. However alternatively also a CPW like that whose preparation is described in section 3 can be connected to the SMA connector to irradiate the sample. This covers the frequency range from 2 GHz (generator minimum) to about 14 GHz. Next to the sample a Hall sensor is mounted which controls the static magnetic field strength via a feedback loop using a digital Gauss meter.

For the microwave photovoltage measurements the contacts of our film stripe are connected to a lock-in amplifier via coaxial cables. If desired also

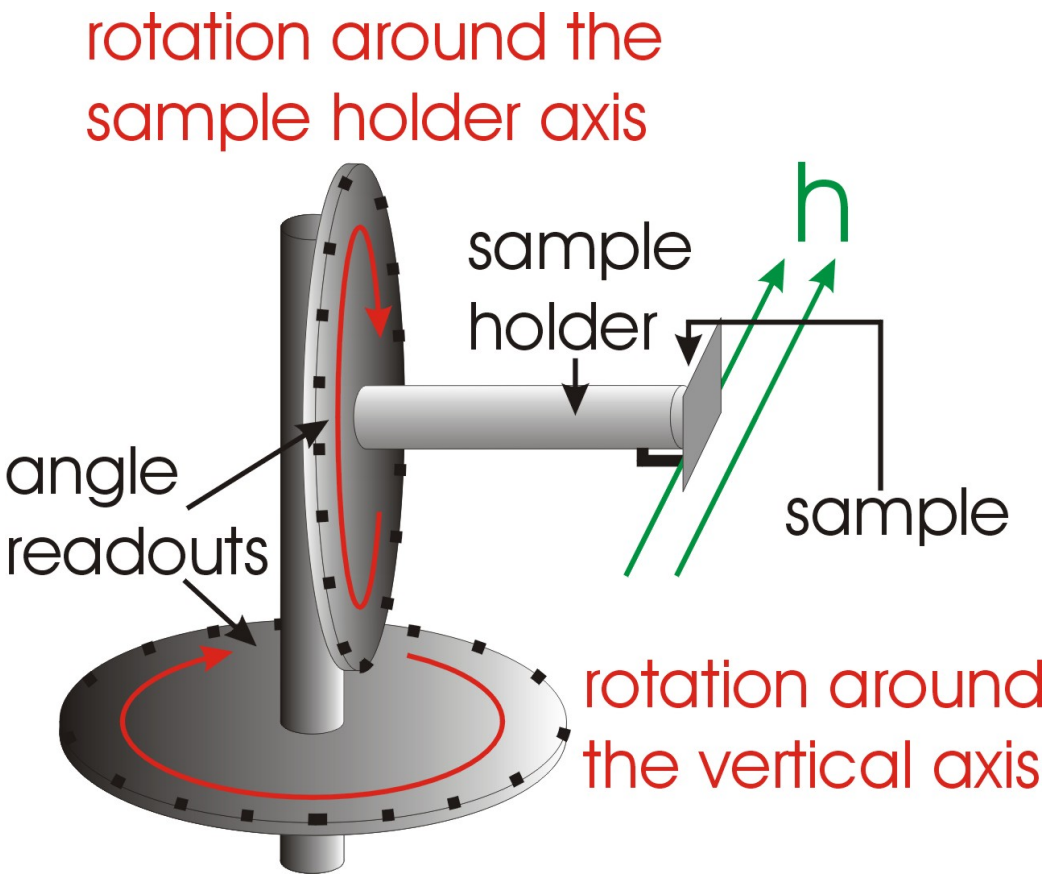

Figure 4.3: Sketch of the sample holder with the two angle readouts. This is on display for the case that the static magnetic field **H** lies in the Permalloy film stripe plane. This is mounted at the end of the sample holder on a plate that faces the sample holder. Therefore the film stripe sample is invisible from this point of view. The sample holder encloses a rectangular hollow waveguide which aims at the film stripe and is used to irradiate it normally. Using the two angle readouts there are two possibilities of rotating the sample: Around the waveguide axis and around the vertical axis. The rotation around the vertical axis is in principle only used to align the sample while the rotation around the waveguide axis is used to alter the angle between the Permalloy film stripe axis and the magnetic field as for example done in publication P1.

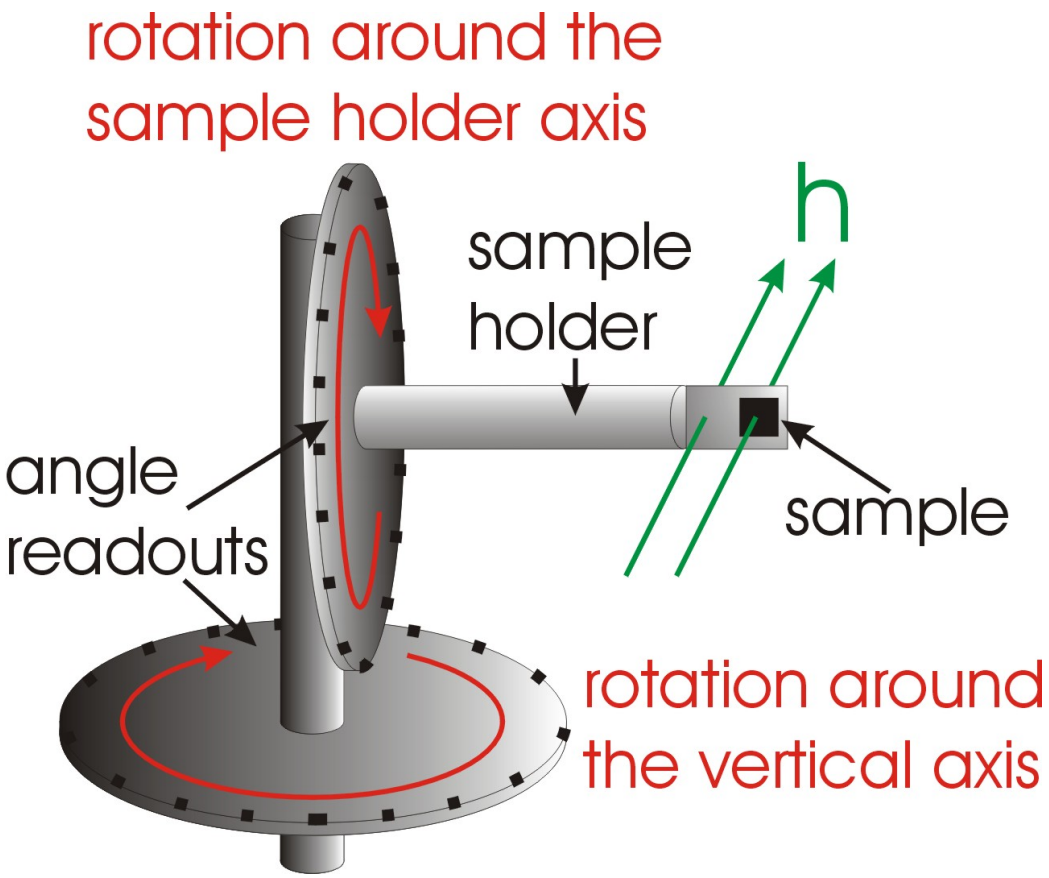

Figure 4.4: Sketch of the sample holder with the two angle readouts. This is on display for the case that the static magnetic field **H** lies normal to the Permalloy film stripe which is mounted at the end of the sample holder on a plate normal to the magnetic field. The sample holder is solid and the film stripe sample has to be irradiated by means of a CPW. Using the two angle readouts there are two possibilities of rotating the sample: Around the waveguide axis and around the vertical axis.

an $U = 9$ V battery with a series resistor can be connected parallel to the amplifier to measure photoresistance instead of photovoltage. In both cases a function generator is used to modulate a square wave signal onto the microwaves and the lock-in amplifier is coupled to the corresponding frequency. Consequently the microwave photovoltage and photoresistance get a square wave modulation, too, and the lock-in amplifier measures the associated sinusoidal fraction. The advantage the advantage of the lock-in technique is, that an excellent sensitivity (≈ 5 nV noise) can be reached. In contrast to this in measurements with dc amplification only a noise level of about 500 nV can be achieved because of for example the electromagnetic noise which also possibly generates a microwave photovoltage across our stripe. This is, however, in general not modulated at the lock-in frequency. Alternatively to photovoltage and photoresistance also photocurrent can be measured using a current instead of voltage amplifier (see publication P2).

In figure 4.1 two angle readouts are visible, one to rotate the sample around the vertical and one to rotate it around the horizontal (waveguide) axis. With these the sample alignment can be controlled in two dimensions. In the displayed case the horizontal readout is used to control the angle between the stripe axis (and therefore the current $\mathbf{I}$ direction) and the static magnetic field $\mathbf{H}$ (and therefore the magnetization $\mathbf{M}_0$) which is rotated in the Permalloy film plane of the sample (a schematic picture can be seen in figure 4.3).

In contrast to the horizontal angle readout which can be used to rotate the sample by 360° the vertical angle readout is only variable by a few degrees because the sample is rotated towards the pole caps in this case. The primary use of this rotation is therefore only to align the magnetization correctly during the preparations for the measurements. In contrast to this the horizontal rotation is usually used for the data collection.

After wiring our Permalloy film stripe the AMR can be used to align it to the magnetic field $\mathbf{H}$ with more precision. The reason is that even if the magnetic field $\mathbf{H}$ is only slightly misaligned with respect to the stripe, sweeping $\mathbf{H}$ up bends the magnetization away from the stripe's easy axis which is in our case aligned to the stripe due to shape anisotropy [29]. Thus the longitudinal resistance changes measurably. The exact alignment of the stripe with the magnetic field is found by determining the position where no impact on the AMR can be detected anymore when sweeping $\mathbf{H}$. For this also a coarse angle adjustment in the lasting third spatial direction (rotation around the magnetic field $\mathbf{H}$) is possible when bending the socket under the waveguide holder.

The same adjustment method also applies in the case that our ferromagnetic film stripe is mounted normal to $\mathbf{H}$ (see figure 4.4). In this case,

however, the maximal deflection in every direction is limited to a few degrees because of the short air gap.

Finally it has to be stated that also the microwave photovoltage which is investigated in this work and described in detail in publication P1 in section 5.1 can be used for the angle adjustment. Thereby the crucial point is that it vanishes if the current - which runs along our film stripe - lies parallel or perpendicular to the external magnetic field **H** (compare equation (21) in publication P1). As far as we could find this allows a much more precise alignment than the direct usage of the AMR.

Chapter 5

In-Plane Magnetized Ferromagnetic Films

In this section we will present our experimental results concerning the microwave photovoltage in in-plane magnetized ferromagnetic films. The magnetic field dependence of the FMR for this case can be seen in figure 2.4. It becomes visible that compared to the normal magnetization case only a relatively low H is needed to excite the FMR and it can be seen that for $|H| < H_0$ also the exchange dominated spin wave resonances and Damon-Eshbach modes can be excited which have been described in section 2.7.1 and 2.8.1 respectively. To give an impression of the microwave spectrum in this case, the microwave photovoltage of a $W = 200$ μm wide and $d = 49$ nm thick Permalloy film stripe is presented in figure 5.1. It is the same stripe whose photovoltage is also investigated in publication P1 (see section 5.1). Beside the FMR which appears at $H = \pm 220$ mT ($\omega/2\pi = 15$ GHz), one standing spin wave mode is observed at $H = \pm 100$ mT for both positive and negative magnetic fields.

A detailed discussion of the experimental results concerning perpendicular standing spin waves in in-plane magnetized Permalloy films will be presented in section 5.3 where a specially thick ($d = 108$ nm) Permalloy film stripe is used. This has the advantage that the resonance magnetic field $H_{0,PSSW}$ of the perpendicular standing spin wave modes is closer to that of the FMR than for the case of figure 5.1 (see equation (2.18)) and thus multiple modes can be visualized. Further in that case on the same substrate also a CPW was prepared so that a much stronger microwave intensity could be achieved at the film stripes location and therefore also a stronger photovoltage and better sensitivity. This enables the observation of also the weak Damon-Eshbach modes which will be described in section 5.4.

However, first we will concentrate on the FMR-induced microwave photo-

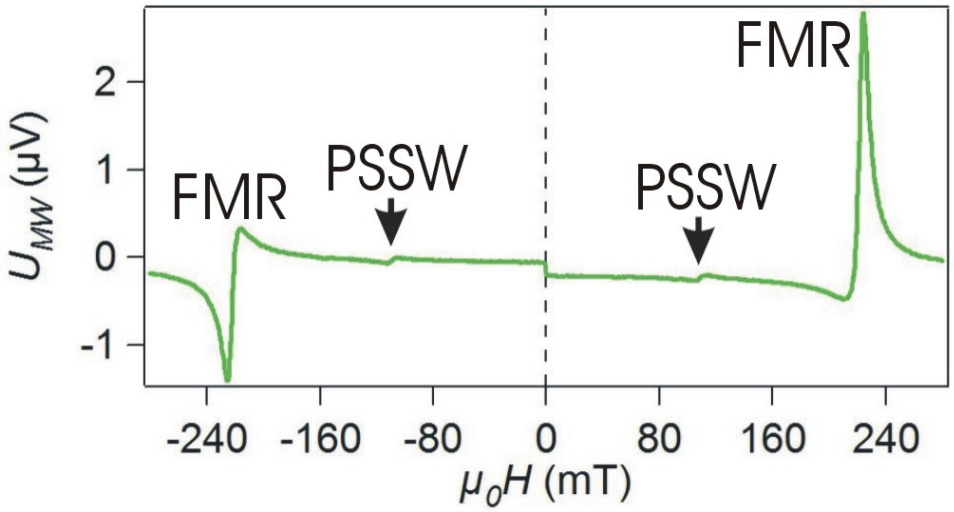

Figure 5.1: Magnetic field H dependence of the microwave photovoltage U_{MW} of the 200 μm wide stripe (A) from the sample of publication P1 (see figure 3.1) at $f = 15$ GHz and with the angle $\alpha_0 = 47°$ between the magnetic field and stripe axis. The FMR appears as a large asymmetric dip and peak at $\mu_0 H = -220$ mT and $\mu_0 H = +220$ mT respectively. Additionally two small steps are visible at $\mu_0 H = \pm 100$ mT (marked by black arrows). These belong to standing spin wave resonances perpendicular to the film (PSSW). The step at $\mu_0 H = 0$ arises from a small non-resonant photovoltage signal which appears in almost all of our measurements and only depends on the magnetic field direction but not on its strength. It arises from the non-resonant photovoltage background discussed in section III C in publication P1.

voltage. As it arises from the AMR-induced spin rectification its theoretical value is derived based on the AMR and the ferromagnetic rf susceptibility $\hat{\chi}$ which were both presented in section 2. The microwave photovoltage mechanism is thereby that the microwaves excite the magnetization to precess so that the AMR is periodically alternated. At the same time the microwaves induce an rf current along our ferromagnetic stripe whose corresponding rf voltage is thus rendered asymmetric with a non-zero time-average by the oscillating AMR (rectification).

The special importance of this section is that the theoretical result in publication P1 can be considered exemplary for the microwave photovoltage and photoresistance in normally magnetized films and spin wave resonances, too. The calculated microwave photovoltage is compared to experimental results of the FMR (compare figure 5.1). Thereby we put an emphasis on the microwave photovoltage's line shape in magnetic field sweeps and on its dependence on the magnetic field direction.

The excellent reproducibility of the measured microwave photovoltage by our theoretical model leads us on the one hand to consider its application in magnetic field sensing what we have described in detail in a separate publication [26] and on the other hand to integrate a consistent description of the AMR-induced microwave photoresistance into our model, too.

Section 5 is organized as follows: In subsection 5.1 publication P1 is presented where the focus is on the investigation of the microwave photovoltage and photoresistance induced by the FMR. Thereby an important result is that the microwave photoresistance is also bipolar like the microwave photovoltage. It has to be noted that a bolometric microwave photoresistance [15] is also found. Its interplay with the AMR-based photoresistance is discussed in publication P4.

Following publication P1 in subsection 5.2 further theoretical and experimental details are presented which were omitted in P1 to limit its length. This is then followed by the experimental results concerning the microwave photovoltage from perpendicular standing spin waves and Damon-Eshbach modes in subsection 5.3 and 5.4, respectively.

5.1 P1: Microwave Photovoltage and Photoresistance Effects in Ferromagnetic Microstrips

N. Mecking, Y. S. Gui, and C.-M. Hu

Phys. Rev. B **76**, 224430 (2007)

PHYSICAL REVIEW B **76**, 224430 (2007)

Microwave photovoltage and photoresistance effects in ferromagnetic microstrips

N. Mecking,[1,2,*] Y. S. Gui,[1] and C.-M. Hu[†]
[1]*Department of Physics and Astronomy, University of Manitoba, Winnipeg, Canada R3T 2N2*
[2]*Institut für angewandte Physik und Zentrum für Mikrostrukturforschung, Universität Hamburg, Jungiusstraße 11, 20355 Hamburg, Germany*

(Received 23 August 2007; revised manuscript received 4 November 2007; published 27 December 2007)

We investigate the dc electric response induced by ferromagnetic resonance in ferromagnetic Permalloy ($Ni_{80}Fe_{20}$) microstrips. The resulting magnetization precession alters the angle of the magnetization with respect to both dc and rf current. Consequently the time averaged anisotropic magnetoresistance (AMR) changes (photoresistance). At the same time the time-dependent AMR oscillation rectifies a part of the rf current and induces a dc voltage (photovoltage). A phenomenological approach to magnetoresistance is used to describe the distinct characteristics of the photoresistance and photovoltage with a consistent formalism, which is found in excellent agreement with experiments performed on in-plane magnetized ferromagnetic microstrips. Application of the microwave photovoltage effect for rf magnetic field sensing is discussed.

DOI: 10.1103/PhysRevB.76.224430 PACS number(s): 76.50.+g, 75.30.Gw, 07.57.Kp

I. INTRODUCTION

The fact that macroscopic mutual actions exist between electricity and magnetism has been known for centuries as described in many textbooks of electromagnetism.[1] Now, this subject is transforming onto the microscopic level, as revealed in various spin-charge coupling effects studied in the new discipline of spintronics. Among them, striking phenomena are the dc charge transport effects induced by spin precession in ferromagnetic metals, which feature both academic interest and technical significance.[2,3] Experiments have been performed independently by a number of groups on devices with different configurations.[4–16] Most works were motivated by the study of spin torque,[17,18] which describes the impact of a spin-polarized charge current on the magnetic moment. In this context, Tulapurkar *et al.* made the first spin-torque diode,[4] and Sankey *et al.* detected the spin-torque-driven ferromagnetic resonance (FMR) electrically.[5] Both measured the vertical transport across nanostructured magnetic multilayers. Along a parallel path, a number of works[19–21] have been devoted to study the effect of spin pumping. One of the interesting predictions is that injection of a spin current from a moving magnetization into a normal metal induces a dc voltage across the interface. To detect such a dc effect induced by spin pumping,[20] experiments have been performed by measuring lateral transport in hybrid devices under rf excitation.[6–8]

From a quite different perspective, Gui *et al.* set out to explore the general impacts of the high frequency response on the dc transport in ferromagnetic metals,[9] based on the consideration that similar links in semiconductors have been extensively applied for electrical detection of both spin and charge excitations.[22] Gui *et al.* detected, subsequently, photoresistance induced by bolometric effect,[9] as well as photocurrent,[10] photovoltage,[11] and photoresistance[12] caused by the spin-rectification effect. A spin dynamo[10] was thereby realized for generating dc current via the spin precession, and the device was applied for a comprehensive electrical study of the characteristics of quantized spin excitations in microstructured ferromagnets.[11] The spin-rectification effect was independently investigated by both Costache *et al.*[13] and Yamaguchi *et al.*[14] and seems to be also responsible for the dc effects detected earlier by Oh *et al.*[15] A method for distinguishing the photoresistance induced by either spin precession or bolometric effect was recently established,[12] which is based on the nice work performed by Goennenwein *et al.*,[16] who determined the response time of the bolometric effect in ferromagnetic metals.

While most of these studies, understandably, tend to emphasize the different nature of dc effects investigated in different devices, it is perhaps more intriguing to ask the questions of whether the seemingly diverse but obviously related phenomena could be described by a unified phenomenological formalism and whether they might arise from a similar microscopic origin. From a historical perspective, these two questions reflect exactly the spirit of two classic papers[23,24] published by Juretscheke and Silsbee *et al.*, respectively, which have been often ignored but have shed light on the dc effects of spin dynamics in ferromagnets. In the approach developed by Juretscheke, photovoltage induced by FMR in ferromagnetic films was described based on a phenomenological depiction of magnetoresistive effects.[23] While in the microscopic model developed by Silsbee *et al.* based on the combination of Bloch and diffusion equations, a coherent picture was established for the spin transport across the interface between ferromagnets and normal conductors under rf excitation.[24]

The goal of this paper is to provide a consistent view for describing photocurrent, photovoltage, and photoresistance of ferromagnets based on a phenomenological approach to magnetoresistance. We compare the theoretical results with experiments performed on ferromagnetic microstrips in detail. The paper is organized in the following way: In Sec. II, a theoretical description of the photocurrent, photovoltage, and photoresistance in thin ferromagnetic films under FMR excitation is presented. Sections II A–II D establish the formalism for the microwave photovoltage (PV) and photoresistance (PR) based on the phenomenological approach to magnetoresistance. These arise from the nonlinear coupling of microwave spin excitations (resulting in magnetization **M** precession) with charge currents by means of the anisotropic

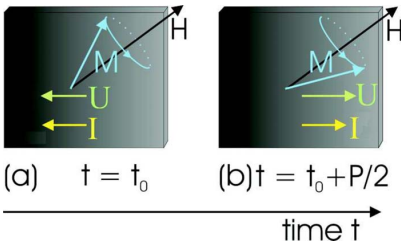

FIG. 1. (Color online) Mechanism of the AMR-induced microwave photovoltage: **M** precesses (period P) in phase with the rf current **I**. (a) **M** lying almost perpendicular to **I** results in low AMR. (b) **M** lying almost parallel to **I** results in high AMR. The time average voltage **U** becomes nonzero.

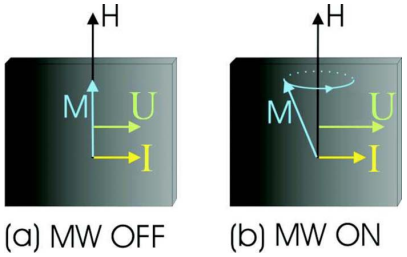

FIG. 2. (Color online) Mechanism of the AMR-induced photoresistance. (a) Without microwaves (MW) **M** lies perpendicular to the dc current **I** and the AMR is minimal (b) With microwaves **M** precesses and is not perpendicular to **I** anymore. Consequently the AMR increases (higher voltage drop **U**).

magnetoresistance (AMR). Section II E compares our model with the phenomenological approach developed by Juretscheke. Section II F provides a discussion concerning the microwave photovoltage and photoresistance based on other magnetoresistance effects [like anomalous Hall effect (AHE), giant magnetoresistance (GMR), and tunneling magnetoresistance (TMR)].

Experimental results on microwave photovoltage and photoresistance measured in ferromagnetic microstrips are presented in Secs. III and IV, respectively. We focus in particular on their characteristic different line shapes, which can be well explained by our model. In Sec. V conclusions and an outlook are given.

II. MICROWAVE PHOTOVOLTAGE AND PHOTORESISTANCE BASED ON PHENOMENOLOGICAL AMR

A. AMR coupling of spin and charge

The AMR coupling of spin and charge in ferromagnetic films results in microwave photovoltage and photoresistance. The photovoltage can be understood regarding Ohms law [current $I(t)$ and voltage $U(t)$]

$$U(t) = R(t) \cdot I(t). \tag{1}$$

We consider a time-dependent resistance $R(t)=R^0+R^1\cos(\omega t-\psi)$ which oscillates at the microwave frequency $\omega=2\pi f$ due to the AMR oscillation arising from magnetization precession. ψ is the oscillations phase shift with respect to the phase of the rf current $I(t)$. For the sake of generality ψ will be kept as a parameter in this work and will be discussed in detail in Sec. III C. $I(t)$ takes the form $I(t)=I_1\cos(\omega t)$ and is induced by the microwaves. It follows that $U(t)$ consists of time-dependent terms with the frequency ω, 2ω and a constant term (time independent) which corresponds to the time average voltage and is equal to the photovoltage: $U_{\mathrm{MW}}=\langle R^1 I_1\cos(\omega t-\psi)\cos(\omega t)\rangle=(R^1 I_1\cos\psi)/2$ ($\langle\ \rangle$ denotes time-averaging). A demonstrative picture of the microwave photovoltage mechanism can be seen in Fig. 1.

The second effect we investigate which is also based on AMR spin-charge coupling is the microwave photoresistance ΔR_{MW}. This has been reported recently[13] with the equilibrium magnetization $\mathbf{M}_0$ of a ferromagnetic stripe aligned to a dc current $\mathbf{I}_0$. Microwave induced precession then misaligns the dynamic magnetization **M** with respect to $\mathbf{I}_0$ and thus makes the AMR drop measurably. In this work, we present results which also show that if $\mathbf{M}_0$ lies perpendicular to $\mathbf{I}_0$ the opposite effect takes place: Microwave induced precession causes **M** to leave its perpendicular position which increases the AMR (see Fig. 2).

After this qualitative introduction we want to go ahead with a quantitative description of the AMR induced microwave photovoltage and photoresistance. Therefore, we define an orthogonal coordinate system (x,y,z) (see Fig. 3). The y axis lies normal to the film plane and the z axis is aligned with the magnetic field **H** and hence with the magnetization **M** which is always aligned with **H** in our measurements because of the sample being always magnetized to saturation.

Geometrically our samples are thin films patterned to stripe shape, so that $d \ll w \ll l$, where d, w, and l are the thickness, width, and length of the sample. We apply **H** always in the ferromagnetic film plane. For calculations based on the stripes geometry the coordinates x' and z' are defined. These lie in the film plane. x' is perpendicular and z' parallel to the stripe. The following coordinate transformation applies: $(x,y,z)=[x'\cos(\alpha_0)-z'\sin(\alpha_0),y,z'\cos(\alpha_0)+x'\sin(\alpha_0)]$ where α_0 is the angle between **H** and the stripe.

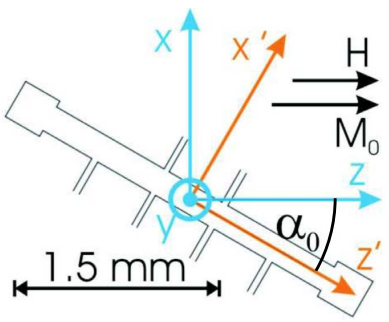

FIG. 3. (Color online) (x,y,z) and (x',y,z') coordinate systems in front of a layout of our Permalloy film stripe ($200\times2400\ \mu\mathrm{m}^2$) with two contacts and six side junctions.

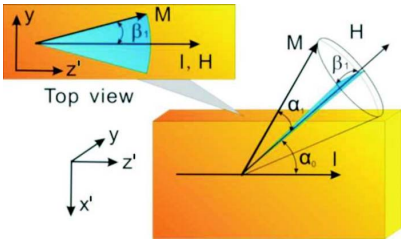

FIG. 4. (Color online) Sketch of the magnetization precession. The magnetic field **H** encloses the angle α_0 with the current **I**. The magnetization oscillation toward **I** has the amplitude α_1 and that perpendicular to **I**: β_1.

For the microwave photovoltage and photoresistance the longitudinal resistance $R(t)=R_0+R_A\cos^2\theta(t)$ of the film stripe matters. It consists of the minimal longitudinal resistance R_0 and the additional resistance $R_A\cos^2\theta(t)$ from AMR. $\theta(t)$ is the angle between the z'-axis (parallel to the stripe) and **M**. **M** moves on a sphere with the radius M_0, which is the saturation magnetization of our sample. $\theta(t)$ can be decomposed into the angle $\alpha(t)$ in the ferromagnetic film plane and the out-of-plane angle $\beta(t)$ (see Fig. 4). Consequently,

$$\cos\theta(t)=\cos\alpha(t)\cos\beta(t). \tag{2}$$

Precession of the magnetization then yields oscillation of $\alpha(t)$, $\beta(t)$, and $\theta(t)$. In our geometry the equilibrium magnetization $\mathbf{M}_0$ encloses the in-plane angle α_0 with the stripe. Hence in time average $\langle\beta(t)\rangle=0$ and $\langle\alpha(t)\rangle=\alpha_0$. In general the magnetization precession is elliptical. Its principle axis lie along the x and y axis and correspond to the amplitudes α_1 and β_1 of the in- and out-of-plane angles α_1^t and β_1^t of the rf magnetization: $\alpha(t)=\alpha_0+\alpha_1^t(t)=\alpha_0+\alpha_1\cos(\omega t-\psi)$ and $\beta(t)=\beta_1^t(t)=-\beta_1\sin(\omega t-\psi)$ [see Fig. 4]. Using Eq. (2) we approximate $\cos^2\theta(t)$ to second order in α_1^t and β_1^t:

$$\cos^2\theta(t)\approx\cos^2\theta|_{\alpha_1^t=\beta_1^t=0}+\alpha_1^t\left.\frac{d\cos^2\theta}{d\alpha_1^t}\right|_{\alpha_1^t=\beta_1^t=0}+0+\frac{\alpha_1^{t2}}{2}\left.\frac{d^2\cos^2\theta}{d\alpha_1^{t2}}\right|_{\alpha_1^t=\beta_1^t=0}+\frac{\beta_1^{t2}}{2}\left.\frac{d^2\cos^2\theta}{d\beta_1^{t2}}\right|_{\alpha_1^t=\beta_1^t=0}. \tag{3}$$

The first order in β_1^t vanishes because it is proportional to $(\sin\beta)|_{\beta_1=0}=0$. It follows that

$$\cos^2\theta(t)\approx\cos^2\alpha_0-\alpha_1\sin 2\alpha_0\cos(\omega t-\psi)-\alpha_1^2\cos 2\alpha_0\cos^2(\omega t-\psi)-\beta_1^2\cos^2\alpha_0\sin^2(\omega t-\psi). \tag{4}$$

This equation is now used to calculate the longitudinal stripe voltage. To consider the general case an externally applied dc current I_0 and a microwave induced rf current I_1 are included in $I(t)=I_0+I_1\cos(\omega t)$. It follows from Eq. (1) that

$$U(t)=[R_0+R_A\cos^2\theta(t)][I_0+I_1\cos(\omega t)]. \tag{5}$$

Consequently $U(t)$ can be written as $U(t)=U_0+U_1\cos(\omega t-\psi_1)+U_2\cos(2\omega t-\psi_2)+U_3\cos(3\omega t-\psi_3)$. For the photovoltage and photoresistance only the constant term U_0, which is equivalent to the time average voltage $\langle U(t)\rangle$, matters. Combining Eqs. (4) and (5), we find

$$U_0=I_0(R_0+R_A\cos^2\alpha_0)-I_1R_A\alpha_1\sin 2\alpha_0\cos(\psi)/2-I_0(\alpha_1^2\cos 2\alpha_0+\beta_1^2\cos^2\alpha_0)R_A/2. \tag{6}$$

Note that $\langle\sin^2(\omega t-\psi)\rangle=\langle\cos^2(\omega t-\psi)\rangle=1/2$ and $\langle\cos\omega t\cos(\omega t-\psi)\rangle=\cos(\psi)/2$. The first term in Eq. (6) is independent of the rf quantities I_1, α_1 and β_1 and represents the static voltage drop of I_0. The second term is the microwave photovoltage U_{MW}. It shows no impact from the dc current I_0. The third term represents the microwave photoresistance ΔR_{MW}. It is proportional to I_0 and depends on the microwave quantities α_1 and β_1. It can be seen now that the rf resistance amplitude R^1 used in the beginning of this paragraph corresponds to $R^1=R_A\alpha_1\sin 2\alpha_0$.

To analyze the magnetization's angle oscillation amplitudes α_1 and β_1 it is necessary to express them by means of the corresponding rf magnetization $\mathrm{Re}(\mathbf{m}e^{-i\omega t})$. **m** is the complex rf magnetization amplitude. Its phase is defined with respect to I_1, so that $\mathrm{Re}(m_xe^{-i\omega t})$ is in phase with $I_1\cos\omega t$ at the FMR. Because $\mathbf{M}=\mathbf{M}_0+\mathbf{m}$, $\mathbf{m}=(m_x,m_y,0)$ can (in first order approximation) only lie perpendicular to $\mathbf{M}_0$ because **M** and $\mathbf{M}_0$ have the same length (M_0). Hence $|m_x|/M_0=\sin\alpha_1\approx\alpha_1$ and $|m_y|/M_0=\sin\beta_1\approx\beta_1$ for $\alpha_1,\beta_1\ll 90°$.

The microwave photovoltage and photoresistance appear whenever magnetization precession is excited. This means if the microwaves are in resonance with the FMR, with standing exchange spin waves perpendicular to the film[10,11,25] or with magnetostatic modes.[11] In this article we will analyze the FMR induced microwave photoresistance and photovoltage.

B. Magnetization dynamics

To understand the impact of the applied rf magnetic field $\mathrm{Re}(\mathbf{h}e^{-i\omega t})$ on the microwave photovoltage and photoresistance the effective susceptibilities χ_{xx}, χ_{xy}, and χ_{yy}, which link $\mathbf{m}e^{-i\omega t}$ inside the sample with the complex external rf magnetic field $\mathbf{h}e^{-i\omega t}=(h_x,h_y,h_z)e^{-i\omega t}$ outside the sample, have to be calculated. Here ψ is encoded in the complex phase of **m**.

The susceptibility inside the sample (magnetic field $\mathbf{h}^{\mathrm{in}}e^{-i\omega t}=(h_x^{\mathrm{in}},h_y^{\mathrm{in}},h_z^{\mathrm{in}})e^{-i\omega t}$) is determined by the Polder tensor[26] $\hat{\chi}$ (received from solving the Landau-Liftshitz-Gilbert equation[28]):

$$\mathbf{m}=\hat{\chi}\mathbf{h}^{\mathrm{in}}=\begin{pmatrix}\chi_L & i\chi_T & 0\\ -i\chi_T & \chi_L & 0\\ 0 & 0 & 0\end{pmatrix}\mathbf{h}^{\mathrm{in}}, \tag{7}$$

with

$$\chi_L = \frac{\omega_M \omega_r}{\omega_r^2 - \omega^2}, \quad \chi_T = \frac{\omega \omega_M}{\omega_r^2 - \omega^2},$$

where $\omega_M = \gamma M_0$ with the gyromagnetic ratio $\gamma \approx \mu_0 \times e/m = 2\pi\mu_0 \times 28$ GHz/T (electron charge e and mass m_e) and $\omega_r = \gamma H$ without damping. Approximation of our sample as a two-dimensional film results in the boundary conditions that h_x and b_y are continuous at the film surface meaning $h_x = h_x^{\text{in}}$ and $b_y = \mu_0 h_y = \mu_0[(1+\chi_L)h_y^{\text{in}} - i\chi_T h_x^{\text{in}}]$. Hence

$$\mathbf{m} = \begin{pmatrix} \chi_{xx} & i\chi_{xy} & 0 \\ -i\chi_{xy} & \chi_{yy} & 0 \\ 0 & 0 & 0 \end{pmatrix} \mathbf{h}, \tag{8}$$

with

$$\chi_{xx} = \frac{\omega_r \omega_M + \omega_M^2}{\omega_r(\omega_r + \omega_M) - \omega^2},$$

$$\chi_{xy} = \frac{\omega \omega_M}{\omega_r(\omega_r + \omega_M) - \omega^2},$$

$$\chi_{yy} = \frac{\omega_r \omega_M}{\omega_r(\omega_r + \omega_M) - \omega^2}.$$

χ_{xx} is identical to the susceptibility describing the propagation of microwaves in an unlimited ferromagnetic medium in Voigt geometry[29] (propagation perpendicular to $\mathbf{M}_0$). χ_{xx}, χ_{xy}, and χ_{yy} have the same denominator, which becomes resonant (maximal) when $\omega = \sqrt{\omega_r^2 + \omega_r \omega_M}$. This is in accordance with the FMR frequency of the Kittel formula for in-plane magnetized infinite ferromagnetic films.[30]

This relatively simple behavior is due to the assumption that $\mathbf{h}^{\text{in}}$ is constant within the film stripe. This assumption is only valid if the skin depth[1] δ of the microwaves in the sample is much larger than the sample thickness. During our measurements we fix the microwave frequency f and sweep the magnetic field H. Consequently we find the FMR magnetic field H_0 with

$$\omega^2 = \gamma^2(H_0^2 + H_0 M_0) \tag{9}$$

and

$$H_0 = \sqrt{M_0^2/4 + \omega^2/\gamma^2} - M_0/2. \tag{10}$$

Now we introduce Gilbert damping[27] α_G by setting $\omega_r := \omega_0 - i\alpha_G\omega$ with now $\omega_0 = \gamma H$ instead of $\omega_r = \gamma H$. We separate the real and imaginary part of χ_{xx}, χ_{xy}, and χ_{yy}:

$$\chi_{xx} = (\omega_r \omega_M + \omega_M^2)F,$$

$$\chi_{xy} = \omega \omega_M F,$$

$$\chi_{yy} = \omega_r \omega_M F, \tag{11}$$

with

$$F = \frac{\omega_0(\omega_0 + \omega_M) - \alpha_G^2\omega^2 - \omega^2 + i\alpha_G\omega(2\omega_0 + \omega_M)}{[\omega_0(\omega_0 + \omega_M) - \alpha_G^2\omega^2 - \omega^2]^2 + \alpha_G^2\omega^2(2\omega_0 + \omega_M)^2}$$

$$\approx \frac{(H + H_0 + M_0)(H - H_0) + i(2H + M_0)\alpha_G\omega/\gamma}{(H + H_0 + M_0)^2(H - H_0)^2 + (2H + M_0)^2\alpha_G^2\omega^2/\gamma^2}.$$

The approximation was done by neglecting the $\alpha_G^2\omega^2$ correction to the resonance frequency $\omega^2 = \omega_0(\omega_0 + \omega_M) - \alpha_G^2\omega^2 \approx \omega_0(\omega_0 + \omega_M)$ which is possible if $\alpha_G \ll 1$. Hence

$$\chi_{xx,xy,yy} \approx A_{xx,xy,yy} \frac{\Delta H(H - H_0) + i\Delta H^2}{(H - H_0)^2 + \Delta H^2}, \tag{12}$$

with $\Delta H = [(2H + M_0)/(H + H_0 + M_0)]\alpha_G\omega/\gamma$. This can be approximated as $\Delta H \approx \alpha_G\omega/\gamma$ if $|H - H_0| \ll H_0$. A_{xx}, A_{xy}, and A_{yy} determine the scalar amplitude of χ_{xx}, χ_{xy}, and χ_{yy}.

To analyze the FMR line shape in the following, we will call the Lorentz line shape which is proportional to $\Delta H/[(H - H_0)^2 - \Delta H^2]$ symmetric Lorentz line shape and the line shape proportional to $(H - H_0)/[(H - H_0)^2 - \Delta H^2]$ antisymmetric Lorentz line shape. A linear combination of both will be called asymmetric Lorentz line shape. $|H - H_0| \ll H_0$ allows us to approximate

$$A_{xx} \approx \frac{\gamma(H_0 M_0 + M_0^2)}{\alpha_G\omega(2H_0 + M_0)},$$

$$A_{xy} \approx \frac{M_0}{\alpha_G(2H_0 + M_0)},$$

$$A_{yy} \approx \frac{\gamma H_0 M_0}{\alpha_G\omega(2H_0 + M_0)}. \tag{13}$$

These are scalars which are independent of the dc magnetic field H and hence characteristic for the sample at fixed frequency. Indeed the assumption of Gilbert damping is not essential for the derivation of Eq. (13). In the event of a different kind of damping, ΔH can also be directly input into Eq. (13) replacing $\alpha_G\omega$. However, because of the commonness of Gilbert damping, its usage here can provide a better feeling for the usual frequency dependence of $A_{xx,xy,yy}$. Going ahead, Eq. (8) becomes

$$\mathbf{m} \approx \frac{\Delta H(H - H_0) + i\Delta H^2}{(H - H_0)^2 + \Delta H^2} \begin{pmatrix} A_{xx} & iA_{xy} & 0 \\ -iA_{xy} & A_{yy} & 0 \\ 0 & 0 & 0 \end{pmatrix} \mathbf{h}. \tag{14}$$

The H-field dependencies has Lorentz line shape with antisymmetric (dispersive) real and symmetric (absorptive) imaginary part, the amplitudes A_{xx}, $\pm iA_{xy}$, and A_{yy}, respectively, and the width ΔH. Note that $A_{xx}A_{yy} \approx A_{xy}^2$ for $|H - H_0| \ll H_0$. Consequently, the susceptibility amplitude tensor can be simplified to

$$\begin{pmatrix} A_{xx} & iA_{xy} & 0 \\ -iA_{xy} & A_{yy} & 0 \\ 0 & 0 & 0 \end{pmatrix} \mathbf{h} \approx \begin{pmatrix} \sqrt{A_{xx}} \\ -i\sqrt{A_{yy}} \\ 0 \end{pmatrix} \left[\begin{pmatrix} \sqrt{A_{xx}} \\ i\sqrt{A_{yy}} \\ 0 \end{pmatrix} \mathbf{h} \right]$$

and Eq. (14) becomes

$$\mathbf{m} = \frac{\gamma M_0}{\alpha_G \omega (2H_0 + M_0)} \frac{\Delta H (H - H_0) + i \Delta H^2}{(H - H_0)^2 + \Delta H^2} \begin{pmatrix} \sqrt{1 + M_0/H_0} \\ -i \\ 0 \end{pmatrix} \times \left[\begin{pmatrix} \sqrt{1 + M_0/H_0} \\ i \\ 0 \end{pmatrix} \mathbf{h} \right]. \quad (15)$$

It is visible that the ellipticity of **m** is independent of the exciting magnetic field **h**. Only the amplitude and phase of **m** are defined by **h**. The reason is the weak Gilbert damping α_G for which much energy needs to be stored in the magnetization precession to have a compensating dissipation. Hence little energy input and impact from **h** appears.

From Eq. (15) follows that m_x and m_y have cardinally the ratio

$$m_x/m_y = i\sqrt{1 + M_0/H_0}. \quad (16)$$

Therefore, m_y vanishes for $\omega \to 0$ and $m_x = i m_y$ for $\omega \to \infty$. This means that the precession of **M** is elliptical and becoming more circular for high frequencies and more linear (along the x axis) for low frequencies. This description applies for the case of an in-plane magnetized ferromagnetic film. However, in the case that the sample has circular symmetry with respect to the magnetization direction (e.g., in a perpendicular magnetized disk or infinite film[10,11]): $\alpha_1 = \beta_1$. This is the same as in the case that $\omega \to \infty$. Only in these cases the magnetization precession can be described in terms of one precession cone angle.[13] Otherwise, distinct attention has to be paid to α_1 and β_1 (see III B). Additionally, it can be seen in Eq. (15) that m_y/m_x is also the ratio of the coupling strength of **m** to h_y and h_x, respectively.

C. Microwave photoresistance

The microwave photoresistance ΔR_{MW} can be deduced from Eq. (6). First the microwave photovoltage is excluded by setting the rf current $I_1 = 0$. Then we only regard the microwave power dependent terms which depend on α_1 and β_1:

$$\Delta R_{\mathrm{MW}} = (U_0|_{I_1=0} - U_0|_{I_1=0,\alpha_1=0,\beta_1=0})/I_0 = R_A(-\alpha_1^2 \cos 2\alpha_0 - \beta_1^2 \cos^2\alpha_0)/2. \quad (17)$$

If the magnetization lies parallel or antiparallel to the dc current vector $\mathbf{I}_0$ along the stripe ($\alpha_0 = 0°$ or $\alpha_0 = 180°$) the AMR is maximal. In this case magnetization oscillation (α_1 and β_1) reduces ($-\cos 2\alpha_0 = -1$) the AMR by $\Delta R_{\mathrm{MW}} = -(\alpha_1^2 + \beta_1^2) R_A/2$ (negative photoresistance). In contrast, if the magnetization lies perpendicular to $\mathbf{I}_0$ ($\alpha_0 = 90°$, see Fig. 2) the resistance is minimal. In this case magnetization oscillation corresponding to α_1 will increase ($-\cos 2\alpha_0 = +1$) the AMR (positive photoresistance) by $\Delta R_{\mathrm{MW}} = +\alpha_1^2 R_A/2$ [oscillations corresponding to β_1 leave $\theta(t)$ constant in this case and do not change the AMR].

The next step is to calculate α_1 and β_1. The dc magnetic field dependence of $\alpha_1 = |m_x|/M_0 = |\chi_{xx} h_x + i\chi_{xy} h_y|/M_0$ and $\beta_1 = |m_y|/M_0 = |-i\chi_{xy} h_x + \chi_{yy} h_y|/M_0$ is proportional to that of $|\chi_{xx}|$, $|\chi_{xy}|$, and $|\chi_{yy}|$ given in Eq. (12) (imaginary symmetric and real antisymmetric Lorentz line shape). Squaring this results in symmetric Lorentz line shape:

$$\alpha_1^2 \propto \beta_1^2 \propto \left| \frac{\Delta H (H - H_0) + i \Delta H^2}{(H - H_0)^2 + \Delta H^2} \right|^2 = \frac{\Delta H^2}{(H - H_0)^2 + \Delta H^2}.$$

Hence

$$\alpha_1^2 = \frac{|A_{xx} h_x + i A_{xy} h_y|^2}{M_0^2} \frac{\Delta H^2}{(H - H_0)^2 + \Delta H^2},$$

$$\beta_1^2 = \frac{|A_{yy} h_y - i A_{xy} h_x|^2}{M_0^2} \frac{\Delta H^2}{(H - H_0)^2 + \Delta H^2}. \quad (18)$$

Using Eqs. (15) and (18), Eq. (17) transforms to

$$\Delta R_{\mathrm{MW}} = \frac{R_A}{(\alpha_G \omega/\gamma)^2 (2H_0 + M_0)^2} [-(H_0 + M_0)\cos 2\alpha_0 - H_0 \cos^2\alpha_0] \frac{\Delta H^2}{(H - H_0)^2 + \Delta H^2} \times |h_x \sqrt{H_0 + M_0} + i h_y \sqrt{H_0}|^2. \quad (19)$$

The strength of the microwave photoresistance is proportional to $1/\alpha_G^2$. Weak damping (small α_G) is therefore critical for a signal strength sufficient for detection. The magnetic field dependence shows symmetric Lorentz line shape.

The dependence of ΔR_{MW} on α_0 in Eq. (19) reveals a sign change and hence vanishing of the photoresistance at

$$\cos^2\alpha_0 = \frac{1}{2}\left(1 - \frac{H_0}{3H_0 + 2M_0}\right). \quad (20)$$

This means that the angle at which the photoresistance vanishes shifts from $\alpha_0 = \pm 45°$ and $\alpha_0 = \pm 135°$ (for $\omega \to 0$) to $\alpha_0 = \pm 54.7°$ and $\alpha_0 = \pm 125.3°$ respectively (for $\omega \to \infty$) when increasing ω. The reason for this frequency dependence is the frequency dependence of the ellipcity of **m** described at the end of Sec. II B.

D. Microwave photovoltage

The most obvious difference in appearance between the microwave photoresistance discussed in Sec. II C and the microwave photovoltage discussed in this paragraph is that the photoresistance is proportional to the square of the rf magnetization [see Eq. (17), $\alpha_1^2 \approx |m_x|^2/M_0^2$ and $\beta_1^2 \approx |m_y|^2/M_0^2$] while the photovoltage U_{MW} is proportional to the product of the rf magnetization and the rf current. Consequently, the photovoltage has a very different line shape: While the rf magnetization depends with Lorentz line shape on H [see Eq. (12)], I_1 is independent of H. The line shape is hence determined by the phase difference ψ between the rf magnetization component $\mathrm{Re}(m_x e^{-i\omega t})$ and the rf current $I_1 \cos \omega t$. This effect does not play a role in the case of photoresistance because there only one phase matters namely that of the rf magnetization. In contrast in photovoltage measurements a linear combination of symmetric and antisymmetric Lorentz line shapes is found. This will be discussed in detail in the following.

To isolate the microwave photovoltage in Eq. (6) the dc current I_0 is set to 0:

$$U_{\mathrm{MW}} = U_0|_{I_0=0} = -I_1\alpha_1\frac{R_A \sin 2\alpha_0 \cos\psi}{2}. \tag{21}$$

From Eq. (8) we follow with

$$\alpha_1 \cos\psi = \mathrm{Re}(m_x) = \mathrm{Re}(\chi_{xx}h_x + i\chi_{xy}h_y). \tag{22}$$

We split $h_x = h_x^r + ih_x^i$ and $h_y = h_y^r + ih_y^i$ into real (h_x^r, h_y^r) and imaginary (h_x^i, h_y^i) part. This enables us to isolate the real part in Eq. (21) using Eq. (14):

$$U_{\mathrm{MW}} = \frac{I_1 R_A \sin 2\alpha_0}{2M_0}\left\{\frac{(A_{xy}h_y^r + A_{xx}h_x^i)\Delta H^2}{(H-H_0)^2+\Delta H^2} + \frac{(A_{xy}h_y^i - A_{xx}h_x^r)\Delta H(H-H_0)}{(H-H_0)^2+\Delta H^2}\right\}. \tag{23}$$

Conclusively in contrast to the microwave photoresistance [$\Delta R_{\mathrm{MW}} \propto 1/\alpha_G^2$, see Eq. (19)] the photovoltage is only proportional to $1/\alpha_G \propto A_{xx,xy,yy}$. Thus good damping is less important for its detection.[31]

To understand the measurement results it will be necessary to transform the coordinate system of Eq. (23) to (x', y, z'). In this coordinate system the rf magnetic field $\mathbf{h}$ is constant during rotation as described in Eq. (33).

To better understand the photovoltage line shape we have a closer look on ψ: When sweeping H the rf magnetization phase is shifted by ψ_m with respect to the resonance case ($H=H_0$). The rf current has a constant phase ψ_I which is defined with respect to the magnetization's phase at resonance. The impact of the dc magnetic field H on the rf current (I_1, ψ_I) via the FMR is believed to be negligible:

$$\cos\psi = \cos(\psi_m - \psi_I) = \cos\psi_m \cos\psi_I + \sin\psi_m \sin\psi_I. \tag{24}$$

ψ is determined by the (complex) phase of χ_{xx}, χ_{xy}, and χ_{yy} with respect to the resonance case [$\mathrm{Re}(\chi_{xy,yy})=0$ at $H=H_0$] during magnetic field sweep [asymmetric Lorentz line shape; see Eq. (12)]:

$$\tan\psi_m = \frac{\mathrm{Im}\left(\frac{\Delta H(H-H_0)+i\Delta H^2}{(H-H_0)^2+\Delta H^2}/i\right)}{\mathrm{Re}\left(\frac{\Delta H(H-H_0)+i\Delta H^2}{(H-H_0)^2+\Delta H^2}/i\right)} = \frac{H_0-H}{\Delta H}. \tag{25}$$

It should be noted that according to the Landau-Liftshitz equation[28] $\mathbf{h}$ applies a torque on the magnetization and hence excites $\mathbf{m}^t$ transversal. That is why at resonance m_x shows a phase shift of 90° with respect to h_x. Consequently in Eq. (25) division by i is necessary (χ_{xx} and χ_{xy} become imaginary at resonance).

Equation (25) means that in case that the applied microwave frequency is higher than the FMR frequency ($H_0 > H$) $\psi_m > 0$ (note that $\mathbf{m}^t = \mathbf{m}e^{-i\omega t}$), $\mathbf{m}^t$ is delayed with respect to the resonant case. The other way around ($H_0 < H$) the FMR frequency is higher than that of the applied microwave field and $\mathbf{m}^t$ is running ahead compared to the resonance case. Using Eq. (25) we find

$$\cos\psi_m = \frac{\Delta H}{\sqrt{(H-H_0)^2+\Delta H^2}}. \tag{26}$$

Inserting Eqs. (18) and (24)–(26) into Eq. (21) gives

$$U_{\mathrm{MW}} = -\frac{R_A I_1 \sin 2\alpha_0}{2}\frac{|A_{xx}h_x + iA_{xy}h_y|}{M_0}\left(\frac{\Delta H^2 \cos\psi_I}{(H-H_0)^2+\Delta H^2} - \frac{(H-H_0)\Delta H \sin\psi_I}{(H-H_0)^2+\Delta H^2}\right). \tag{27}$$

The dependence on H takes the form of a linear combination of symmetric and antisymmetric Lorentz line shape with the ratio $1:\tan\psi_I$. The symmetric line shape contribution ($\propto \Delta H$) arises from the rf current contribution that is in phase with the rf magnetization at FMR and the antisymmetric from that out-of-phase. This gives a nice impression of the phase ψ_I of the rf current determining the line shape of the FMR.

E. Vectorial description of the photovoltage

To complete the discussion of the microwave photovoltage we want to return to the approach used by Juretschke[23] to demonstrate that it is consistent with the description above. In Sec. II A we started with Ohm's law [scalar equation (1)]. There we integrate an angle- and time-dependent resistance. Here we want to start with the vectorial notation of Ohm's law used in Juretschke's publication [Eq. (1) (Ref. 23)]. This integrates AMR and anomalous Hall effect AHE. ρ is the resistivity of the sample and $\Delta\rho$ that additionally arising from AMR. R_H is the anomalous Hall effect constant:

$$\mathbf{E} = \rho\mathbf{J} + (\Delta\rho\mathbf{M}^2)(\mathbf{J}\cdot\mathbf{M})\mathbf{M} - R_H\mathbf{J}\times\mathbf{M}. \tag{28}$$

We split $\mathbf{M} = \mathbf{M}_0 + \mathbf{m}^t$ and the current density $\mathbf{J} = \mathbf{J}_0 + \mathbf{j}^t$ into their dc ($\mathbf{M}_0$ and $\mathbf{J}_0$) and rf contributions [$\mathbf{m}^t = \mathrm{Re}(\mathbf{m}e^{-i\omega t})$ and $\mathbf{j}^t = \mathbf{j}\cos\omega t$]. Constance of $|\mathbf{M}|$ allows $\mathbf{m}^t = (m_x^t, m_y^t, 0)$ in first order approximation only to lie perpendicular to $\mathbf{M}_0 = (0,0,M_0)$. To select the photovoltage we set $\mathbf{J}_0 = 0$ and approximate equation (28) to second order in $\mathbf{j}^t$ and $\mathbf{m}^t$. The terms of zeroth order in both $\mathbf{j}^t$ and $\mathbf{m}^t$ represent the sample resistance without microwave exposure and are not discussed here. The terms of first order in either $\mathbf{j}^t$ or $\mathbf{m}^t$ (but not both) have zero time average and do not contribute to the microwave induced dc electric field $\mathbf{E}_{\mathrm{MW}}$. Only the terms that are simultaneously of first order in $\mathbf{j}^t$ and $\mathbf{m}^t$ contribute to $\mathbf{E}_{\mathrm{MW}}$ [compare Eq. (4) from Juretschke[23]]:

$$\mathbf{E}_{\mathrm{MW}} = \frac{\Delta\rho}{M_0^2}\langle(\mathbf{j}^t\mathbf{m}^t)\mathbf{M}_0 + (\mathbf{j}^t\mathbf{M}_0)\mathbf{m}^t\rangle - R_H\langle\mathbf{j}^t\times\mathbf{m}^t\rangle. \tag{29}$$

The $\Delta\rho$ dependent term represents the photovoltage contribution arising from AMR and the R_H dependent term that arising from AHE. Note that a second order of $\mathbf{m}^t$ appears when applying a dc current $\mathbf{J}_0 \neq 0$. It represents the photoresistance discussed in Sec. II C. However, it we will not be discussed here.

In the following we will calculate the photovoltage in our Permalloy film stripe considering its geometry which fixes the current direction. $\mathbf{j}^t = j_z^t, \mathbf{z}'$ along the stripe ($\mathbf{z}'$ is the unit

vector along the Permalloy stripe). The small dimensions perpendicular to the stripe ($\ll L$) will prevent the formation of a perpendicular rf current. A similar approximation of a metal grating forming a linear polarizer has been considered previously.[9] The photovoltage U_{MW} is also measured along the stripe (length vector $\mathbf{L}=\mathbf{z}'\times 2.4$ mm). When fluctuations of $\mathbf{E}_{\mathrm{MW}}$ along the stripe are neglected considering the large microwave wavelength, $\lambda \approx 20\ \mathrm{mm} \gg 2.4\ \mathrm{mm}=L$, we find U_{MW} by multiplying $\mathbf{E}_{\mathrm{MW}}$ with $\mathbf{L}$:

$$U_{\mathrm{MW}} = \int_0^L \mathbf{E}_{\mathrm{MW}} d\mathbf{z}' \approx \mathbf{E}_{\mathrm{MW}} \cdot \mathbf{L}$$

$$= \frac{\Delta\rho L}{M_0^2}\langle j_{z'}^t(\mathbf{z}'\mathbf{m}^t)(\mathbf{M}_0\mathbf{z}') + j_{z'}^t(\mathbf{z}'\mathbf{M}_0)(\mathbf{m}^t\mathbf{z}')\rangle - 0$$

$$= \frac{\Delta\rho L}{M_0}\langle j_{z'}^t, m_x^t\rangle \sin(2\alpha_0). \tag{30}$$

This is equivalent to Eq. (21) which can be verified by replacing $\Delta\rho j_{z'}^t L = R_A I_1 \cos(\omega t)$ and $m_x^t = \alpha_1 M_0 \cos(\omega t - \psi)$. Time averaging results in the additional factor $\cos(\psi)/2$.

As discussed in Sec. II F the contribution belonging to the anomalous Hall effect has no impact in this geometry because it can only generate a photovoltage perpendicular to the rf current, i.e., perpendicular to the stripe.

Comparing our results to those of Juretschke and Egan,[23,31] we note that an equation similar to Eq. (30) has been derived in the formula for e_{y0} in Eq. (31) in Juretschke's publication.[23] There the photovoltage is measured parallel to the rf current as done in our stripe. However, it has to be noted that the coordinate system is defined differently. The major difference compared to our system is that we use a stripe shaped film to lithographically define the direction of the rf current I_1, while the direction of $\mathbf{h}$ is left arbitrary. In contrast to that, Juretschke and Egan[23,31] define the direction of the rf magnetic field and rf current by means of their microwave setup. In Eq. (31) (e_{y0}) from Juretschke[23] this results in the additional factor $\cos\theta$ (which is equivalent to $\cos\alpha_0$ in our work) compared to Eq. (30). This arises from the definition of $\mathbf{h}$ fixed parallel to the rf current [compare Eq. (33)].

F. Other magnetoresistive effects that couple spin and charge current

In this section we present other magnetoresistive effects which can generate photovoltage and photoresistance like the AMR. This selection gives a broader view on the range of effects for which the photovoltage and photoresistance can be discussed in terms of the analysis presented in this work. In principle every magnetoresistive effect can modulate the sample resistance and thus rectify some of the rf current to photovoltage.

One magnetoresistive effect is the anomalous Hall effect AHE in ferromagnetic metals that was (together with the AMR) the basis for the discussion of Juretschke.[23] There a current with perpendicular magnetization generates a voltage perpendicular to both. Under microwave exposure this alternates with the microwave frequency but in an asymmetric way due to the modulated AHE arising from magnetization precession. The asymmetric voltage has a dc contribution (photovoltage),[31] which can be measured using a two-dimensional ferromagnetic film with the magnetization neither parallel nor perpendicular to it. The photovoltage induced by AHE appears in the film plane perpendicular to the rf current and is small[25] for Permalloy ($Ni_{80}Fe_{20}$). Also a photoresistive effect which alters the AHE can be expected if the magnetization lies out-of-plane.

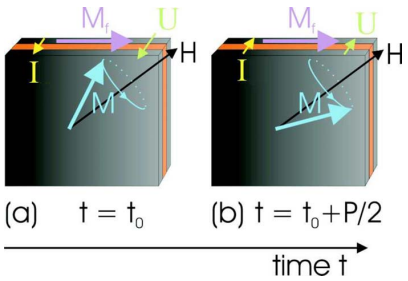

FIG. 5. (Color online) Microwave photovoltage in a GMR/TMR heterostructure [ferromagnetic ($\mathbf{M}$)/nonferromagnetic/ferromagnetic ($\mathbf{M}_f$)]: The dynamic magnetization $\mathbf{M}$ precesses (period P) in phase with the current $\mathbf{I}$. (a) $\mathbf{M}$ lies almost perpendicular to $\mathbf{M}_f$: High GMR/TMR. (b) $\mathbf{M}$ lies almost parallel to $\mathbf{M}_f$: Low GMR/TMR $\Rightarrow$ nonzero time average of the voltage $\mathbf{U}$.

Other examples for magnetoresistive effects are GMR and TMR structures which exhibit a photovoltage mechanism similar to that in AMR films. The difference is that there the direction of the ferromagnetic layer magnetization with respect to the current does not matter. Effectively instead the direction of the magnetization $\mathbf{M}$ of one ferromagnetic layer with respect to that of another layer is decisive (see Fig. 5). Exciting the FMR in one layer yields again oscillation of the sample resistance $R(t)$ and thus gives the corresponding rf voltage $U(t)$ a nonzero time average (photovoltage).[4,32] This is usually stronger than that from AMR films due to the generally higher relative strength of GMR and TMR compared to AMR.

It should be noted that in current studies of the microwave photovoltages effect in multilayer structures, the focus is on interfacial spin transfer effects.[4–8,19–21,32] It remains an intriguing question whether interfacial spin transfer effects and the effect revealed in our approach based on phenomenological magnetoresistance might be unified by a consistent microscopic model, as Silsbee *et al.* have demonstrated for describing both bulk and interfacial spin transport under rf excitation.[24]

Multilayer structures also provide a nice example that photovoltage generation can also be reversed when the oscillating magnetoresistance, transforms a dc current into an rf voltage,[33] instead of transforming an rf current into a dc voltage (photovoltage). This gives a new kind of microwave source and seems—although weaker—also possible in AMR and AHE samples.

It can be reasoned that like microwave photovoltage the microwave photoresistance can also be based on GMR or TMR instead of AMR: When aligning the two magnetiza-

tions of both ferromagnetic layers in a GMR or TMR structure microwave induced precession of one magnetization is expected to increase the GMR/TMR because of the arising misalignment with the other magnetization. With the magnetizations initially antiparallel the opposite effect, a microwave induced resistance decrease, is expected. Further work demonstrating these effects would be interesting.

III. PHOTOVOLTAGE MEASUREMENTS

A. Measurement setup

The sample we use to investigate the microwave photovoltage consists of a thin (d=49 nm) Permalloy (Ni 80%, Fe 20%) film stripe (200 μm wide and 2400 μm long) with 300×300 μm^2 bond pads at both ends (see Fig. 3). These are connected via gold bonding wires and coaxial cables to a lock-in amplifier. For auxiliary measurements (e.g., Hall effect) six additional junctions are attached along the stripe (see Fig. 3).

The resistance of the film stripe is $R_0+R_A=85.0\ \Omega$ for parallel and $R_0=83.6\ \Omega$ for perpendicular magnetization. Hence the conductance is $\sigma=1/\rho=2.9\times10^6\ \Omega^{-1}\,\mathrm{m}^{-1}$ and the relative AMR is $\Delta\rho/\rho=1.7\%$. The absolute AMR is $R_A=1.4\ \Omega$. This is in good agreement with previous publications.[9–11]

The film is deposited on a 0.5 mm thick GaAs single crystal substrate, and patterned using photolithography and lift off techniques. The substrate is mounted on a 1 mm polyethylene print circuit board which is glued to a brass plate holding it in between the poles of an electromagnet. This provides the dc magnetic field $B=\mu_0 H$ (maximal $\approx$1 T). The sample is fixed 1 mm behind the end of a WR62 (15.8 $\times$7.9 mm) hollow brass waveguide which is mounted normal to the Permalloy film plane. The stripe is fixed along the narrow waveguide dimension. In the K_u band (12.4–18 GHz), that we use in our measurements, the WR62 waveguide only transmits the TE_{01} mode.[1] The stripe was fixed with respect to the waveguide but was left rotatable with respect to **H**. This allows the stripe to be parallel or perpendicular to **H**, but keeps the magnetic field always in the film plane. A high precision angle readout was installed to indicate α_0. (See Fig. 6).

The waveguide is connected to an HP83624B microwave generator by a coaxial cable supplying frequencies of up to 20 GHz and a power of 200 mW. The power is however later significantly reduced by losses occurring within the coaxial cable, during the transfer to the hollow waveguide and by reflections at the end of the waveguide. Microwave photovoltage measurements are performed sweeping the magnetic field while fixing the microwave frequency. The sample is kept at room temperature.

To avoid external disturbances the photovoltage was detected using a lock-in technique: A low frequency (27.8 Hz) square wave signal is modulated on the microwave CW output. The lock-in amplifier, connected to the Permalloy stripe, is triggered to the modulation frequency to measure the resulting square wave photovoltage across the sample. Instead of the photovoltage also the photocurrent can be measured.[10]

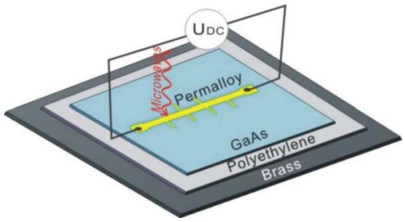

FIG. 6. (Color online) Sketch of the measurement geometry. A 1 mm thick polyethylene plate is glued on a brass holder. On top of the polyethylene a GaAs substrate is glued. On the substrate the Permalloy (Py) stripe is defined. This is electrically wired to a voltage amplifier for photovoltage measurements. For photoresistance measurements an additional current source is connected parallel to the voltage amplifier, which is not shown explicitly here.

Its strength I_0 can be found when setting $U_0=0$ in Eq. (6) (instead of $I_0=0$).

B. Ferromagnetic resonance

The measured photovoltage almost vanishes during most of the magnetic field sweep but shows one pronounced resonance of several μV. The strength and line shape of this resonance are strongly depending on α_0 and will be discussed in Sec. III C. A line shape dependence of the photovoltage on the microwave frequency is also found. The photovoltage with respect to the strength of the external magnetic field H and the microwave frequency $f=\omega/2\pi$ can be seen in a gray scale plot in Fig. 7, in which the resonance can be identified with the FMR by the corresponding fits (dashed line) because the Kittel equation (9) (Ref. 30) for ferromagnetic planes (our Permalloy film) applies. The magnetic parameters found are $\mu_0 M_0\approx1.02$ T and $\gamma\approx2\pi\mu_0\times28.8$ GHz/T. They are in good agreement with previous publications.[9,10]

The exact position of the FMR is obscured by its strongly varying line shape. We overcome this problem by the pro-

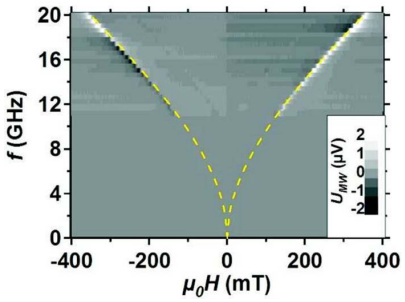

FIG. 7. (Color online) Gray scale plot of the measured frequency and magnetic field dependence of the microwave photovoltage at $\alpha_0=47°$. The dashed line shows the calculated FMR frequency [see Eq. (9)]. The photovoltage intensity is strongly frequency dependent because of the frequency dependent waveguide transmission.

ductive line shape analysis in Sec. III C. It is found that H_0 is slightly dependent on α_0. This can be attributed to a small demagnetization field perpendicular to the stripes but within the film plane arising from the finite stripe dimensions in this direction. So, when $\mathbf{M}_0$ lies perpendicular to the stripe, H_0 slightly increases compared to the value fulfilling the Kittel equation for a plane [see Eq. (9)]. In the parallel and perpendicular case we use the approximation of our film stripe as an ellipsoid, where we can use the corresponding Kittel equation[30] (demagnetization factors N_x, N_y, and N_z with respect to the dc magnetic field):

$$\omega = \gamma\sqrt{[H_0 + (N_x - N_z)M_0][H_0 + (N_y - N_z)M_0]}. \quad (31)$$

The difference of the resonance field between the case that $\mathbf{M}_0$ lies in the film plane parallel to the stripe and perpendicular is 1.6 mT (0.7%) at $f=15$ GHz. From this we can calculate the small demagnetization factor $N_{x'}=0.085\%$ perpendicular to the Permalloy stripe within the film plane using Eq. (31). From the sum rule[34] follows: $N_y=1-N_{x'}-N_{z'}=1-0.085\%-0=99.915\%$. $N_{z'}$ (parallel to the stripe) can be assumed to be negligibly small. This matches roughly with the dimension of the height to width ratio (49 nm:200 μm) of the sample. For the stripe presented in Sec. IV similar but stronger demagnetization effects are found.

Now we will have a closer look on the magnetic properties of the investigated film. Again at $f=15$ GHz we find using Eq. (10): $H_0=0.219$ T. Using asymmetric Lorentz line shape fitting as described in Sec. III C we get $\alpha_G=0.0072$. Consequently, $A_{xx}=231.1$, $A_{xy}=97.1$, and $A_{yy}=40.8$ according to Eq. (13).

Because of $\alpha_G=0.0072$ the magnetization precession does impressive $n\approx 22$ turns before being damped to $1/e$ of its initial amplitude ($n=1/2\pi\alpha_G$). Therefore the ellipcity of $\mathbf{m}$ is almost independent of $\mathbf{h}$ (see Sec. II B). It can be calculated from Eq. (16) that $m_x/m_y=2.38i$ at $\omega/2\pi=15$ GHz.

To check the validity of our approximation ($d \ll \delta$, see Sec. II B) we will now regard the skin depth δ at $f=15$ GHz in our sample ($d=49$ nm). For $\mu=\mu_0$ (away from the FMR) we find $\delta=\sqrt{2/\omega\mu\rho}=2.4$ μm. Hence $\delta \gg d$. This is in accordance with our approximation that $\mathbf{h}$ is almost constant within the Permalloy film (see II B). However, in the vicinity of the FMR: $|\mu| \gg \mu_0$ and for the same frequency and conditions as above: $\mu_L=(1+\chi_L)\mu_0=133i\mu_0$ at the FMR. Thus we approximate $\delta_{\mathrm{FMR}}=\sqrt{2/\omega|\mu_L|\rho}=210$ nm. Hence δ_{FMR} is still significantly larger than d and our approximation is still valid.

Finally we can summerize that for samples with weak damping ($\alpha_G \ll \omega/\omega_M$) like ours the approximation $H\approx H_0$ gives results with impressive precision (see Fig. 8) because its discrepancies are limited to the unimportant magnetic field ranges with $|\chi_{xx}|$, $|\chi_{xy}|$, and $|\chi_{yy}| \ll 1$, which are far away from the FMR.

C. Asymmetric Lorentz line shape

Although in Sec. III B the frequency dependence of the FMR field is verified with the gray scale plot in Fig. 7, it is still desirable to receive a more accurate picture of the corresponding line shape which is found to be strongly angular dependent (see Fig. 8). In Eq. (27) it is shown that the magnetic field dependence of U_{MW} exhibits asymmetric Lorentz line shape around $H=H_0$. Hence U_{MW} takes the form

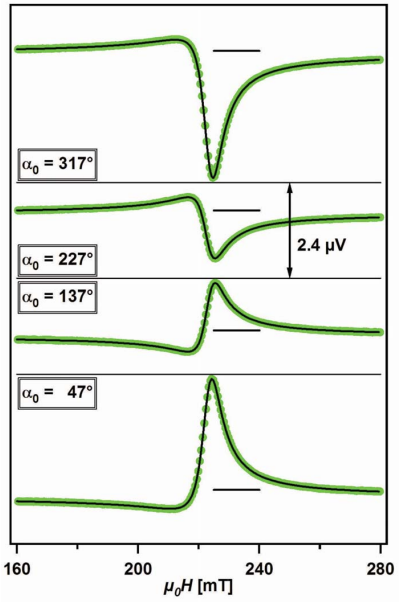

FIG. 8. (Color online) Fitting (black line) of the microwave photovoltage signal (dots) for different angles α_0 at $f=15$ GHz. The black horizontal bars indicate zero signal.

$$U_{\mathrm{MW}} = U_{\mathrm{MW}}^{\mathrm{SYM}} + U_{\mathrm{MW}}^{\mathrm{ANT}} = U_0^{\mathrm{SYM}}\frac{\Delta H^2}{(H-H_0)^2+\Delta H^2} + U_0^{\mathrm{ANT}}\frac{\Delta H(H-H_0)}{(H-H_0)^2+\Delta H^2}. \quad (32)$$

This is used to fit the magnetic field dependence of the photovoltage in Fig. 8. For clearness the symmetric (absorptive) and antisymmetric (dispersive) contributions are shown separately in Fig. 9. A small constant background is found and added to the antisymmetric contribution. The background could possibly arise from other weak nonresonant photovoltage mechanisms.

The fits agree in an unambiguous manner with the measured results. Hence they can be used to determine the Gilbert damping parameter with high accuracy: $\alpha_G \approx \gamma\Delta H/\omega \approx (0.72\% \pm 0.015\%)$. However, if the magnetization lies parallel or perpendicular to the stripe the photovoltage vanishes [see Eq. (21)]. Hence we can only verify α_G when the magnetization is neither close to being parallel nor perpendicular to our stripe.

The corresponding $\alpha_G=1/\omega\tau$ in the Nickel sample of Egan and Juretschke,[31] can be estimated using the ferromagnetic relaxation time τ from their Table II. It lies in between $\alpha_G=0.12$ and 0.18, so being more than 16 times higher than the value in our sample. This makes the line shape approximation of Sec. II D invalid for their case. Consequently, a

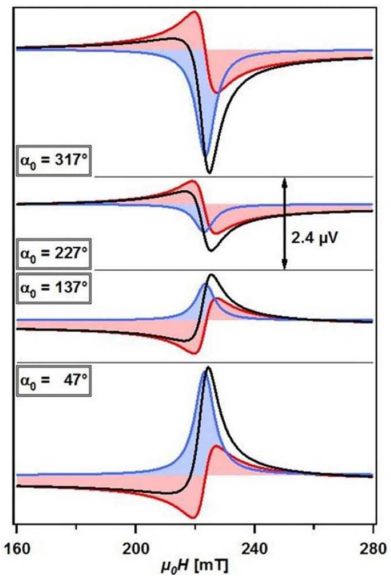

FIG. 9. (Color online) Symmetric and antisymmetric contributions to the asymmetric Lorentz line shape fit from Fig. 8 (black). A small constant background is found and added to the antisymmetric contribution.

much more elaborated line shape analysis[23] appears necessary.

In Fig. 8 the photovoltage along the stripe is presented at four different angles α_0. The signal to noise ratio is about 1000 because of the carefully designed measurement system, where the noise is suppressed to less than 5 nV. Because of this good sensitivity we can verify the matching of our theory from Sec. II with the measurement results in great detail. (See Fig. 10.)

In the following we want to investigate the angular dependence in detail. Therefore, we transform the coordinate system of Eq. (23) according to the transformation presented in

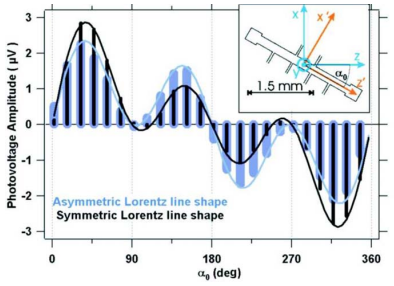

FIG. 10. (Color online) Bars show the angular dependence of the amplitude of the symmetric (U_0^{SYM}, thin bars) and antisymmetric (U_0^{ANT}, thick bars) contribution to the microwave photovoltage at $f=15.0$ GHz. Note that both the symmetric and antisymmetric contribution vanish for $\alpha_0=0°$, 90°, 180°, and 270°. The lines represent the corresponding fits by means of Eq. (34). The inlet shows the geometry of the investigated Permalloy stripe and the coordinate systems from Fig. 3 (note: $\mathbf{z}\|\mathbf{H}$).

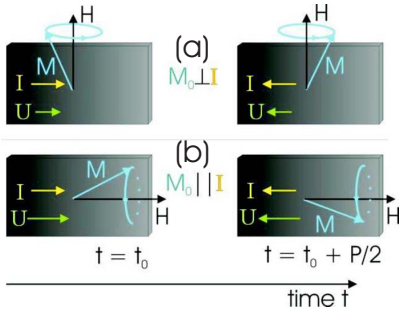

FIG. 11. (Color online) When the magnetic field **H** lies parallel or perpendicular to the stripe, the time average voltage vanishes. (a) **H** lies perpendicular to **I**: Precession of the magnetization **M** leaves (after half a period $P/2$) the angle θ between the axis of **M** and **I** unchanged. Hence the AMR (and so voltage **U**) is also unchanged. The photovoltage vanishes. (b) **H** is parallel to **I**: θ and the AMR stay constant during the precession of **M** and the time average of **I** is zero. This means that only when **H** is neither parallel nor perpendicular to the stripe a photovoltage is generated.

Sec. II A. Doing so we can separate the contributions from $h_{x'}$, h_y, and $h_{z'}$:

$$U_{\mathrm{MW}} = \frac{R_A I_1 \sin(2\alpha_0)}{2M_0}\left\{[A_{xy}h_y^r + A_{xx}(h_{x'}^i \cos\alpha_0 - h_{z'}^i \sin\alpha_0)]\frac{\Delta H^2}{(H-H_0)^2+\Delta H^2} + [A_{xy}h_y^i + A_{xx}(h_{z'}^r \sin\alpha_0 - h_{x'}^r \cos\alpha_0)]\frac{\Delta H(H-H_0)}{(H-H_0)^2+\Delta H^2}\right\}. \tag{33}$$

$h_{x'}$, h_y, and $h_{z'}$ are fixed with respect to the hollow brass waveguide and its microwave configuration and do not change when α_0 is varied.

We find that the angular dependence of the line shape in Eq. (33) exhibits two aspects: An overall factor $\sin(2\alpha_0)$ and individual factors ($\sin\alpha_0$, $\cos\alpha_0$, and 1) for the terms belonging to the different spatial components of **h**. The overall factor $\sin(2\alpha_0)$ arises from the AMR photovoltage mechanism and results in vanishing of the photovoltage signal at $\alpha_0=0°$, 90°, 180°, and 270°. This means if $\mathbf{M}_0$ lies either parallel, antiparallel, or perpendicular to the stripe axis. This is illustrated in Fig. 11 and is clearly observed in our measurements (see Fig. 10). We take this as a strong support for the photovoltage being really AMR based.

Another support comes from the similarity with the planar Hall effect.[35] The planar Hall effect generates a voltage U_{PHE} perpendicular to the current in ferromagnetic samples (width W) when the magnetization $\mathbf{M}_0$ lies in the current-voltage plane. It arises as well from AMR and vanishes when $\mathbf{M}_0$ lies either parallel or perpendicular to the current axis.

The similarity arises because of the AMR only generating a transversal resistance when the current is not lying along the principle axis of its resistance matrix (parallel or perpen-

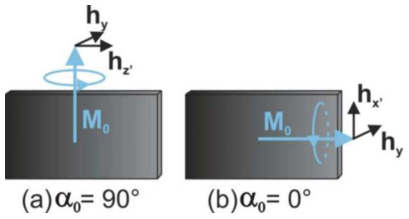

FIG. 12. (Color online) Angular dependent coupling of the magnetization **M** to the dynamic magnetic field $\mathbf{h}=(h_{x'},h_y,h_{z'})$. Only the components of **h** perpendicular to $\mathbf{M}_0$ can excite precession of **M** and therefore generate a dynamic **m**. h_y is always exciting **m**. The excitation strength of $h_{x'}$ and $h_{z'}$ is angular dependent [compare Eq. (33)]. Here the two symmetry cases are shown: **M** (a) perpendicular (only $h_{z'}$ and h_y can excite **M**) and (b) parallel (only $h_{x'}$ and h_y can excite **M**) to the stripe.

dicular to the magnetization). This is the same geometrical restriction as shown above for the microwave photovoltage [see Eq. (21) and Fig. 11].

We want to emphasize the importance that in any of these microwave photovoltage experiments, due to the unusually strong angle dependence, it is important to pay attention to the exact angle adjustment of the sample with respect to the dc magnetic field **H** when measuring under high symmetry conditions (**H** parallel or perpendicular to the stripe) to avoid involuntary signal changes due to small misalignments. As found in 90° out-of-plane configuration[10] already a misalignment as small as a tenth of a degree can yield a tremendous photovoltage change in the vicinity of the FMR.

Finally we want to come back to the individual angular dependencies of the photovoltage contributions arising from the different external magnetic field components. In addition to the $\sin(2\alpha_0)$ proportional dependence of U_{MW} on m_x, also the strength with which m_x is excited by **h** depends on α_0. This is displayed in Fig. 12 and reflected by the three terms in Eq. (33) depending on $h_{x'}$, h_y, and $h_{z'}$ with $\cos\alpha_0$, 1, and $\sin\alpha_0$ factors, respectively. Hence the symmetric U_0^{SYM} and antisymmetric U_0^{ANT} Lorentz line shape contribution to U_{MW} are fitted in Fig. 10 with

$$U_0^{\mathrm{SYM}} = [U_{z'}^S \sin(\alpha_0) + U_{x'}^S \cos(\alpha_0) + U_y^S]\sin(2\alpha_0),$$

$$U_0^{\mathrm{ANT}} = [U_{z'}^A \sin(\alpha_0) + U_{x'}^A \cos(\alpha_0) + U_y^A]\sin(2\alpha_0). \quad (34)$$

From $U_{z'}^S$, $U_{x'}^S$, and U_y^A the dynamic magnetic field components $h_{z'}^i$, $h_{x'}^i$, h_y^i which are 90° out-of-phase with respect to the rf current I_1 can be determined using Eq. (33) and from $U_{z'}^A$, $U_{x'}^A$, and U_y^S we find $h_{z'}^r$, $h_{x'}^r$, and h_y^r which are in phase with I_1.

In principle I_1 can be separately deduced using the bolometric effect[12] as discussed in Sec. IV A. However, for the sample used here our usage of multiple stipes does not allow us to address the bolometric heating to one single stripe. Consequently the strength of I_1 is unknown so that we can not determine **h**, but only $\mathbf{h}I_1$.

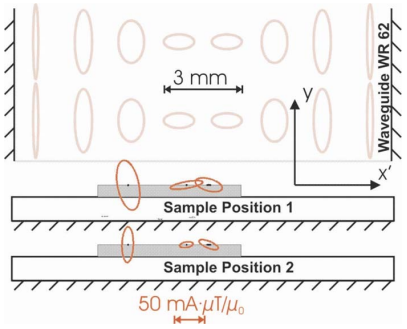

FIG. 13. (Color online) Direction and ellipticity of the rf magnetic field **h** displayed by showing the path $I_1\cdot\mathbf{h}$ passes during one cycle. This is shown at the location of the three stripes (these lie normal to the picture on top of the gray GaAs substrate; the 200 μm wide stripe to the right) for two sample positions. $I_1\cdot\mathbf{h}$ was determined by means of Eq. (33). The upper right path corresponds to the $I_1\cdot\mathbf{h}$ from Table I. The hatched edges indicate metal surfaces reflecting microwaves. Within the waveguide the rf magnetic field **h** corresponding to the TE_{10} mode is displayed in the background.

Besides, considering the special dynamic magnetic field configuration in our rectangular hollow waveguide no rf magnetic field component $h_{z'}$ is expected to be generated along the waveguides narrow dimension (z' axis) by the TE_{01} mode[1] (which is the microwave configuration of our waveguide). It follows that the $\sin(\alpha_0)$ terms in Eq. (34) vanishes. This results in the additional symmetry $U_{\mathrm{MW}}(\alpha_0) = -U_{\mathrm{MW}}(-\alpha_0)$, which is clearly observed in our measurements (see Fig. 10). This symmetry was broken when we used a round waveguide.

The vanishing of $h_{z'}$ in our waveguide will allow us to plot the direction of **h** two-dimensional (instead of three-dimensional) in Fig. 13. A small deviation from the symmetry $U_{\mathrm{MW}}(\alpha_0)=-U_{\mathrm{MW}}(-\alpha_0)$ is however found and arises from a small $h_{z'}$ component (see Table I) which is not displayed in Fig. 13. It might arise from the fact that the rf microwave magnetic field **h** at the waveguide end already deviates from the TE_{01} mode.

TABLE I. Determination of the rf magnetic field **h** at the 200 μm wide stripe at 1 mm distance from the waveguide end by means of Eq. (33). $U_{x',y,z'}^S$, $U_{x',y,z'}^A$: Measured amplitudes of the contributions to the symmetric and antisymmetric Lorentz line shape of U_{MW} [see Eq. (34)] with the angular dependence belonging to x', y, and z', respectively (taken from the fitting in Fig. 10). $A_{xx,xy}$: Corresponding amplitudes of $\chi_{xx,xy}$. $h_{x',y,z'}^r$, $h_{x',y,z'}^i$: rf magnetic field strength calculated from $U_{x',y,z'}^S$, $U_{x',y,z'}^A$ (in-phase and 90° out-of-phase contribution with respect to the current).

	$U_{x',y,z'}^S$	$U_{x',y,z'}^A$	A_{xx}	A_{xy}	$I_1 h_{x',y,z'}^r$	$I_1 h_{x',y,z'}^i$
	(μV)				(mA μT/μ_0)	
x'	+2.60	+2.55	231.1		−15.7	+16.4
y	+0.95	+0.30		97.1	+14.0	+4.4
z'	+0.12	0.00	231.1		0.0	−0.7

D. Determination of the rf magnetic field direction

Using the different angular dependencies of the three symmetric and three antisymmetric terms in Eq. (33) $\mathbf{h}I_1$ can be determined. We make the assumption that the stripe itself does not influence the rf magnetic field configuration, what is at least the case when further reducing its dimensions. Thus the film stripe becomes a kind of detector for the rf magnetic field **h**.

To test this an array of 36 additional 50 μm wide and 20 μm distant Permalloy stripes of the same height and length as the 200 μm wide stripe described above (see Sec. III A) was patterned beside this one. The 50 μm wide stripes were connected with each other at alternating ends to form a long meandering stripe.[9] Four stripes were elongated on both ends to 300×300 μm^2 Permalloy contact pads. For the outer two stripes and the single 200 μm stripe $\mathbf{h}I_1$ is calculated from the measured photovoltage using Eq. (23). Table I shows the measured voltage and the corresponding $\mathbf{h}I_1$ for the 200 μm stripe at 1 mm distance from the waveguide. $\mathbf{h}I_1$ for all three stripes is displayed in Fig. 13, while positioning the sample at two distances (1 and 3.5 mm, respectively) from the waveguide end. For comparison the rf magnetic field **h** configuration of the TE_{01} mode is displayed in the background. From other measurements we can estimate that I_1 lies somewhere in the 1 mA range.

It is worth noting that possible inhomogeneities of the rf magnetic field **h** within the Permalloy stripes will be averaged because U_{MW} is linear in **h**. Determining the sign of the rf magnetic field components from the photovoltage contributions signs exhibits a certain complexity because a lot of attention has to be paid to the chosen time evolution ($e^{i\omega t}$ or $e^{-i\omega t}$) and coordinate system (right hand or left hand). However, the sign only reflects the phase difference with respect to the rf current. The rf current is admittedly not identical for different stripe positions. Consequently the comparison of the rf magnetization phase at different stripe locations is obscured.

It is a specially interesting point concerning microwave photovoltage that the phase of the individual components of the rf magnetic field with respect to the rf current, and therefore also with respect to each other can be determined. The phase information is encoded in the line shape, which is a particular feature of the microwave photovoltage described in this work.

At this point only determining $\mathbf{h}I_1$ is possible because I_1 is unknown. However, in Sec. IV A, an approach to determine I_1 using the bolometric effect is presented. Using this approach the bolometric photoresistance is the perfect supplement for the photovoltage. It delivers unknown I_1 with almost no additional setup.

IV. PHOTORESISTANCE MEASUREMENTS

The principle difficulties when detecting the AMR induced photoresistance are to increase the microwave power for a sufficient signal strength and to reduce the photovoltage signal, which is in general much stronger and superimposes with the photoresistance. We overcome the microwave power problem by using high initial microwave power (316 mW) and a coplanar waveguide (CPW),[10] which emits the microwaves as close as possible to the Permalloy film stripe ($0.137\times20\times2450$ μm^3) with which we detect the photoresistance. Its resistance is found to be $R=880$ Ω and the AMR $R_A=15$ Ω. Its magnetic properties (γ, M_0) are almost identical to that of the sample investigated in Sec. III. We use again lock-in technique like in III A with now an additional dc current from a battery to measure resistance instead of voltage. The strong microwave power results in strong rf currents within the sample which give a specially strong photovoltage signal [see Eq. (27)]. To achieve a sufficiently strong photoresistance signal the dc current I_0 and rf current I_1 have to be increased to the maximal value that does not harm the sample (a few mA, hence $I_0\approx I_1$).

Ignoring the trigonometric factors $\sin 2\alpha_0$, $\cos 2\alpha_0$, and $\cos\psi$ as well as the photoresistance term depending on β_1 (that is always smaller than α_1) the photovoltage signal [$U_{MW}=\alpha_1\sin(2\alpha_0)\cos\psi R_A I_1/2$, Eq. (21)] and the photoresistance signal [$\Delta R_{MW}I_0\approx-\alpha_1^2\cos(2\alpha_0)R_A I_0/2$, Eq. (17)] become almost identical. But the major difference is that the photoresistance is multiplied by α_1^2 and the photovoltage only by α_1. As α_1 is particularly small ($<1°$) in our experiments, this means that $\Delta R_{MW}I_0$ is much smaller than U_{MW}. However, suppressing U_{MW} is possible because it vanishes for $\alpha_0=0°$, 90°, 180°, 270° [see Eq. (21)]. A very precise tuning of α_0 with an accuracy below 0.1° is necessary to suppress U_{MW} below $\Delta R_{MW}I_0$. Fortunately in contrast to $|U_{MW}|$, $|\Delta R_{MW}|$ is maximal for $\alpha_0=0°$, 90°, 180°, 270°. In the following, we will first discuss the bolometric photoresistance arising from microwave heating of the sample and afterwards the AMR induced photoresistance that is discussed above.

A. Bolometric (nonresonant)

The AMR-induced ΔR_{MW} is not the only photoresistive effect present in our Permalloy film stripe. Also nonresonant heating by the microwave rf current I_1 results in a (bolometric) photoresistance. The major difference compared to the AMR-based photoresistance is that the bolometric photoresistance is almost independent of the applied dc magnetic field H and that its reaction time to microwave exposure is much longer (in the order of ms) than that of the AMR-based photoresistance ($1/\alpha_G\omega$, in the order of ns).[12] The nonresonant bolometric photoresistance is found with a typical strength of $(\Delta R/R)/P=0.2$ ppm/mW (see Fig. 14).

The bolometric heating power P_{bol} arises from resistive dissipation of the rf current I_1 in the sample ($P_{bol}=\langle RI^2\rangle=RI_0^2+RI_1^2/2$). This can hence be used to determine I_1, which is otherwise an unknown in Eq. (27). I_1 can be determined for example by finding the corresponding dc current I_0 with the same bolometric resistance change. However, especially in the sample we use the thermal conductivity of the GaAs crystal on which our Permalloy stripes were deposited is so high (55 W/m K) that the different stripes are strongly thermally coupled. Thus we cannot address the bolometric signal of one stripe solely to the rf current of the same stripe. This effect was verified comparing the resistance changes from one stripe while applying a dc current through an other stripe. Hence determination of $|I_1|$ by means of Eq. (27) is

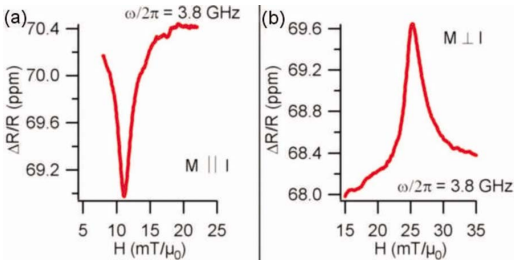

FIG. 14. (Color online) Photoresistance ΔR_{MW} measurement (stripe resistance R). The curves show the difference between the signals ΔU with $I_0=+5$ mA and $I_0=-5$ mA at $P=316$ mW: $\Delta R=[\Delta U(I_0=+5\ \mathrm{mA})-\Delta U(I_0=-5\ \mathrm{mA})]/10$ mA. The subtraction suppresses the photovoltage dependence on absolute $|I_0|$ (for example from bolometric AMR change). For both curves the dc magnetic field **H** (and so **M**) was applied within the film plane, but for (a) parallel to the stripe (and hence to the dc current I_0) and for (b) perpendicular. A nonresonant background of about 70 ppm from bolometric photoresistance is found. It is decreases by about 1.2 ppm when the sample is turned from parallel to perpendicular configuration. This is caused by the 1.7% AMR which changes R and the bolometric signal proportionally. The FMR signal has almost Lorentz line shape and its position is significantly changing when the sample is turned from parallel to perpendicular position (see Sec. IV B).

only possible when using a substrate material with low heat conductance (e.g., glass) or by not depositing more than one stripe.

B. AMR based (resonant)

In contrast to the nonresonant bolometric photoresistance in Sec. IV A, the typically 50 times weaker resonant AMR-based photoresistance is very hard to detect. After visualizing it by using the CPW and turning the sample into a high symmetry position (parallel or perpendicular to **H**) it is still necessary to regard the difference of the photoresistance measured with the same current strength but with reversed current sign instead of measuring with only one current direction. This eliminates the remaining still significant photovoltage signal, which depends on the absolute current strength possibly due to bolometric AMR change.

Measurement results are presented in Fig. 14 for $f=3.8$ GHz. There it can be seen that (as deduced in Sec. II C), if the stripe lies parallel to the magnetization, the AMR is maximal and the resistance decreases when the FMR is excited (negative photoresistance). In contrast in the perpendicular case the AMR is minimal and we measure a resistance increase (positive photoresistance). This behavior is schematically explained in Fig. 15. The curves in Fig. 14 show the photoresistance at the FMR with symmetric Lorentz line shape as predicted in Sec. II C.

Using Eq. (9) we calculate $\mu_0 H_0=16.6$ mT. However, a deviation of H_0 is found in both, parallel ($\mu_0 H_0=11.1$ mT) and perpendicular ($\mu_0 H_0=25.3$ mT), configuration. This is due to demagnetization which gives rise to an FMR shift with respect to the result from the infinite film approximation [compare Eq. (31)]. $N_x=0.7\%$ can be assumed because of this shift.

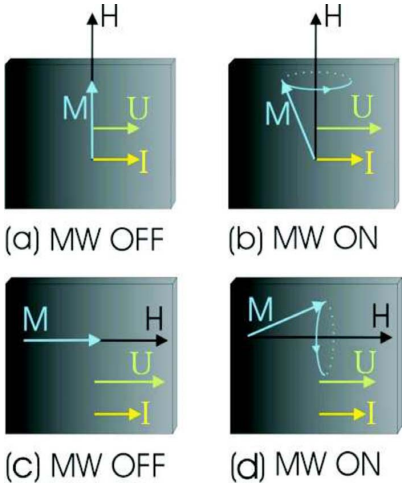

FIG. 15. (Color online) Demonstration of the angular dependence of the microwave photovoltage: Without microwaves [(a), (c)] the AMR is (a) minimal in perpendicular configuration of **M** and **I** and (c) maximal in parallel configuration. When the microwaves are switched on the resistance (b) increases in parallel configuration and (d) decreases in perpendicular configuration.

Using Eq. (16) we find that for our conditions $m_x/m_y=7.9i$. Consequently, we can neglect the contribution from $\beta_1=|m_y|/M_0$ in Eq. (17) and find $|m_x|=13$ mT using $\Delta R_{\mathrm{MW}}=(\Delta R/R)R=1.23$ mΩ (from Fig. 14) and thus $\alpha_1=\sqrt{2\Delta R_{\mathrm{MW}}/R_A}=0.73°$ and $\beta_1=\alpha_1/|m_x/m_y|=0.09°$. The smallness of β_1 is the reason for the resonant photoresistance strength being almost identical for $\mathbf{M}\parallel\mathbf{I}$ and $\mathbf{M}\perp\mathbf{I}$ (although the sign is reversed). We must expect $|m_x|$, α_1, and β_1 to be even a little bit larger due to our lock-in measurement technique only detecting the sinusoidal contribution to the square wave signal from the microwaves.

The photoresistive decrease is in accordance with that found by Costache *et al.*[13] There the magnetization is aligned with the current ($\alpha_0=0$). Thus applying an rf magnetic field decreases the AMR from R_A to $R_A\cos^2\theta_c$. This is used to determine the precession cone angle θ_c by assuming $\theta_c=\alpha_1=\beta_1$.

The height to width ratio of the strip is 35 nm to 300 nm. Because of the magnetization lying along the stripe,[13] the magnetization precession strongly deviates from being circular. Using the corresponding parameters $\mu_0 M_0=1.06$ T, $\gamma=2\pi\mu_0\times 28$ GHz/T, and $\omega/2\pi=10.5$ GHz), we find from Eq. (16) that the ratio of the amplitudes is $m_x/m_y=3.15i$. This indicates strongly elliptical precession and suggests that distinguishing α_1 and β_1 would provide a refined description compared to that using the cone angle θ_c, as discussed in Sec. II C.

V. CONCLUSIONS

We have presented a comprehensive study of dc electric effects induced by ferromagnetic resonance in Py microstrips. A theoretical model based on a phenomenological approach to magnetoresistance is developed and compared with

experiments. These provide a consistent description of both photovoltage and photoresistance effects.

We demonstrate that the microwave photoresistance is proportional to the square of magnetization precession amplitude. In the special case of circular magnetization precession, the photoresistance measures its cone angle. In the general case of arbitrary sample geometry and elliptical precession, we refine the cone angle concept by defining two different angles, which provide a precise description of the microwave photoresistance (and photovoltage) induced by elliptical magnetization precession. We show that the microwave photoresistance can be either positive or negative, depending on the direction of the dc magnetic field.

In contrast to the microwave photoresistance, we find that the microwave photovoltage is proportional to the product of the in-plane magnetization precession component with the rf current. Consequently, it is sensitive to the magnetic field dependent phase difference between the rf current and the rf magnetization. This results in a characteristic asymmetric photovoltage line shape, which crosses zero when the rf current and the in-plane component of the rf magnetization are exactly 90° out of phase. Therefore, the microwave photovoltage provides a powerful insight into the phase of magnetization precession, which is usually difficult to obtain.

We demonstrate that the asymmetric photovoltage line shape is strongly dependent on the dc magnetic field direction, which can be explained by the directional dependence of the magnetization precession excitation. By using the model developed in this work, and by combining such a sensitive geometrical dependence of the microwave photovoltage with the bolometric photoresistance which independently measures the rf current, we are now in a position to detect and determine the external rf magnetic field vector, which is of long standing interest with significant potential applications.

ACKNOWLEDGMENTS

We thank G. Roy, X. Zhou, and G. Mollard for technical assistance and D. Heitmann, U. Merkt, and the DFG for the loan of equipment. N.M. is supported by the DAAD. This work has been funded by NSERC and URGP grants to C.-M.H.

*nmecking@physnet.uni-hamburg.de
†hu@physics.umanitoba.ca

[1] B. S. Guru and H. R. Hiziroglu, *Electromagnetic Field Theory Fundamentals*, 2nd ed. (Cambridge University Press, Cambridge, UK, 2004).
[2] B. A. Gurney *et al.*, in *Ultrathin Magnetic Structures IV*, edited by B. Heinrich and J. A. C. Bland (Springer, Berlin, 2004), Chaps. 6, 7 and 8.
[3] J.-G. Zhu, and Y. Zheng, in *Spin Dynamics in Confined Magnetic Structures I*, edited by B. Hillebrands and K. Ounadjela (Springer, Berlin, 2002), pp. 289–323.
[4] A. A. Tulapurkar *et al.*, Nature (London) **438**, 339 (2005).
[5] J. C. Sankey, P. M. Braganca, A. G. F. Garcia, I. N. Krivorotov, R. A. Buhrman, and D. C. Ralph, Phys. Rev. Lett. **96**, 227601 (2006).
[6] A. Azevedo, L. H. Vilela Leo, R. L. Rodriguez-Suarez, A. B. Oliveira, and S. M. Rezende, J. Appl. Phys. **97**, 10C715 (2005).
[7] E. Saitoh, M. Ueda, H. Miyajima, and G. Tatara, Appl. Phys. Lett. **88**, 182509 (2006).
[8] M. V. Costache, M. Sladkov, S. M. Watts, C. H. van der Wal, and B. J. van Wees, Phys. Rev. Lett. **97**, 216603 (2006); J. Grollier, M. V. Costache, C. H. van der Wal, and B. J. van Wees, J. Appl. Phys. **100**, 024316 (2006).
[9] Y. S. Gui, S. Holland, N. Mecking, and C.-M. Hu, Phys. Rev. Lett. **95**, 056807 (2005).
[10] Y. S. Gui, N. Mecking, X. Zhou, Gwyn Williams, and C.-M. Hu, Phys. Rev. Lett. **98**, 107602 (2007).
[11] Y. S. Gui, N. Mecking, and C.-M. Hu, Phys. Rev. Lett. **98**, 217603 (2007).
[12] Y. S. Gui, N. Mecking, A. Wirthmann, L. H. Bai, and C.-M. Hu, Appl. Phys. Lett. **91**, 082503 (2007).
[13] M. V. Costache, S. M. Watts, M. Sladkov, C. H. van der Wal, and B. J. van Wees, Appl. Phys. Lett. **89**, 232115 (2006).
[14] A. Yamaguchi, H. Miyajima, T. Ono, Y. Suzuki, S. Yuasa, A. Tulapurkar, and Y. Nakatani, Appl. Phys. Lett. **90**, 182507 (2007); A. Yamaguchi, H. Miyajima, T. Ono, Y. Suzuki, S. Yuasa, A. Tulapurkar, and Y. Nakatani, *ibid.* **90**, 212505 (2007).
[15] Dong Keun Oh *et al.*, J. Magn. Magn. Mater. **293**, 880 (2005); Je-Hyoung Lee and Kungwon Rhie, IEEE Trans. Magn. **35**, 3784 (1999).
[16] S. T. Goennenwein, S. W. Schink, A. Brandlmaier, A. Boger, M. Opel, R. Gross, R. S. Keizer, T. M. Klapwijk, A. Gupta, H. Huebl, C. Bihler, and M. S. Brandt, Appl. Phys. Lett. **90**, 162507 (2007).
[17] J. C. Slonczewski, J. Magn. Magn. Mater. **159**, L1 (1996).
[18] L. Berger, Phys. Rev. B **54**, 9353 (1996).
[19] L. Berger, Phys. Rev. B **59**, 11465 (1999).
[20] A. Brataas, Yaroslav Tserkovnyak, Gerrit E. W. Bauer, and Bertrand I. Halperin, Phys. Rev. B **66**, 060404(R) (2002).
[21] Xuhui Wang, Gerrit E. W. Bauer, Bart J. van Wees, Arne Brataas, and Yaroslav Tserkovnyak, Phys. Rev. Lett. **97**, 216602 (2006).
[22] C.-M. Hu, C. Zehnder, Ch. Heyn, and D. Heitmann, Phys. Rev. B **67**, 201302(R) (2003).
[23] H. J. Juretschke, J. Appl. Phys. **31**, 1401 (1960).
[24] R. H. Silsbee, A. Janossy, and P. Monod, Phys. Rev. B **19**, 4382 (1979).
[25] W. M. Moller and H. J. Juretschke, Phys. Rev. B **2**, 2651 (1970).
[26] D. Polder, Philos. Mag. **40**, 99 (1949).
[27] T. L. Gilbert, IEEE Trans. Magn. **40**, 3443 (2004).
[28] L. Landau and L. Liftshitz, Phys. Z. Sowjetunion **8**, 153 (1935).
[29] R. E. Camley and D. L. Mills, J. Appl. Phys. **82**, 3058 (1997).
[30] C. Kittel, Phys. Rev. **73**, 155 (1948).
[31] W. G. Egan and H. J. Juretschke, J. Appl. Phys. **34**, 1477 (1963).
[32] J. N. Kupferschmidt, Shaffique Adam, and P. W. Brouwer, Phys. Rev. B **74**, 134416 (2006).
[33] S. I. Kiselev, J. C. Sankey, I. N. Krivorotov, N. C. Emley, R. J. Schoelkopf, R. A. Buhrman, and D. C. Ralph, Nature (London) **425**, 380 (2003).
[34] M. S. Sodha and N. C. Srivasta, *Microwave Propagation in Ferrimagnets* (Plenum Press, New York, 1981).
[35] K. L. Yau and J. T. H. Chang, J. Phys. F: Met. Phys. **1**, 38 (1971).

5.2 Supplementary Details

In this section we present further details on the derivation of the results in publication P1. In section 5.2.1 to 5.2.3 the derivation of some specially complex theoretical results of publication P1 is presented in more details. Further in section 5.2.4 the measurement results which lead to the determination of the rf magnetic field configuration at our samples position in figure 13 of publication P1 are supplemented.

5.2.1 Second Order Approximation of the Dependence of the AMR on the Magnetization Precession's Maximal Horizontal and Vertical Deflection Angles

Using equation (2) in publication P1 we approximate the dependence of the AMR on the dynamic angle $\theta(t)$ between the magnetization and current axis, namely $\cos^2\theta(t)$, to second order in the maximum deflection angles α_1^t and β_1^t, (in-plane and out-of-plane, respectively). Note that: $\alpha(t) = \alpha_0 + \alpha_1^t(t) = \alpha_0 + \alpha_1\cos(\omega t - \psi)$ and $\beta(t) = \beta_1^t(t) = -\beta_1\sin(\omega t - \psi)$.

$$\begin{aligned}\cos^2\theta(t) \approx \cos^2\theta|_{\alpha_1^t=\beta_1^t=0} + \alpha_1^t\cdot\frac{d\cos^2\theta}{d\alpha_1^t}|_{\alpha_1^t=\beta_1^t=0} + \beta_1^t\cdot\frac{d\cos^2\theta}{d\beta_1^t}|_{\alpha_1^t=\beta_1^t=0}\\ +\frac{\alpha_1^{t2}}{2}\cdot\frac{d^2\cos^2\theta}{d\alpha_1^{t2}}|_{\alpha_1^t=\beta_1^t=0} + \frac{\beta_1^{t2}}{2}\cdot\frac{d^2\cos^2\theta}{d\beta_1^{t2}}|_{\alpha_1^t=\beta_1^t=0}\\ = \cos^2\theta|_{\alpha_1=\beta_1=0} + \alpha_1^t\cdot\frac{d\cos^2\theta}{d\alpha}|_{\alpha_1=\beta_1=0} + \beta_1^t\cdot\frac{d\cos^2\theta}{d\beta}|_{\alpha_1=\beta_1=0}\\ +\frac{\alpha_1^{t2}}{2}\cdot\frac{d^2\cos^2\theta}{d\alpha^2}|_{\alpha_1=\beta_1=0} + \frac{\beta_1^{t2}}{2}\cdot\frac{d^2\cos^2\theta}{d\beta^2}|_{\alpha^t=\beta^t=0}\end{aligned}$$

with (compare equation (2) in publication P1):

$$\begin{aligned}\frac{d\cos^2\theta}{d\alpha}|_{\alpha_1=\beta_1=0} &= -\sin 2\alpha\cos^2\beta|_{\alpha_1=\beta_1=0} = -\sin 2\alpha_0\\ \frac{d\cos^2\theta}{d\beta}|_{\alpha_1=\beta_1=0} &= -\cos^2\alpha\sin 2\beta|_{\alpha_1=\beta_1=0} = 0\\ \frac{d^2\cos^2\theta}{d\alpha^2}|_{\alpha_1=\beta_1=0} &= -2\cos 2\alpha\cos^2\beta|_{\alpha_1=\beta_1=0} - 2\cos 2\alpha_0\\ \frac{d^2\cos^2\theta}{d\beta^2}|_{\alpha_1=\beta_1=0} &= -2\cos^2\alpha\cos 2\beta|_{\alpha_1=\beta_1=0} - 2\cos^2\alpha_0\end{aligned}$$

Conclusively:

$$\cos^2\theta(t) \approx \cos^2\alpha_0 - \alpha_1 \cdot \sin 2\alpha_0 \cos(\omega t - \psi)$$
$$-\alpha_1^2 \cdot \cos 2\alpha_0 \cos^2(\omega t - \psi) - \beta_1^2 \cdot \cos^2\alpha_0 \sin^2(\omega t - \psi)$$

This is equation (4) in publication P1.

5.2.2 Determination of the Magnetic Field Dependence of the Magnetization Precession's Maximal Horizontal and Vertical Deflection Angles

From equation (14) in publication P1 follows (note that: $A_{xx} \cdot A_{yy} \approx A_{xy}$):

$$|A_{xx}h_x + iA_{xy}h_y|^2 = A_{xx} \cdot |\sqrt{A_{xx}}h_x + i\sqrt{A_{xy}}h_y|^2 =$$
$$\frac{A_{xx}}{A_{xy}}A_{yy} \cdot |-i\sqrt{A_{xx}}h_x + \sqrt{A_{xy}}h_y|^2 = \frac{A_{xx}}{A_{xy}} \cdot |-iA_{xy}h_x + A_{yy}h_y|^2$$

Considering equation (8) and (12) in publication P1 it can be deduced that:

$$|m_x|^2 = \frac{A_{xx}}{A_{xy}}|m_y|^2$$

and it follows that:

$$\alpha_1^2 = \frac{|m_x|^2}{M_0^2} = \frac{\gamma^2(H_0 + M_0)}{\alpha_G^2\omega^2(2H_0 + M_0)^2} \cdot |h_x\sqrt{H_0 + M_0} + ih_y\sqrt{M_0}|^2 \cdot \frac{\Delta H^2}{(H - H_0)^2 + \Delta H^2}$$
$$\beta_1^2 = \frac{|m_y|^2}{M_0^2} = \frac{\gamma}{\alpha_G^2\omega(2H_0 + M_0)^2} \cdot |h_x\sqrt{H_0 + M_0} + ih_y\sqrt{M_0}|^2 \cdot \frac{\Delta H^2}{(H - H_0)^2 + \Delta H^2}$$

Putting this into equation (17) from publication P1 then results in equation (19) in publication P1.

5.2.3 Determination of the In-Phase Contribution to the In-Plane Component of the rf Magnetization with Respect to the rf Current Phase

From equation (12) in publication P1 it can be followed that:

$$\alpha_1 M_0 \cos\psi = \Re(m_x) = \Re(\chi_{xx} h_x + i\chi_{xy} h_y)$$
$$= (A_{xx} h_x^r - A_{xy} h_y^i)\frac{(H-H)\Delta H}{(H-H_0)^2+\Delta H^2} - (A_{xx} h_x^i + A_{xy} h_y^i)\frac{\Delta H^2}{(H-H_0)^2+\Delta H^2}$$

Putting this into equation (21) in publication P1 gives equation (23) in P1.

5.2.4 Supplementary Measurement Results

In this subsection we present microwave photovoltage measurement results concerning the stripes B and C of the stripe array whose mask is presented in figure 3.1. These two stripes were used to determine the microwave magnetic field distribution in figure 13 of publication P1. However for reasons of limited space in publication P1 figure 8 and 10 and table I only display data for stripe A (see figure 3.1). As figure 13 in publication P1 is based on these data but also on the corresponding data for the stripes B and C of the array (see figure 3.1) which are omitted in P1. These data are hence presented here using for the same microwave frequency $f = 15$ GHz and the same microwave generator output power $P = 200$ mW. Thereby figure 5.2 and 5.4 correspond to figure 8 in publication P1, figure 5.3 and 5.5 to figure 10 and table 5.1 in P1 and 5.2 to table I in P1. It can be seen that the fittings of the photovoltage of stripe B and C match in a similar adequate fashion as do those for stripe A in publication P1.

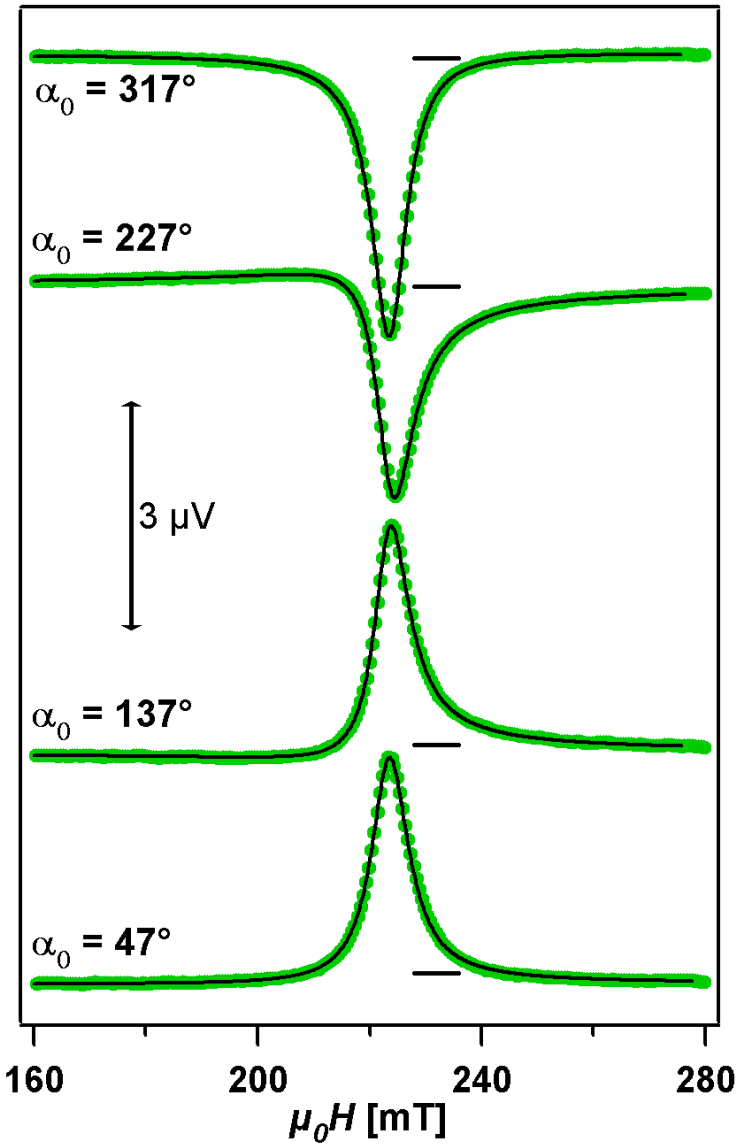

Figure 5.2: Fitting (black line) of the microwave photovoltage signal (dots) of stripe B (see figure 3.1) of the sample from publication P1. The microwave photovoltage is displayed for different angles α_0 between the magnetization and stripe axis at $f = 15$ GHz. For the fittings equation (32) from publication P1 was used. The curves are offset for clarity and the black horizontal bars indicate the corresponding zero signal lines.

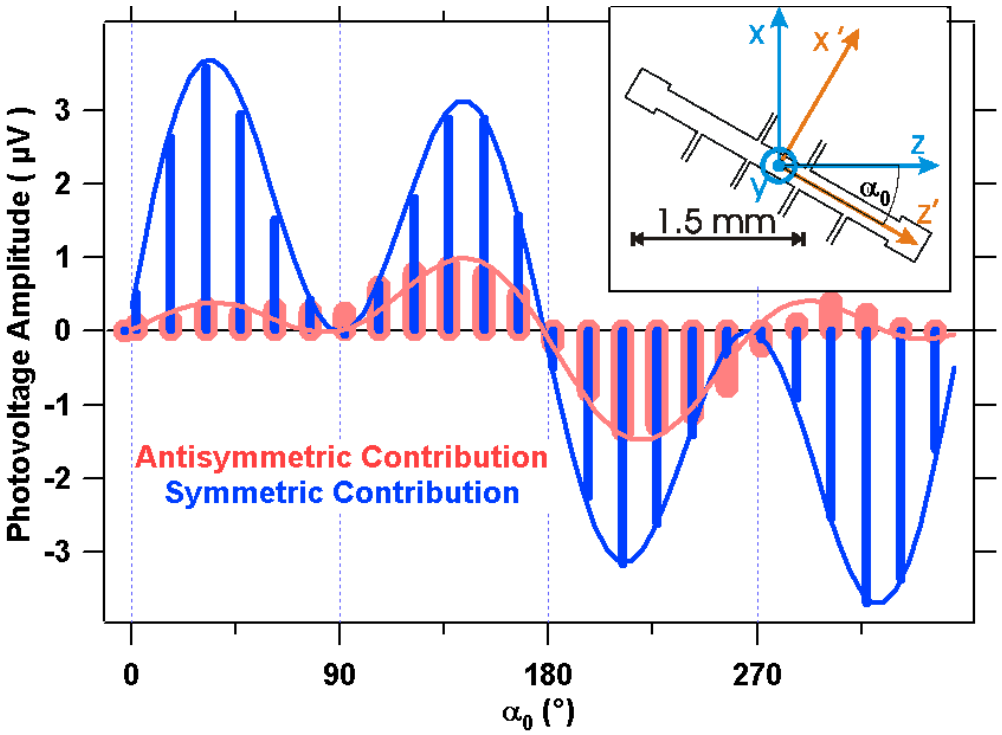

Figure 5.3: The bars show the angular dependence of the amplitude of the symmetric (U_0^{ABS}, thin bars) and antisymmetric (U_0^{DISP}, thick bars) contribution to the microwave photovoltage of stripe B (see figure 3.1) of the film stripe from publication P1 at f = 15 GHz. Note that both, the symmetric and antisymmetric contribution, vanish for $\alpha_0 = 0°, 90°, 180°$ and 270°. The lines show the corresponding fits by means of equation (34) of publication P1. The inlet displays the magnetic field's angle α_0 with respect to the 200 μm wide Permalloy stripe (A) and the coordinate system (note: $\mathbf{z} \parallel \mathbf{H}$).

	$U^S_{x\prime,y,z\prime}$	$U^A_{x\prime,y,z\prime}$	A_{xx} A_{xy}	$I_1 \cdot h^r_{x\prime,y,z\prime}$	$I_1 \cdot h^i_{x\prime,y,z\prime}$
	(μV)			($\mathrm{mA}\cdot\mu\mathrm{T}/\mu_0$)	
x'	+0.90	+4.45	231.1	26.9	-5.4
y	+0.30	-0.55	97.1	4.4	-8.1
z'	+0.40	0.00	231.1	0.0	-2.3

Table 5.1: Determination of the rf magnetic field **h** at the position of stripe B (see figure 3.1) of the sample from publication P1 at - like in figure 5.2 and 5.3 - 1 mm distance from the waveguide end. For this equation (34) from publication P1 was used. $U^S_{x\prime,y,z\prime}$, $U^A_{x\prime,y,z\prime}$: Measured amplitudes of the contributions with symmetric and antisymmetric Lorentz line shape to U_{MW}. The different contributions have different angle dependencies ($\sin\alpha_0$, 1, $\cos\alpha_0$). They are determined using the fitting in figure 5.3 by means of equation (34) in publication P1. Following equation (33) and (34) in publication P1 $U^S_{x\prime,y,z\prime}$ and $U^A_{x\prime,y,z\prime}$ are proportional to ($h^i_{x\prime}$, h^r_y, $h^i_{z\prime}$) and ($h^r_{x\prime}$, h^i_y, $h^r_{z\prime}$) respectively. $A_{xx,xy}$: Amplitudes of $\chi_{xx,xy}$ (see equation (12) in P1). $h^r_{x\prime,y,z\prime}$, $h^i_{x\prime,y,z\prime}$: rf magnetic field strength calculated from $U^S_{x\prime,y,z\prime}$, $U^A_{x\prime,y,z\prime}$. $h^r_{x\prime,y,z\prime}$ is the contribution in-phase and $h^i_{x\prime,y,z\prime}$ that 90° out-of-phase with respect to the rf current.

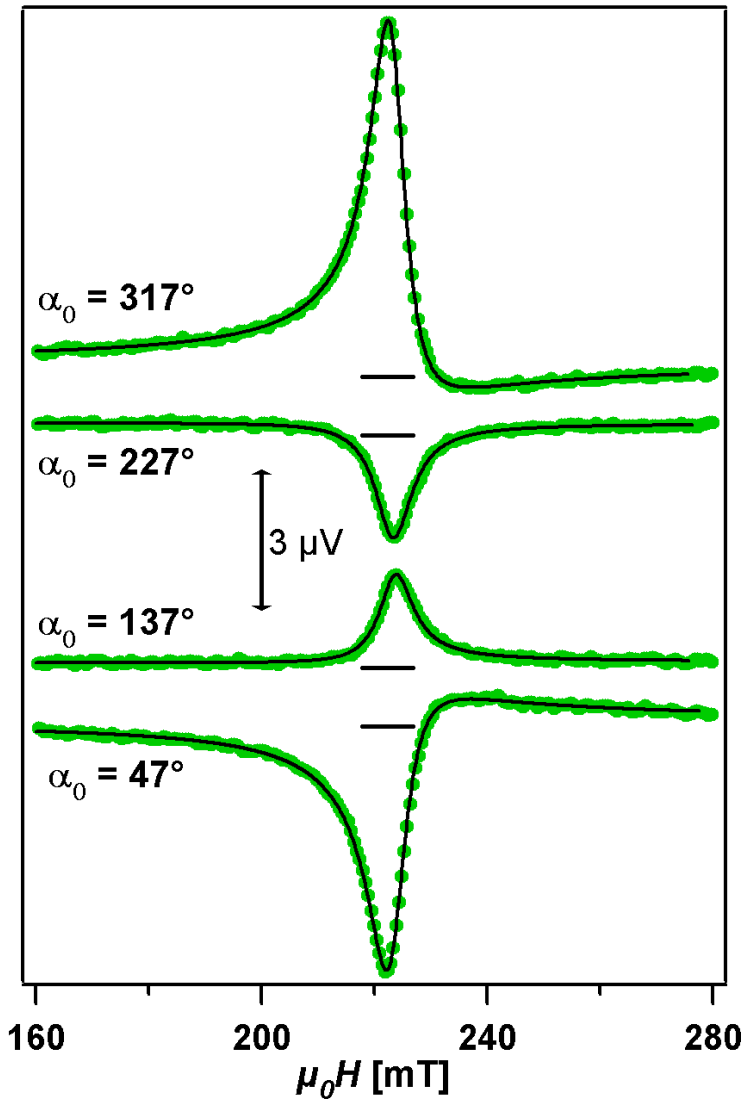

Figure 5.4: Fitting (black line) of the microwave photovoltage signal (dots) of stripe C (see figure 3.1) of the sample from publication P1. The photovoltage is displayed for different angles α_0 between the magnetization and the stripe axis at $f = 15$ GHz. For the fitting equation (32) in publication P1 was used. The curves are offset for clarity and the black horizontal bars indicate the corresponding zero signal lines. The stronger noise compared to the measurements on the other stripes (see figure 8 in publication P1 and figure 5.2 in this work) is caused by the use of one amplifier stage less for the microwave photovoltage detection on this stripe.

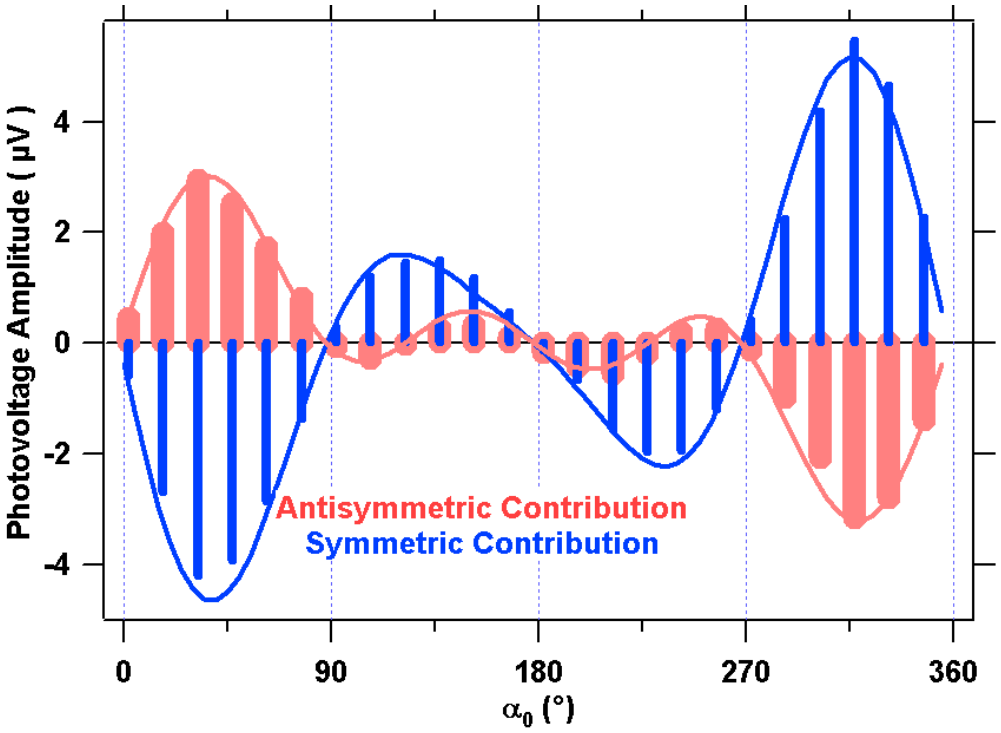

Figure 5.5: The bars show the angular dependence of the amplitude of the symmetric (U_0^{ABS}, thin bars) and antisymmetric (U_0^{DISP}, thick bars) contribution to the microwave photovoltage of stripe C (see figure 3.1) of the sample from publication P1 at f = 15.0 GHz. Note that both, the symmetric and antisymmetric contribution, vanish for $\alpha_0 = 0°, 90°, 180°$ and 270°. The lines show the corresponding fits by means of equation (34) of publication P1.

	$U^S_{x\prime,y,z\prime}$	$U^A_{x\prime,y,z\prime}$	A_{xx} A_{xy}	$I_1 \cdot h^r_{x\prime,y,z\prime}$	$I_1 \cdot h^i_{x\prime,y,z\prime}$
	(μV)			(mA·μT/μ_0)	
x'	+2.30	-2.20	231.1	13.5	14.2
y	-3.30	+1.40	97.1	-48.6	20.5
z'	-0.15	+0.40	231.1	2.3	0.9

Table 5.2: Determination of the rf magnetic field **h** at the position of stripe C (see figure 3.1) of the sample from publication P1 at - like in figure 5.4 and 5.5 - 1 mm distance from the waveguide end. For this equation (34) from publication P1 was used. $U^S_{x\prime,y,z\prime}$, $U^A_{x\prime,y,z\prime}$: Measured amplitudes of the contributions with symmetric and antisymmetric Lorentz line shape to U_{MW}. The different contributions have different angle dependencies ($\sin\alpha_0$, 1, $\cos\alpha_0$). They are determined using the fitting in figure 5.5 by means of equation (34) in publication P1. Following equation (33) and (34) in publication P1 $U^S_{x\prime,y,z\prime}$ and $U^A_{x\prime,y,z\prime}$ are proportional to ($h^i_{x\prime}$, h^r_y, $h^i_{z\prime}$) and ($h^r_{x\prime}$, h^i_y, $h^r_{z\prime}$) respectively. $A_{xx,xy}$: Amplitudes of $\chi_{xx,xy}$ (see equation (12) in P1). $h^r_{x\prime,y,z\prime}$, $h^i_{x\prime,y,z\prime}$: rf magnetic field strength calculated from $U^S_{x\prime,y,z\prime}$, $U^A_{x\prime,y,z\prime}$. $h^r_{x\prime,y,z\prime}$ is the contribution in-phase and $h^i_{x\prime,y,z\prime}$ that 90° out-of-phase with respect to the rf current.

5.3 Standing Spin Waves Perpendicular to In-Plane Magnetized Ferromagnetic Films

Standing spin wave modes perpendicular to ferromagnetic films have already been observed in figure 5.1 where a hollow waveguide was used for the microwave transmission. However, to visualize more than one perpendicular standing spin wave order a thicker film stripe is needed because there the spin wave frequency is closer to that of the FMR (see equation (2.16) and (2.17)) and therefore rather below the maximal frequency of our microwave equipment.

Instead of the $d = 49$ nm thick film stripe used for the data in figure 5.1 we hence use a $d = 108$ nm thick film stripe with the width $W = 20$ μm and length $L = 2.45$ mm. This stripe is also improved in being imbedded in a CPW (see section 3) which enables measurements at specially low microwave frequencies and at higher microwave powers. A microscope photo of a similar structure can be seen in figure 3.2. In figure 5.6 a fit of the first standing spin wave mode with equation (2.17) is displayed together with a gray scale plot of the photovoltage. For the microwave transmission the CPW is used because it results in a much stronger photovoltage compared to the irradiation of the sample with a hollow waveguide.

From the fitting $H_S = H_{S1} = 46$ mT is found for the first standing spin wave mode (see figure 5.6). In principle this can be used to estimate the strength A of the exchange interaction by means of equation (2.16) considering the spin wave's perpendicular confinement $d = 108$ nm. However in this case the order n of the standing spin wave has to be known which can also take non-integer values (see section 2.6.1 and publication P3). Further information about the order can be obtained by visualizing additional spin wave modes. This is possible when going to even higher microwave frequencies, where a second spin wave resonance appears as can be seen in figure 5.7. There the spacing between the FMR and the two spin wave modes is $H_{S1} = 46$ mT for the first spin wave resonance like found above and $H_{S2} = 190$ mT for the second spin wave resonance. Hence we interpret the two modes as first ($n = 1$) and second ($n = 2$) order, because for exchange dominated spin waves the magnetic field difference to the FMR increases quadratically with the wave vector k (see equation (2.16)). Thus we get an exchange interaction strength of $A = 2.1 \cdot 10^{-11}$ N by means of equation (2.16). This is roughly in accordance with the value found in publication P3.

It has to be admitted that the pinning condition at the surface of our Permalloy film is still only roughly known at this stage and that possible decimal places of n are elided. Therefore the assumption of $n = 1$ and

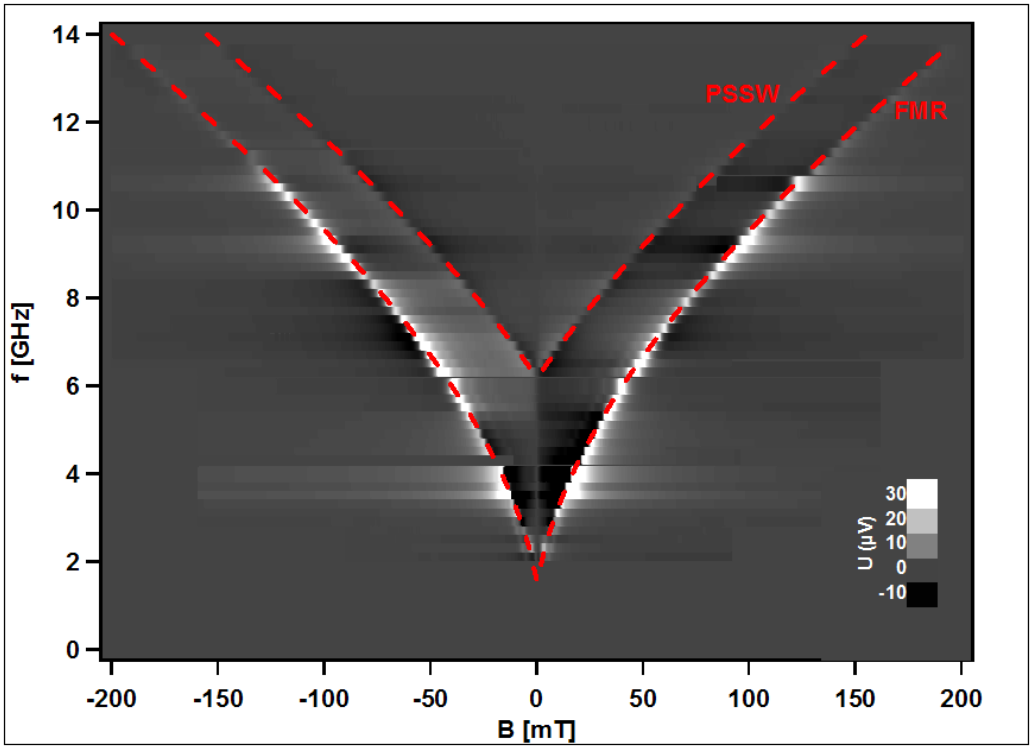

Figure 5.6: Grayscale plot of the microwave photovoltage in a 108 nm thick film stripe irradiated with a CPW at $P = 200$ mW generator output power. Fits of the FMR (lower dashed line) and the first PSSW (upper dashed line) are displayed. For the fittings equation (2.10) and (2.17) and the following parameters were used: $M_0 = 1$ T, $\gamma/2\pi = 28.4$ GHz/T and $H_S = 46$ mT. A good agreement with the grayscale plot is visible. As seen above, a special feature of the FMR is that its frequency does not go to zero if the magnetic field is switched off. We assign this effect to the impact of demagnetization effects on the FMR frequency which have been discussed in publication P1 by referring to the general Kittel equation for ellipsoids (see equation (31) in publication P1). This effect was also considered in the fittings.

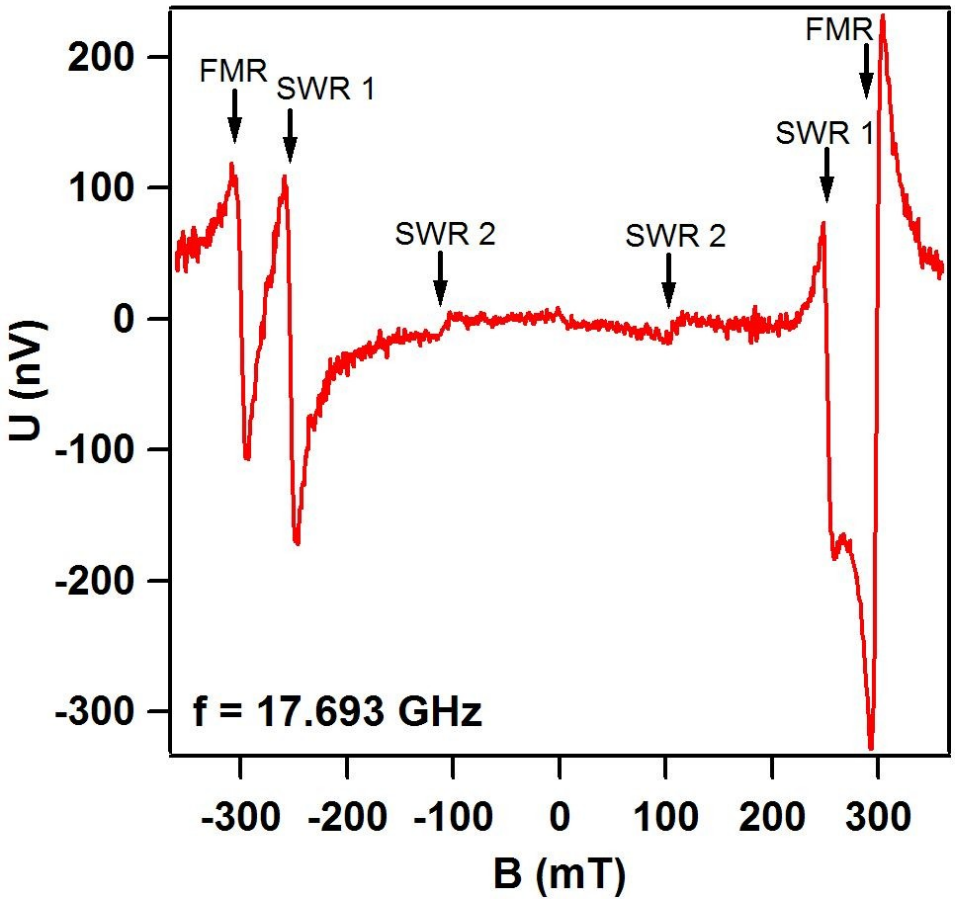

Figure 5.7: Microwave photovoltage measurement with the angle $\alpha_0 = 45°$ between the magnetization and the film stripe which was irradiated by a hollow K_U-band waveguide. The microwave generator output power is $P =$ 200 mW. Beside the FMR two spin waves (SWR1 and SWR2) are visible which appear for both, positive and negative magnetic fields and exhibit like discussed for the FMR in section III C of publication P1 an asymmetric line shape. The magnetic field spacing of the 2 spin wave modes from the FMR is 46 mT and 190 mT respectively. For exchange dominated spin wave modes the magnetic field difference compared to the FMR increases quadratically with the wave vector k and hence with the mode order n (see equation (2.16)). Thus we interpret the spin wave resonances as first and second order standing spin waves perpendicular to our ferromagnetic film. Additionally like in figure 5.1 at $B = 0$ again a small step in the photovoltage is visible. The strong decreasing of the signal strength with increasing mode order is accordance with previous results [7].

$n = 2$ respectively for the two spin wave modes just gives us an approximate value for A. To find a more precise value the pinning condition has to be known more precisely and for this the observation of even more spin wave modes would be necessary, but this is not possible in the case of an in-plane magnetized ferromagnetic film because of the limited frequency range (≤ 20 GHz) of the microwave generator. However, for the case of perpendicular magnetized ferromagnetic films the frequency of the FMR and the PSSWs is lower (see equation (2.20)) and more than two spin waves can be displayed. This can be used to determine A more precisely and also to draw further conclusions concerning the pinning condition as done in publication P3 (see section 6.2.1).

It has to be noted that for the measurement in figure 5.7 a rectangular hollow waveguide was used to transmit the microwaves because the CPW only transmits very little at such high frequencies ($f = 17.693$ GHz). The line shape of the PSSW photovoltage is found to be asymmetric like that of the FMR (see figure 8 in publication P1) with which it superposes (see figure 5.7) and also a similar angle dependence with vanishing of the PSSWs at $\alpha_0 = 0°$, $\alpha_0 = \pm 90°$ and $\alpha_0 = 180°$ is found. Therefore it can be assumed that the PSSW-induced microwave photovoltage arises from the AMR-based spin rectification like the FMR-induced photovoltage (see publication P1). This seems also likely when the fact is considered that like the FMR also spin waves are nothing but - in this case inhomogeneous - spin precession. It would be an interesting task to generalize the theoretical model of publication P1 to spin wave resonances wherefore the assumption of a spatially inhomogeneous magnetization would be necessary. We will continue by discussing a different kind of spin precession modes, namely the Damon-Eshbach modes.

5.4 Damon-Eshbach Modes

For the investigation of Damon-Eshbach modes the same Permalloy film stripe (thickness $d = 108$ nm and width $W = 20$ μm) is used that was also used for the experiments on the PSSWs in the previous section 5.3. Damon-Eshbach modes were already observed in the photovoltage measurement results presented in figure 5.6. However, there they are not visualized because their signal is about two orders of magnitude weaker than that from the FMR and the first PSSW. They become observeable in figure 5.8 where only the microwave photovoltage signal for one frequency is plotted. There, two Damon-Eshbach mode resonances are visible with about 1 μV amplitude. This is still significantly above the noise level (≈ 5 nV). The full width at half maximum (FWHM) is about 3 mT. This is roughly the same FWHM as found for the FMR (note that the width of the FMR and Damon-Eshbach modes look very different at first guess in figure 5.8, but this is only an illusion due to the very different signal strength).

An overview of the whole microwave frequency dependence of the Damon-Eshbach modes can be found in figure 5.9 where up to four orders are found in total. At low microwave frequencies however, when their resonance magnetic field decreases down to the order of their FWHM, the modes disappear. For the lowest order mode this happens at $f \approx 4$ GHz. At high microwave frequencies the transmission of the CPW decreases and the Damon-Eshbach modes become invisible, too, above about $f = 11$ GHz due to the resulting lower sensitivity.

Damon-Eshbach modes are the magnetostatic modes which appear in the case that their wave vector $\mathbf{k}_\parallel$ lies perpendicular to the magnetization. We investigate Damon-Eshbach modes confined perpendicular to our film stripe (width $W = 20$ μm) because along our film stripe (length $L \approx 2$ mm) the confinement is too weak to define standing waves with a magnetic field H spacing sufficiently large for the resolution of the individual modes and for a sufficient separation from the FMR (compare 5.10). Consequently our stripe has to be aligned to the static magnetic field (and thus to the magnetization). In this symmetry case, however the microwave photovoltage vanishes because, for its appearing the stripe has to be categorically misaligned with respect to the magnetic field (compare figure 10 and 11 in publication P1). The maximum of the photovoltage signal appears at an angle of about $\alpha_0 = 45°$ between the magnetization $\mathbf{M}$ and stripe direction (see equation (21) in publication P1). Therefore as a compromise we measure the signal at $\alpha_0 = 37.5°$. Note that a discussion on how the angle between $\mathbf{k}_\parallel$ and $\mathbf{M}$ impacts the Damon-Eshbach mode resonances can be found in the work of Damon and Eshbach [42]. For our case we will go into more detail with the angle dependence at the end of

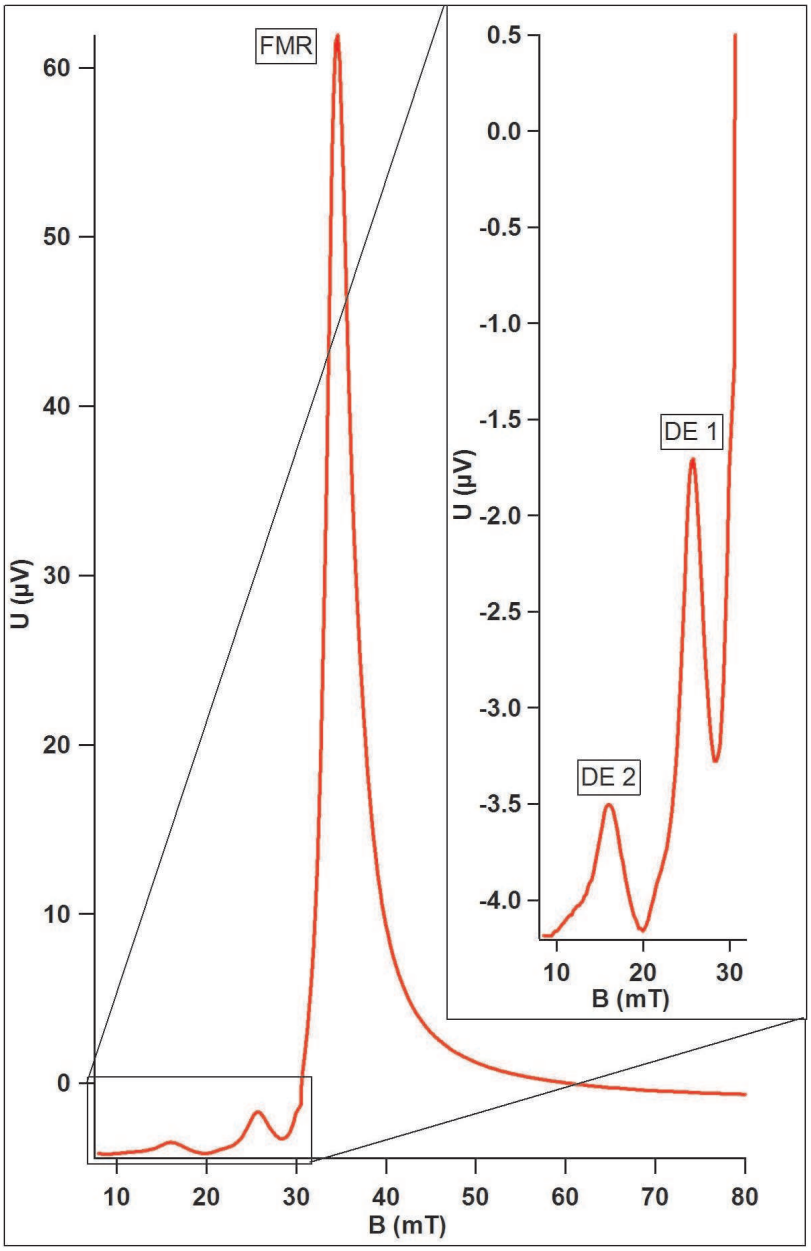

Figure 5.8: Measurement of the magnetic field dependence of the microwave photovoltage in a 108 nm thick film stripe at $f = 5.6$ GHz and $\alpha_0 = 37.5°$. The microwave generator output power is $P = 200$ mW. Two Damon-Eshbach modes DE1 and DE2 are observed and it can be seen that they are about 50 and 100 times smaller than the FMR. The inlet expands the magnetic field range between 10 and 30 mT in which DE1 and DE2 are found. A CPW is used to transmit the microwaves onto the film stripe.

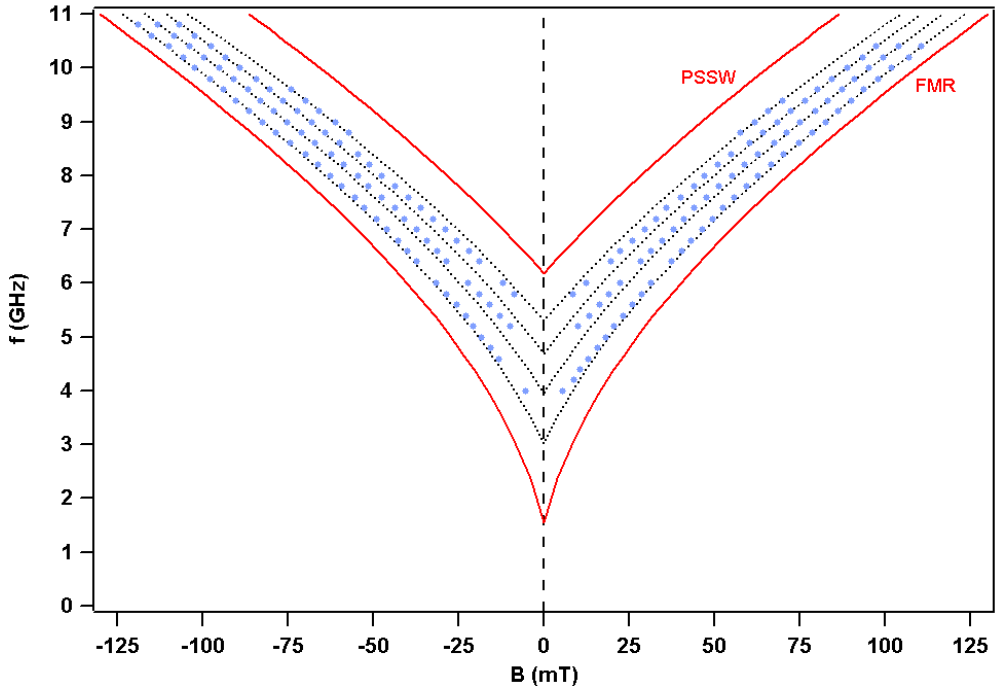

Figure 5.9: Plot of the measured magnetic field dependence of the resonance frequencies of the confined Damon-Eshbach modes (dots) in a 108 nm thick film stripe for $\alpha_0 = 37.5°$ and a microwave generator output power $P = 200$ mW. The dotted lines show the Damon-Eshbach mode frequencies calculated by means of equation 2.24. Additionally for better orientation also the fits of the FMR and PSSW (solid lines) from figure 5.6 are displayed.

this section.

The next question is in how far the measured magnetic field dependence corresponds to the theoretical predictions presented in section 2.8.1. Therefore equation (2.24) was used to calculate the Damon-Eshbach frequency considering the ferromagnetic film parameters determined in section 5.3. The resulting magnetic field dependence is also plotted in figure 5.9 and compared to the measurement results. For high magnetic fields $H > 50$ mT an agreement of the calculations with the experimental results is found. At low magnetic fields, however, the measured Damon-Eshbach mode frequencies are higher than the calculated ones. A possible reason could be the impact of demagnetization or that from $k_{\parallel}$ lying perpendicular to the magnetic field. For figure 5.9 the demagnetization was respected in the calculations based on equation (2.24) by replacing the contribution $H(H + M_0)$ associated with the FMR frequency for an in-plane magnetized plane (see equation 2.9) by

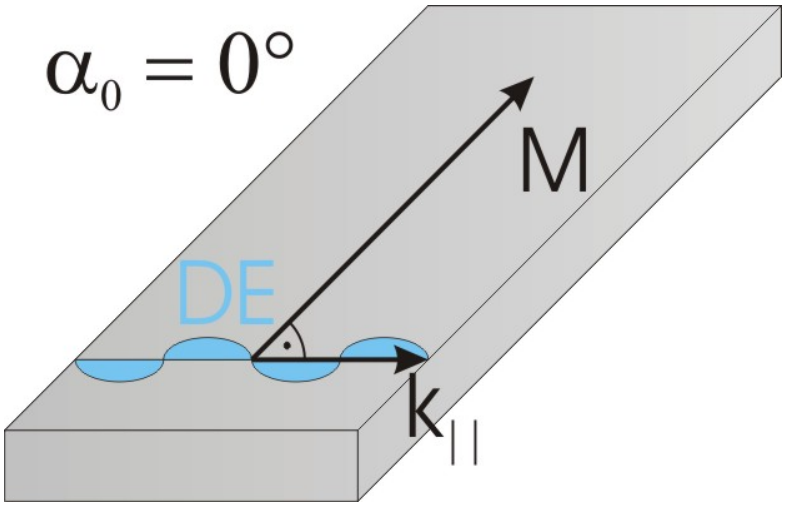

Figure 5.10: Geometry in which the Damon-Eshbach modes (DE) are investigated: The magnetization (**M**) lies parallel to our film stripe and the Damon-Eshbach modes (wave vector $\mathbf{k}_{\parallel}$) are confined perpendicular to it. The displayed case represents the standard configuration for Damon-Eshbach modes ($\mathbf{k}_{\parallel} \perp \mathbf{M}$), however in this case no microwave photovoltage is generate. For this **M** has to be - at least slightly - misaligned with respect to the stripe.

$(H_0 + (N_x - N_z) \cdot M_0) \cdot (H_0 + (N_y - N_z) \cdot M_0)$. This is associated with the equation for an ellipsoid (see equation (31) in publication P1).

We will now continue with discussing the dependence of the Damon-Eshbach modes' resonance magnetic field on the angle α_0 between the stripe and the magnetization **M**. An overview of the corresponding measurement configuration is provided in figure 5.10 and the measurement results can be found in figure 5.11. It becomes visible that the Damon-Eshbach mode resonance magnetic field approaches that of the FMR and finally completely vanishes when $\alpha_0 = \pm 90°$ is approached. The reason is that there one leaves the Damon-Eshbach mode regime and gradually enters that of the Backward-Volume modes which are, however, not observed here probably due to a smaller magnetic field difference with respect to the FMR. According to equation (2.25) it should be expected that the Damon-Eshbach modes vanish at $\alpha_0 > 90° - \Theta_{DE} = 78.3°$ and $\alpha_0 < 90° + \Theta_{DE} = 101.7°$. However already at $\alpha_0 = 67.5°$ and $\alpha_0 = 112.5°$ (and also at $\alpha_0 = 247.5°$ and $\alpha_0 = 292.5°$) no Damon-Eshbach modes are observed anymore (see figure 5.11). This might be caused by the decreasing magnetic field spacing between the modes when going further away from $\alpha_0 = 0°$ and $\alpha_0 = 180°$ what renders the individual

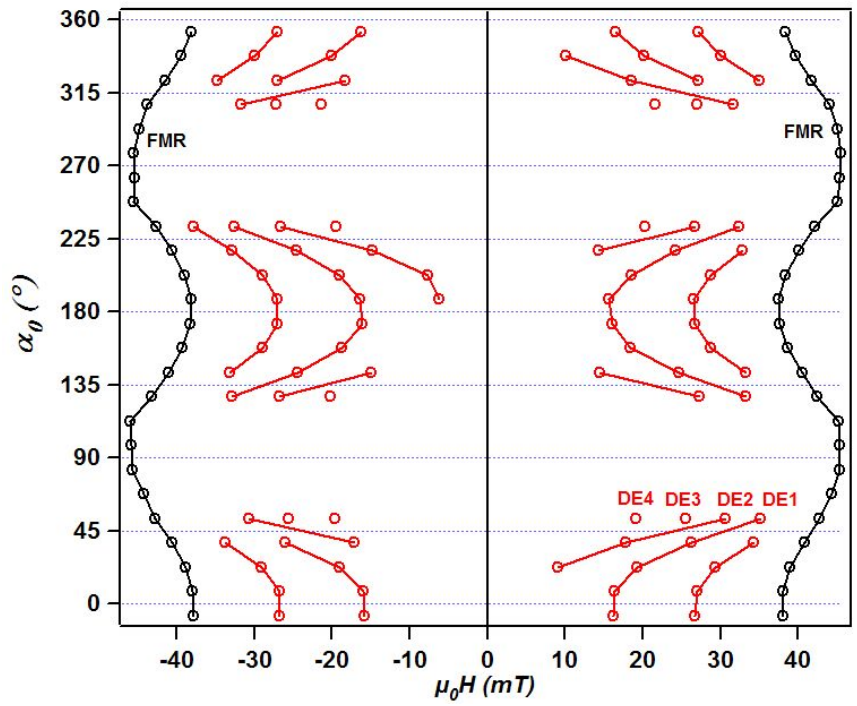

Figure 5.11: Angle dependence of the resonance magnetic field of the Damon-Eshbach modes (red circles) at the microwave frequency $f = 6$ GHz with the microwave generator output power $P = 200$ mW in a $d = 108$ nm thick Permalloy film stripe. The black circles display the corresponding FMR frequency. This is angle dependent because of the varying demagnetization conditions to which the sample is subject when being rotated (compare equation (31) in publication P1).

observation of the Damon-Eshbach modes impossible.

The decreasing Damon-Eshbach mode spacing when α_0 approaches $\pm 90°$ is also responsible for an other important conclusion from figure 5.11, namely that also the frequency dependence which was presented in figure 5.9 for $\alpha_0 = 37.5°$ is expected to be different from that calculated by means of equation (2.24) which is valid for $\alpha_0 = 0°$. Conclusively there is an obvious reason for discrepancies between the measurement data and calculations in figure 5.9. However, in this section, especially in figure 5.9 and 5.11, it becomes visible that the basis for a detailed discussion of the interplay of the Damon-Eshbach modes' angle dependence with their frequency dependence by means of the microwave photovoltage is established and that this might result in many new results. Thus a detailed discussion of the frequency dependence of the Damon-Eshbach mode-induced microwave photovoltage is

to follow and thereby it has to be noted that in the following section 6 such a detailed discussion is already established for the case of the corresponding magnetostatic modes in out-of-plane configuration, namely for the Forward-Volume modes.

Chapter 6

Normally Magnetized Ferromagnetic Films

After discussing the microwave photovoltage and photoresistance in in-plane magnetized ferromagnetic films in section 5 we will now continue with presenting measurements concerning the microwave photovoltage in normally magnetized ferromagnetic films whereby we also use the possibility to investigate photocurrent instead of photovoltage. Note that a short introduction on how to find photocurrent instead of photovoltage was provided at the end of section IIIA in publication P1. Here we have focused on three aspects: The general characteristics of the microwave photocurrent and photovoltage (angle dependence, power conversion etc.), the spin wave modes that can be visualized (PSSWs and Forward-Volume modes), and the microwave photoresistance whose either AMR-based or bolometric origin are distinguished. These three aspects are presented in section 6.1 by means of publication P2, in section 6.2 by means of publication P3 and in section 6.3 by means of publication P4, respectively.

6.1 General Characteristics of the Microwave Photovoltage and Photocurrent in Out-Of-Plane Magnetized Ferromagnetic Film Stripes

For the case of a 90° out-of-plane magnetized ferromagnetic film stripe the magnetization lies normal to the film stripe axis. This is the same as for the case of the magnetization lying in-plane but also perpendicular to the film stripe ($\alpha_0 = \pm 90°$) which is described in publication P1. Analogically to

there also here the microwave photovoltage (and also the photocurrent) vanish in the exactly normal configuration. Therefore only measurements close to this case can presented but under the assumption that the misalignment changes the result only gradually. This is visualized in figure 6.1 where the microwave photovoltage of a Permalloy film stripe is displayed for several different angles between the magnetization and film normal. There, also another important property of the microwave photovoltage and photocurrent becomes visible, namely their bipolar symmetry around symmetry configurations. This was found in in-plane magnetized ferromagnetic films, too, for the cases that the angle between the magnetization and the stripe direction takes the values $\alpha_0 \approx 0°$, $\alpha_0 \approx \pm 90°$ and $\alpha_0 \approx 180°$ (compare figure 10 in publication P1).

The major distinction of the microwave photovoltage and photocurrent in normally magnetized ferromagnetic films to those in in-plane magnetized ones is that the orientation of the magnetization with respect to the ferromagnetic film plane is different - although it might be the same with respect to the stripe axis (namely for $\alpha_0 = \pm 90°$). This results in very different static and dynamic magnetic properties of the film (compare sections 2.5.1 and 2.5.2), especially in a much higher resonance magnetic field - for the FMR as well as for the PSSWs - in the case of normal magnetization. For us this has the advantage that consequently the resonance frequency is much lower and thus, for example, more orders of the PSSW modes can be observed which will be analyzed in detail in publication P3. However, here we will first concentrate on the exceptional microwave photocurrent and photovoltage properties of normally magnetized ferromagnetic films by presenting publication P2.

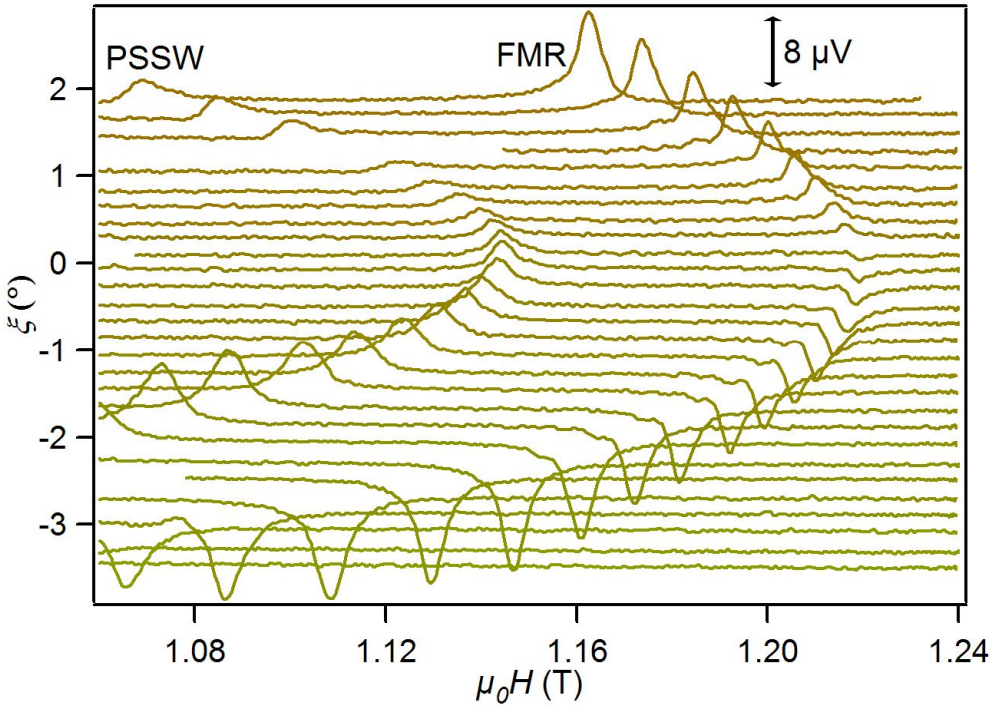

Figure 6.1: Waterfall diagram displaying the angle ξ dependence of the microwave photovoltage in a normally magnetized, 140 nm thick Permalloy film stripe at a microwave frequency of $f = 6$ GHz and a microwave generator output power of 316 mW. The angle ξ represents the angular deviation from the exact normal magnetization case. The FMR and a standing spin wave perpendicular to the ferromagnetic film (PSSW) are observed. The measurement is from an early stage of our refinement of the setup. That is why the angle ξ represents neither a rotation of the stripe around its axis nor around its perpendicular due to the coarse sample mounting. Therefore a clear aggregation of the whole angle dependence of the photovoltage as presented in publication P2, where the parallel and perpendicular angle (α and β) are distinguished, cannot be achieved here. However, a nice demonstration of the critical angle dependence of the microwave photovoltage is provided. Especially the bipolar symmetry of the signal which was also observed in publication P1 and P2 is visible for the FMR whose photovoltage reverses its sign at $\xi = 0°$.

6.1.1 P2: Realization of a Room-Temperature Spin Dynamo: The Spin Rectification Effect

Y. S. Gui, N. Mecking, X. Zhou, Gwyn Williams, and C.-M. Hu

Phys. Rev. Lett **98**, 107602 (2007)

PRL 98, 107602 (2007) PHYSICAL REVIEW LETTERS week ending 9 MARCH 2007

Realization of a Room-Temperature Spin Dynamo: The Spin Rectification Effect

Y. S. Gui, N. Mecking, X. Zhou, Gwyn Williams, and C.-M. Hu*

Department of Physics and Astronomy, University of Manitoba, Winnipeg, Canada R3T 2N2

(Received 18 October 2006; published 9 March 2007)

We demonstrate a room-temperature spin dynamo where the precession of electron spins in ferromagnets converts energy from microwaves to a bipolar current of electricity. The current/power ratio is at least 3 orders of magnitude larger than that found previously for spin-driven currents in semiconductors. The observed bipolar nature and intriguing symmetry are fully explained by the spin rectification effect via which the nonlinear combination of spin and charge dynamics creates dc currents.

DOI: 10.1103/PhysRevLett.98.107602 PACS numbers: 76.50.+g, 73.50.Pz, 84.40.−x, 85.75.−d

There is currently great interest in generating dc currents via spin dynamics [1–4]. The significance is twofold: On the one hand, it provides electrical means for investigating spin dynamics, while on the other hand, it may pave the way for designing new spin sources for spintronic applications. In semiconductor materials with spin-orbit coupling, both aspects have been demonstrated [3–5]. Progress with ferromagnetic metals (FM) has been achieved using magnetic multilayers [1,2]. Very recently, a few groups [6,7] have begun to develop techniques for electrical detection of spin resonances in a FM single layer. Understanding the dc effects in a FM single layer is crucial for clarifying whether spin pumping effects might exist in magnetic multilayers [7,8]. Until now, in contrast to the case for semiconductors [3,4], the important question of how to effectively generate dc currents from a single FM remained unclear. This leaves our understanding of the interplay between spin dynamics and electrostatic response incomplete, as evidenced in the different views represented in recent work [7,8].

In this Letter, we present both experimental and theoretical answers to this question. A spin dynamo is constructed which generates dc currents via spin dynamics. The observed bipolar nature and intriguing symmetry allow us to unambiguously identify the origin of this phenomenon as the spin rectification effect. To give a simple picture, we begin with the well-known optical rectification effect, which occurs in nonlinear media with large second-order susceptibility. Here the optical response to the product of time-dependent electric fields $e_0 \cos(\omega t)$ is governed by the trigonometric relation: $\cos(\omega_1 t)\cos(\omega_2 t) = \{\cos[(\omega_1 - \omega_2)t] + \cos[(\omega_1 + \omega_2)t]\}/2$. If the frequencies $\omega_1 = \omega_2$, the terms with difference and sum frequencies cause optical rectification and second harmonic generation, respectively. A similar nonlinear dynamic response to the product of rf electric and magnetic fields is the origin of the spin rectification effect, investigated here by using a spin dynamo.

The spin dynamo we constructed is sketched in Figs. 1(b) and 1(c). It is the microscopic counterpart of Faraday's dynamo, shown in Fig. 1(a). Both devices generate dc currents in a static magnetic field, but the rotational motion of a macroscopic copper plate in Faraday's dynamo is replaced by microscopic spin precession in the spin dynamo. The device is based on a Permalloy (Py) microstrip (typically 2.45 mm × 20 μm × 137 nm) placed in the slot between the ground and signal strips of a coplanar waveguide (CPW) [9]. From anisotropic magnetoresistance (AMR) and ferromagnetic resonance (FMR) measurements, the following material parameters have been determined for the Py strip: the conductivity $\sigma = 3 \times 10^4\ \Omega^{-1}\,\mathrm{cm}^{-1}$, the magnetoanisotropy $\Delta\rho/\rho = 0.019$, the saturation magnetization $\mu_0 M_0 = 1.0$ T, and the demagnetization factors $N_x \approx 0$, $N_y \approx 0.007$, and $N_z \approx 0.993$. Here μ_0 is the permeability of vacuum. The coordinate system is shown in Fig. 1(c). The CPW is deposited with Au/Ag/Cr layers (5/550/5 nm) on top of a semi-insulating GaAs substrate and is impedance matched to 50 Ω. The dimensions of the CPW are 150 and 100 μm in width for the strips and the slots, respectively. As sketched in Fig. 1(b), by setting the device in an electromagnet and feeding the CPW with microwaves using a conventional microwave power generator, dc currents

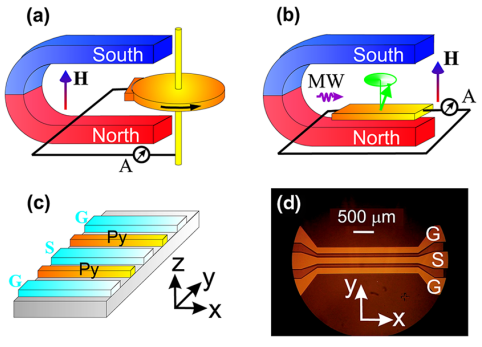

FIG. 1 (color online). (a) Faraday's dynamo with a revolving copper disk converts energy from rotation to a current of electricity. (b) Spin dynamo with a FM strip converts energy from spin precession to a bipolar current of electricity. (c) Diagram of the spin dynamo structure with Py strips placed in slots between the ground (G) and signal (S) lines of a coplanar waveguide. (d) Top view micrograph of a device.

PRL 98, 107602 (2007) PHYSICAL REVIEW LETTERS week ending 9 MARCH 2007

are generated in the Py strip at room temperature. To preserve the symmetry of the CPW, two identical Py microstrips are inserted in both slots. They are measured independently, and the same effect is found. Several spin dynamos with different Py thicknesses have been measured in various configurations. The data reported here have been rendered, both experimentally and theoretically, to convey the most significant aspects of the observed phenomena. For the same purpose, a special sample holder has been constructed that enables the spin dynamo to rotate about both the x and the y axes with an angular resolution approaching 0.01°.

Figure 2 demonstrates the production of bipolar dc currents. The microwave frequency is set at 5.4 GHz. The current I flowing along the x axis is measured using a current amplifier while sweeping the magnetic field H applied nearly perpendicular to the Py strip. We define α and β as the small angles of the field direction tilted away from the z axis towards the x and y axes, respectively. As shown in Fig. 2(a), when β is set to zero, the current $I(\alpha, H)$ measured at $\alpha = -1°$ shows a positive peak and a negative dip. The current rapidly diminishes when α is tuned to zero and then changes polarity when α becomes positive [Fig. 2(b)]. The same bipolar behavior holds true for the current $I(\beta, H)$ measured at $\alpha = 0$ and plotted in Figs. 2(c) and 2(d), except that its polarity also changes upon reversing the direction of the applied magnetic field. In addition, the sharp features in Figs. 2(a) and 2(b) disappear in Figs. 2(c) and 2(d). The insets in Fig. 2 summarize the angular dependence of the maximum bipolar current, measured by using standard lock-in techniques to enhance the signal/noise ratio at extremely small angles.

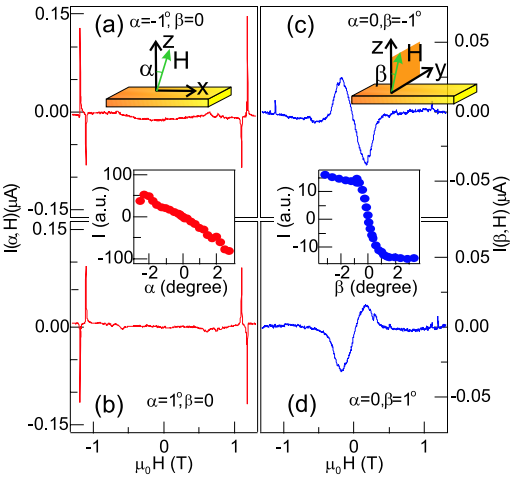

FIG. 2 (color online). Bipolar dc currents measured as a function of the magnetic field H applied with angles (a) $\alpha = -1°$, $\beta = 0$, (b) $\alpha = 1°$, $\beta = 0$, (c) $\alpha = 0$, $\beta = -1°$, and (d) $\alpha = 0$, $\beta = 1°$. The microwave frequency is fixed at 5.4 GHz. The insets summarize the angular dependence of the maximum current measured at $H < 0$.

The curious results of Fig. 2 can be summarized with the following observed bipolar symmetry:

$$I(\alpha, H) = -I(-\alpha, H) = I(\alpha, -H) \quad \text{for } \beta = 0;$$
$$I(\beta, H) = -I(-\beta, H) = -I(\beta, -H) \quad \text{for } \alpha = 0. \tag{1}$$

The sharp features in the $I(\alpha, H)$ trace suggest a resonant nature, which is confirmed by frequency dependence measurements. At higher frequencies, up to four resonances are observed. For $|H| > M_0$, the measured resonant relations, plotted in Fig. 3(a), follow the dispersion of standing spin waves (SSW) in Py films [10], given by $\omega = \gamma(|H| - M_0 + 2Ak^2/\mu_0 M_0)$. Here $k = p\pi/d$ is the wave vector with the values of p determined by the number of half-wavelengths in the Py strip with a thickness d. The solid lines in Fig. 3(a) are calculated using a gyromagnetic ratio $\gamma = 181\mu_0$ GHz/T and an exchange constant $A = 1.22 \times 10^{-11}$ N for Py [10]. Four modes with $p = 0$, 2, 3, and 4 are determined from the observed resonances, which indicates an intermediate pinning condition [11]. With $|H| < M_0$, the dispersion for SSW was previously unclear, due partially to the experimental challenge of detecting spin waves in a single Py microstrip. However, a similar field curve with a sharp cusp corresponding to the magnetic anisotropy was observed for the FMR [12]. Here, in the situation with $\beta = 0$, $\mathbf{M}$ rotates with increasing H from the easy axis parallel to the x axis towards the direction of $\mathbf{H}$. When α is small, we find that the solution of the magneto-

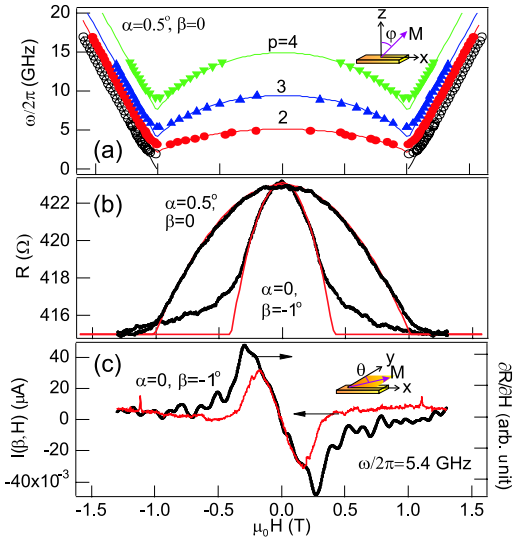

FIG. 3 (color online). (a) The measured frequency variation (marks) of the resonant features in the $I(\alpha, H)$ trace in comparison with the calculated dispersions (solid curves) for SSW. (b) AMR trace $R(H)$ measured (thick curves) and calculated (thin curves) at $\alpha = 0.5°$, $\beta = 0$ and $\alpha = 0$, $\beta = -1°$. (c) Current trace $I(\beta, H)$ measured at $\alpha = 0$, $\beta = -1°$ and 5.4 GHz (thin curve) in comparison with the field derivative of the AMR trace $\partial R(H)/\partial H$ (thick curve).

PRL 98, 107602 (2007) PHYSICAL REVIEW LETTERS week ending 9 MARCH 2007

static problem gives $\cos\varphi \approx H\cos\alpha/M_0$, where the angle φ shown in Fig. 3(a) describes the direction of $\mathbf{M}$ with respect to the hard z axis. This simple relation is confirmed by the AMR measured at $\beta = 0$, plotted in Fig. 3(b), which is well represented by $R(H) = R(\infty)[1 + (\Delta\rho/\rho)\sin^2\varphi]$. By noticing the apparent similarity between the measured SSW dispersion and the AMR trace shown in Figs. 3(a) and 3(b), respectively, we suggest an empirical expression describing the SSW at $|H| < M_0$, given by $\omega = 2\gamma(Ak^2/\mu_0 M_0)\sqrt{1 + (4\pi/p)\sin^2\varphi}$, which well describes the measured dispersions.

It follows, therefore, that the spin dynamo is an ideal device for electrically detecting spin excitations in FM microstructures. In order to focus on the characteristics of the spin rectification effect, we leave the interesting physics of the spin excitation to a later paper and continue here by studying $I(\beta, H)$ measured at $\alpha = 0$. Since $\mathbf{H}$ in this case is tilted towards the y axis by a small angle β, and because $N_x \ll N_y \ll N_z$ for the long Py strip, we make an approximation to simplify the otherwise complicated magnetostatic problem. With increasing H, we assume $\mathbf{M}$ rotates first from the easy x axis towards the y axis before it moves out of the xy plane towards the direction of $\mathbf{H}$. Physically, this means the Py strip is much easier to magnetize along the y axis than the z axis. By describing the direction of $\mathbf{M}$ with the angle θ measured with respect to the y axis as shown in Fig. 3(c), we find $\cos\theta = H/M_1$ for $|H| < M_1$, and $\theta \approx 0$ for $|H| > M_1$, where $M_1 \equiv N_y M_0/\sin\beta$. As shown in Fig. 3(b), our approximation is justified by the AMR trace measured at $\alpha = 0$ and $\beta \approx -1°$, which agrees well with the curve calculated from $R(H) = R(\infty)[1 + (\Delta\rho/\rho)\sin^2\theta]$ for $|H| < M_1 \approx 0.4$ T. In this field range, we find that the current $I(\beta, H)$ partially follows $\partial R(H)/\partial H$. This comparison is shown in Fig. 3(c).

All of these results indicate that the current is induced by the dynamics of $\mathbf{M}$, as demonstrated by the following arguments on the nature of the spin rectification effect.

Under internal magnetic ($\mathbf{H}_i$) and electric ($\mathbf{E}$) fields, the magnetostatic response of the Py strip is determined by $\mathbf{M} = \hat{\chi}_0\mathbf{H}_i$ via the static permeability tensor $\hat{\chi}_0$, while the electrostatic response is described [13] by the generalized Ohm's equation $\mathbf{J} = \sigma\mathbf{E} - R_A(\mathbf{J}\cdot\mathbf{M})\mathbf{M} + \sigma R_0\mathbf{J}\times\mathbf{H}_i + \sigma R_1\mathbf{J}\times\mathbf{M}$. This equation takes into account spin-charge coupling effects phenomenologically via the nonlinear terms. Here the second term describes magnetoanisotropy via the AMR coefficient $R_A = \Delta\rho/\rho M_0^2$, which we have used to calculate the AMR trace $R(H)$. The last two terms describe the Hall effect with the ordinary and extraordinary Hall coefficients given by $R_0 = -1.9\times10^{-8}\ \Omega\,\mathrm{cm/T}$ and $R_1 \approx 3.3\times10^{-8}\ \Omega\,\mathrm{cm/T}$, respectively [14]. Dynamic responses of the Py strip to the rf magnetic ($\mathbf{h}$) and electric ($\mathbf{e}$) fields are given by $\mathbf{m} = \hat{\chi}\mathbf{h}$ and $\mathbf{j} = \hat{\sigma}\mathbf{e}$, respectively. Here the high-frequency permeability and conductivity tensors $\hat{\chi}$ and $\hat{\sigma}$ determine the dynamic spin accumulation $\mathbf{m}$ and the eddy current $\mathbf{j}$, respectively. If static and dynamic fields coexist, the nonlinear effects couple not only the magneto and electric responses but also the static and dynamic ones. Solving the above equations self-consistently, we obtain the dc current $\mathbf{I}$ in the absence of the applied electric field as

$$\mathbf{I} = \mathbf{J}_0 - R_A(\mathbf{J}_0\cdot\mathbf{M})\mathbf{M} + \sigma R_0\mathbf{J}_0\times\mathbf{H}_i + \sigma R_1\mathbf{J}_0\times\mathbf{M}, \quad (2)$$

where $\mathbf{J}_0 = -R_A[\langle\mathbf{j}\times\mathbf{m}\rangle\times\mathbf{M} + \langle\mathbf{j}\cdot\mathbf{m}\rangle\mathbf{M}] + \sigma R_0\langle\mathbf{j}\times\mathbf{h}\rangle + \sigma R_1\langle\mathbf{j}\times\mathbf{m}\rangle$ is determined by the time average of the product of $\mathbf{j}$ and $\mathbf{m}$.

Equation (2) is the general expression for the spin rectification effect in FM. For materials with small AMR and Hall coefficients, the last three terms can be neglected, and Eq. (2) recovers an expression found earlier [15]. For devices with special geometry, the result can be further simplified. The geometric asymmetry of the spin dynamo shown in Fig. 1(d) leads to anisotropic electric and magnetodynamic responses. The eddy current is found flowing predominantly along the x axis, so that the dominant term of the spin-induced current is

$$I \approx -2R_A M_x\langle j_x m_x\rangle. \quad (3)$$

Since the components of $\mathbf{M}$ are described by the angles α, β, φ, and θ defined before, it is straightforward to show that, if $\beta = 0$, $I(\alpha, H) \approx -2R_A M_0[|H|/(|H| - M_0)]\langle j_x m_x\rangle\sin\alpha$ for $|H| > M_0$ and $I(\alpha, H) \approx -2R_A M_0\sqrt{1 - (H/M_0)^2}\langle j_x m_x\rangle(\alpha/|\alpha|)$ for $|H| < M_0$. When $\alpha = 0$, $I(\beta, H) = 0$ for $|H| > M_0$ and $I(\beta, H) \approx 2(R_A/N_y)\langle j_x m_y\rangle H\sin\beta$ for $|H| < M_1$. From these results, the bipolar symmetry deduced for $I(\alpha, H)$ and $I(\beta, H)$ is exactly the same as summarized in Eq. (1). The result $I(\beta, H) = 0$ for $|H| > M_0$ explains the disappearance of the sharp resonances in Figs. 2(c) and 2(d). Note that, for $|H| < M_1$, $I(\beta, H)$ is quasiresonant, which combines the resonant m_y and a linear dependence on H. It is easy to show that $|I(\beta, H)|$ saturates at about $2R_A\langle j_x m_y\rangle M_0$ at small angles, and $I(\beta, H)$ follows $\partial R(H)/\partial H$ in the field dependence, which explain the results shown in Figs. 2 and 3, respectively.

It is clear, therefore, that the spin rectification effect is analogous to the optical rectification effect. The effect appears whenever spin and charge responses mix via nonlinear responses. In semiconductors, spin-orbit coupling may affect such a mixing [3,4]. In FM, the effect is nonzero due to spin-charge coupling effects. It should be noted that a few earlier works [15,16] have analyzed in great detail weak dc effects induced by FMR in FM thin films, where a pulsed voltage signal was measured by using a high-power (up to kilowatts) pulsed microwave source. Here we measure directly dc currents with different characteristics: i.e., $I(\alpha, H)$ induced resonantly by both FMR and SSW and $I(\beta, H)$ caused quasiresonantly by the combination of AMR and spin excitations. An intriguing bipolar symmetry is revealed due to the microstrip geometry. Since a film has no in-plane preferential direction, the symmetry of dc effects in the film is much more cumbersome.

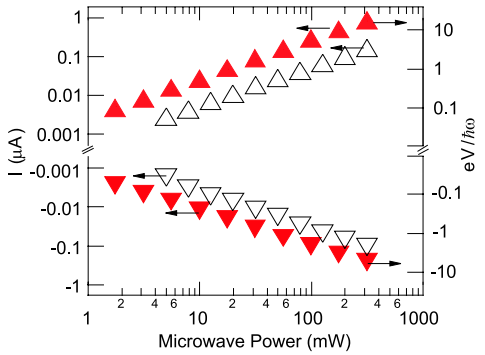

FIG. 4 (color online). The bipolar dc currents generated by both the FMR (upward triangles) and the $p = 2$ SSW (downward triangles) depend linearly on the microwave power. Open triangles are maximum currents measured at 5.4 GHz on a spin dynamo with the Py thickness $d = 137$ nm set at $\alpha = -1°$, $\beta = 0$. Solid triangles show both the closed circuit currents (left scale) and the open circuit voltages (right scale) measured at 6 GHz on a second spin dynamo with $d = 120$ nm set at $\alpha = -2°$, $\beta = 0$.

It follows from Eq. (2) that the spin-induced current and voltage are proportional to the microwave power. This is confirmed in Fig. 4, where the results for two spin dynamos measured over three decades of power range are plotted. Compared to earlier studies on semiconductors [3] and FM films [16], the current and voltage power sensitivity have been increased by 3 orders of magnitude, reaching values as high as 1 μA/W and 1 mV/W, respectively. To quantitatively evaluate the dc current enhancement, two additional experiments are performed to measure the amplitude of j_x and m_x. With an output microwave power of $P_0 = 316$ mW at the frequency of 5.4 GHz, the amplitude of $j_x = 6.5$ mA is measured via the nonresonant resistance change induced by the bolometric effect [6], and the amplitude of $\mu_0 m_x = 20$ mT is determined by the precession cone angle extracted from the microwave-induced AMR change [7]. The large value of j_x indicates the high efficiency of the microwave power coupling between CPW and Py microstrips, which dissipates more than 10% of the microwave power P_0 in the Py microstrips via the charge dynamics. The large m_x indicates the high energy density of about 0.6 J/m^3 stored by the spin dynamics, which is about 200 times larger than that carried by the rf magnetic field in the proximity of the Py microstrip. These data explain the significant enhancement of the spin rectification effect. Using Eq. (3), the dc current is calculated to be $I = 0.27$ μA at $\alpha = -1°$ with $P_0 = 316$ mW, which agrees very well with the measured result shown in Fig. 4.

Finally, we compare the spin dynamo with the spin battery proposed recently [17,18]. In the spin battery, a dc voltage generated by FMR was predicted to occur via the spin pumping effect, with a universal high-power limit given by $eV/\hbar\omega \sim 1$. In contrast, $eV/\hbar\omega \sim 18$ is observed in Fig. 4 for the spin dynamo. We anticipate that the difference is caused by lateral spin transport in the spin dynamo, which was neglected for spin battery design based on interfacial spin pumping. Experimental efforts [7,8] have been made recently to test the spin battery. Since the characteristic length scale of the spin transport in FM is only about a few nanometers, one should be cautious in distinguishing dc effects caused by spin pumping and spin rectification. Precise angular-dependent measurement is essential. One should note that the dc signal generated by the spin rectification effect, as shown in Fig. 2, may reverse its sign and change the order of its magnitude by tilting the device through only a few tenths of a degree.

In summary, we have demonstrated a spin rectification effect which generates dc currents via spin wave excitations. The unprecedented high power sensitivity and the intriguing bipolar symmetry may enable new rf signal processing and sensor applications utilizing spin dynamics. A general and consistent view is achieved for interpreting spin-driven currents, which are currently of great interest and have been studied in a variety of materials.

We thank G. Roy and G. Mollard for technical assistance and D. Heitmann, U. Merkt, and DFG for the loan of equipment. N. M. is supported by the DAAD. This work has been funded by NSERC and URGP grants awarded to C.-M. H.

*Electronic addresses: hu@physics.umanitoba.ca
http://www.physics.umanitoba.ca/~hu

[1] A. A. Tulapurkar, *et al.*, Nature (London) **438**, 339 (2005).
[2] J. C. Sankey *et al.*, Phys. Rev. Lett. **96**, 227601 (2006).
[3] S. D. Ganichev *et al.*, Nature (London) **417**, 153 (2002).
[4] C. L. Yang *et al.*, Phys. Rev. Lett. **96**, 186605 (2006).
[5] C.-M. Hu *et al.*, Phys. Rev. B **67**, 201302(R) (2003).
[6] Y. S. Gui, S. Holland, N. Mecking, and C.-M. Hu, Phys. Rev. Lett. **95**, 056807 (2005).
[7] M. V. Costache *et al.*, Phys. Rev. Lett. **97**, 216603 (2006); Appl. Phys. Lett. **89**, 232115 (2006); J. Grollier *et al.*, J. Appl. Phys. **100**, 024316 (2006).
[8] A. Azevedo *et al.*, J. Appl. Phys. **97**, 10C715 (2005); E. Saitoh *et al.*, Appl. Phys. Lett. **88**, 182509 (2006).
[9] C. P. Wen, IEEE Trans. Microwave Theory Tech. **17**, 1087 (1969).
[10] A. H. Morrish, *The Physical Principles of Magnetism* (IEEE, New York, 2001).
[11] H. Puszkarski, Prog. Surf. Sci. **9**, 191 (1979).
[12] S. V. Vonsovskii, *Ferromagnetic Resonances* (Pergamon, New York, 1966), pp. 38–39; O. Mosendz *et al.*, J. Magn. Magn. Mater. **300**, 174 (2006).
[13] J. P. Jan, in *Solid State Physics*, edited by F. Seitz and D. Turnbull (Academic, New York, 1957), Vol. 5.
[14] S. Foner, Phys. Rev. **99**, 1079 (1955).
[15] H. J. Juretschke, J. Appl. Phys. **31**, 1401 (1960).
[16] W. G. Egan and H. J. Juretschke, J. Appl. Phys. **34**, 1477 (1963).
[17] A. Brataas *et al.*, Phys. Rev. B **66**, 060404(R) (2002).
[18] Y. Tserkovnyak *et al.*, Rev. Mod. Phys. **77**, 1375 (2005).

6.2 Detection of the Forward-Volume Modes and Standing Spin Waves Perpendicular to Normally Magnetized Ferromagnetic Films

As shown in publication P2 an exceptionally strong microwave photovoltage signal (up to the mV-range) can be achieved in almost normally magnetized ferromagnetic films when using a CPW for its irradiation. In combination with our low noise level of only about 5 nV this gives us an excellent sensitivity which can be used to detect weak resonances which are usually hardly accessible in microwave experiments. One example are the confined Damon-Eshbach modes presented in section 5.4 which were previously detected using Brillouin-light scattering [37,38]. Here we want to present the corresponding modes in normally magnetized ferromagnetic films, namely confined Forward-Volume modes which are another kind of magnetostatic modes (see section 2.8.2) and have been predicted by Damon and van de Vaart [43].

Beside the Forward-Volume modes also a much more detailed discussion concerning the perpendicular standing spin waves with a special emphasis on their pinning condition is presented. Together with the results concerning the Forward-Volume modes the objective is to give an as comprehensive as possible overview over the spin wave spectrum in this measurement configuration. Thereby the CPW induced microwave photovoltage shows its extraordinary advantages, especially that it is an on-chip technique meaning that the irradiation of the specimen as well as the generation of the measurement signal takes place on the same substrate. This way, in contrast to many conventional microwave experiments, here a strong signal can be generated with a small structure, which is the major reason for our distinguished access to the large number of microscopic excitations in our Permalloy film stripe.

6.2.1 P3: Quantized Spin Excitations in a Ferromagnetic Microstrip from Microwave Photovoltage Measurements

Y. S. Gui, N. Mecking, and C.-M. Hu

Phys. Rev. Lett **98**, 217603 (2007)

PRL 98, 217603 (2007) PHYSICAL REVIEW LETTERS week ending 25 MAY 2007

Quantized Spin Excitations in a Ferromagnetic Microstrip from Microwave Photovoltage Measurements

Y. S. Gui,* N. Mecking, and C. -M. Hu†

Department of Physics and Astronomy, University of Manitoba, Winnipeg, Canada R3T 2N2

(Received 12 December 2006; published 24 May 2007)

Quantized spin excitations in a single ferromagnetic microstrip have been measured using the microwave photovoltage technique. Several kinds of spin wave modes due to different contributions of the dipole-dipole and the exchange interactions are observed. Among them are a series of distinct dipole-exchange spin wave modes, which allow us to determine precisely the subtle spin boundary condition. A comprehensive picture for quantized spin excitations in a ferromagnet with finite size is thereby established. The dispersions of the quantized spin wave modes have two different branches separated by the saturation magnetization.

DOI: 10.1103/PhysRevLett.98.217603 PACS numbers: 76.50.+g, 75.30.Et

Understanding quantized spin excitations in ferromagnets with finite size is not only pivotal for exploring nanomagnetism [1], but also essential for designing high-density magnetic memories with fast recording speed [2]. The most compelling topics that have recently attracted great interest include: the interplay between dipole-dipole and exchange interactions [3–6], the characteristics of the spin boundary conditions [7], and the evolution of spin excitations in various phases [5,8,9]. Despite general consensus on the theoretical explanation of the combined effects of dipole-dipole and exchange interactions [10,11], experiments found usually either magnetostatic modes (MSM) [12] or standing spin waves (SSW) [13], which are determined by dipole-dipole or exchange interaction, respectively. As a related problem, the impact of spin boundary conditions, which has been studied over decades on thin films with a thickness comparable to the wavelength of spin waves, remains elusive [14,15]. The most appealing quantized dipole-exchange spin wave (DESW) modes existing in laterally structured ferromagnets, which should exhibit combined characteristics of the MSM and SSW, have only been recently observed near the uniform ferromagnetic resonance (FMR) [3–6], and are therefore found to be insensitive to the exchange interaction and spin boundary conditions [10]. The lack of a comprehensive picture of spin excitations in ferromagnets with finite size is partially due to the experimental challenge of detecting spin waves in samples with shrinking dimensions, where conventional techniques such as the FMR absorption and Brillouin light scattering are approaching their sensitivity limit.

Very recently, promising new experimental techniques have been developed for studying spin dynamics: microwave photoconductivity [16] and photovoltage techniques [17], which allow electrical detection of spin excitations in ferromagnetic metals. The associate high sensitivity makes it possible to investigate the comprehensive characteristics of quantized spin excitations.

In this Letter we report investigations of quantized spin waves in a single ferromagnetic microstrip using the microwave photovoltage technique. Both the even and odd order SSWs are detected, and quantized DESWs are observed near both the FMR and the SSW. Two distinct branches of the field dispersion for the quantized spin waves are measured. The spin boundary conditions are precisely determined. And an empirical expression describing the dispersion characteristics of the complete spin excitations in the entire magnetic field range is obtained.

Our sample is a $Ni_{80}Fe_{20}$ (Permalloy, Py) microstrip, with dimensions of $l = 2.45$ mm, $w = 20$ μm, and $d = 137$ nm as shown in Fig. 1(a) in a x-y-z coordinate system. From anisotropic magnetoresistance measurements, we determine the saturation magnetization $\mu_0 M_0 = 1.0$ T. As shown in Fig. 1(b), the Py strip is inserted in the slot of a ground-signal-ground coplanar waveguide (CPW) made of an Au/Ag/Cr (5/550/5 nm) multilayer. The device is deposited on a semi-insulating GaAs substrate. By feeding the CPW with a few hundreds mW microwaves, a dc voltage V is measured along the x axis as a function of the magnetic field H applied nearly perpendicular to the Py strip. The photovoltage is induced by the spin rectification effect whose characteristics are reported elsewhere [17]. The data presented here are taken by slightly tilting the field direction away from the z axis towards the x axis by a very small angle of 0.2°, so that the x component of the magnetization M_x is nonvanishing, and the photovoltage $V \propto M_x$ has a power sensitivity approaching 0.1 mV/W.

Figure 1(c) shows the electrically detected quantized spin excitations in the Py microstrip. The sharp resonances at $H > M_0$ (labeled as FMR, S2 and S3) move to higher fields with increasing microwave frequency. At high frequencies ($\omega/2\pi > 8$ GHz) another resonance (S4) is observed (not shown) at $H > M_0$. The dispersions of these resonances follow the well-known Kittel formula for SSWs

PRL 98, 217603 (2007) PHYSICAL REVIEW LETTERS week ending 25 MAY 2007

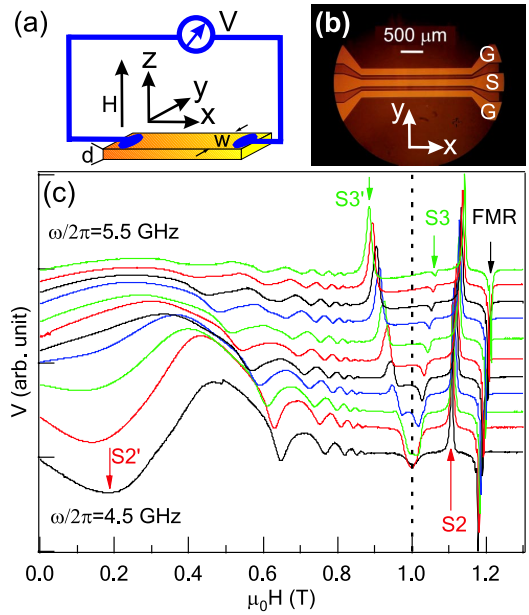

FIG. 1 (color online). (a) Schemetic drawing of the Py microstrip and the measurement circuitry. (b) Top view micrograph of a device with Py strips placed in slots between the ground (G) and signal (S) lines of a coplanar waveguide. (c) Typical photovoltage spectra measured at different microwave frequencies (from 4.5 to 5.5 GHz with a step size of 0.1 GHz). Arrows indicate FMR, SSW for the quantized number $p = 2$ (S2 and S2') and SSW for $p = 3$ (S3 and S3'), respectively. The dashed line indicates $H = M_0$. All curves are normalized with the FMR amplitude and vertically offset for clarity.

used in textbooks [15], given by: $\omega = \gamma(H - M_0 + 2Ak_z^2/\mu_0 M_0)$. The gyromagnetic ratio is determined to be $\gamma = 181\ \mu_0$ GHz/T. Here $k_z = (p - \Delta p)\pi/d$ is the wave vector, and A is the exchange stiffness constant. The quantized number p is the integer number of half wavelengths along the z direction. The correction factor Δp is bounded by $0 \leq \Delta p \leq 1$ and is determined by the boundary condition [14]

$$2A\frac{\partial \Psi_p}{\partial z} - K_s \Psi_p = 0, \tag{1}$$

where the eigenfunction of SSW has the form $\Psi_p = \alpha \sin k_z z + \beta \cos k_z z$. The constants α and β are determined by both the surface anisotropy K_s and the exchange stiffness constant A. If $\alpha/\beta \rightarrow \infty$, the spins at surfaces are completely pinned and $\Delta p = 0$. In the opposite case where $\alpha/\beta \rightarrow 0$, the spins at surfaces are totally free and $\Delta p = 1$. Based on the Kittel formula, the observed four resonances correspond to FMR ($p = 0$) and SSWs with $p = 2$, 3 and 4. However, the precise values of Δp, which are dependent on p in general, are difficult to deduce directly from the resonant positions of the SSWs. This is a long standing problem of the spin boundary condition [14,15], which not only sets up an obstacle for identifying SSWs, but also causes significant diversity [4,6,13,15] in determining important spin properties such as the value of the exchange stiffness constant A.

Before we proceed to determine precisely the value of Δp by going beyond the simple Kittel picture, we briefly highlight two interesting features observed in Fig. 1(c). One feature is that there are two branches for each SSW modes. For example, at $\omega/2\pi = 4.5$ GHz, the $p = 3$ SSW mode appears as a dip at $H = M_0$. At higher frequencies, it splits into two structures: the higher branch (dips labeled as S3) at $H > M_0$ and the lower branch (peaks labeled as S3') at $H < M_0$. Similar effects are observed for other SSWs (see Fig. 3 for the entire dispersions). The higher branch is typical for the SSWs reported earlier, where the magnetization $\mathbf{M}$ is forced to align nearly parallel to $\mathbf{H}$, and the internal field $H_i \approx H - M_0$. The lower branch is less familiar. Here, $H_i \approx 0$, and the direction of $\mathbf{M}$ is tilted away from the z axis towards the x axis by an angle φ given by $\cos\varphi \approx H/M_0$ [17]. We note that similar evolution of spin waves observed in Ni nanowires [5] and nanorings [9], were interpreted as reorientation phase transitions [8] and the transition from a "twisted bamboo" state to a "bamboo" state [9], respectively.

More interestingly, Fig. 1(c) shows a series of pronounced oscillations between S2' and S3'. The amplitude of these oscillations decreases with increasing field strength H. To the best of our knowledge, such striking oscillations, related to spin dynamics, have never been reported before. They are observed in a series of samples with different thickness in our experiment. As discussed below, the oscillations originate from the lower branch of the DESWs at $H < M_0$.

Going beyond Kittel's picture, the dispersion of DESW modes has a form given by Kalinikos and Slavin [11]:

$$\omega^2 = \gamma^2(H_i + 2Ak^2/\mu_0 M_0)(H_i + 2Ak^2/\mu_0 M_0 + M_0 F_p), \tag{2}$$

where

$$F_p = P_p + \sin^2\varphi\left(1 - P_p + \frac{M_0 P_p(1 - P_p)}{H_i + 2Ak^2/\mu_0 M_0}\right),$$

$$P_p = \frac{k_y}{2}\int_0^d \int_0^d \Psi_p(z)\Psi_p(z')\exp(-k_y \mid z - z' \mid)dzdz'.$$

Here $k^2 = k_z^2 + k_y^2$ is the wave vector, and $k_y = n\pi/w$ is the quantized wave vector along the y direction. Neglecting the exchange effect ($A = 0$) the DESW modes near the FMR reduce to the magnetostatic modes with quantized number n. In different measurement geometries, magnetostatic modes may appear either as magnetostatic forward volume modes (MSFVM), magnetostatic backward volume modes, or Damon-Eshbach modes [18]. On the other hand, neglecting the dipolar dynamic field by assuming $P_p = 0$, Eq. (2) reduces to the case for SSWs with the quantized number $p - \Delta p$.

Both MSFVMs and SSWs are detected by the photovoltage technique in our experiment. If we focus on the

PRL 98, 217603 (2007) PHYSICAL REVIEW LETTERS week ending 25 MAY 2007

low-field range of the FMR, a series of fine structures are well resolved as shown in Fig. 2(a). These are the quantized MSFVMs. The first MSFVM has an intensity of about 25% of that of the FMR and its width is narrower but comparable to that of the FMR (a few mT). The intensity of the MSFVM dramatically decreases with increasing n, while its width is not sensitive to n. The widths of both the FMR and the MSFVMs increase with microwave frequency roughly following a linear relation due to Gilbert damping [19]. Using $\Psi_0 = 1/\sqrt{d}$ one obtains $P_0 \sim k_y d/2 \sim 10^{-2} n$ in the long-wavelength limit ($k_y d \ll 1$) for MSFVMs. Consequently, the dispersions of the quantized MSFVMs are essentially independent of both the boundary conditions and the exchange interaction, as also pointed out by Sparks [10]. Figure 2(c) shows the resonance positions of the MSFVMs (symbols) as a function of the microwave frequency. The dotted lines are calculated according to Eq. (2) by adjusting the quantized number n.

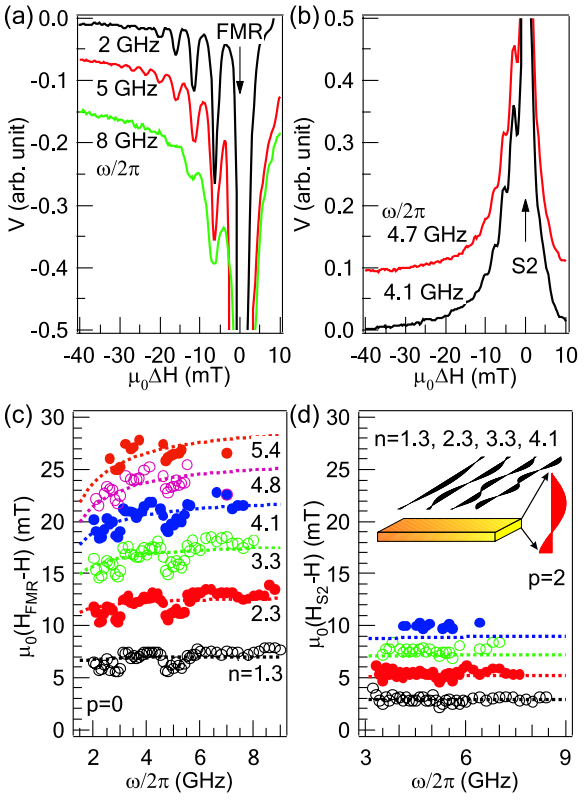

FIG. 2 (color online). (a) Quantized MSFVM and (b) DESW modes found near FMR ($p = 0$) and SSW ($p = 2$), respectively. The spectra are measured at different microwave frequencies and are vertically offset. They are normalized either to FMR or SSW ($p = 2$). (c) The measured dispersions (symbols) of the quantized MSFVM and (d) DESW modes are compared with the calculated results (dotted lines). The inset in (d) illustrates the spin waves in the microstrip quantized along both y and z directions.

The resulting values of n are 1.3, 2.3, 3.3, 4.1, 4.8, and 5.4. The spacing between the MSFVM and the FMR saturates at a value of $P_0 M_0/2$ at high frequencies when $\omega \gg \gamma P_0 M_0$.

The significance of this work is observing not only both the quantized MSFVMs and SSW modes, but also a distinct type of quantized DESW mode determined by both the quantized numbers n and $p - \Delta p$; here the interplay between the exchange and dipole-dipole interactions is significant, and the surface spin pinning must be taken into account. For $H > M_0$, as shown in Fig. 2(b), the quantized DESW modes ($p = 2$, $n \neq 0$) appear as a series of discrete resonances on the lower field side of the SSW with $p = 2$. The spacing between these modes is of the same order of magnitude as the MSFVMs. This implies that the expression for P_2 is similar to P_0 and may be of the form $k_y d$. Indeed, Fig. 2(d) shows good agreement between the measured dispersions and the calculated results using Eq. (2) with $P_2 = 2k_y d/\pi^2 \sim 4 \times 10^{-3} n$. The quantized numbers n are the same values as those for the quantized MSFVMs. It should be emphasized that the theoretical expression for P_2 depends strongly on the spin boundary conditions. For totally unpinned surface spins, one obtains $P_p = (k_y d/p\pi)^2$. For totally pinned surface spins, $P_p = 3(k_y d/p\pi)^2$ for even p, and $P_p = 4k_y d/p^2\pi^2 + 3(k_y d/p\pi)^2$ for odd p. In order to explain the observed DESW modes near the SSW with $p = 2$, unequal spin pinning at two surfaces of the Py microstrip must be taken into account. Here we assume that the spins are fully pinned only at the top surface by a thin antiferromagnetic oxide layer there, while the spins are partially pinned (described by Δp) at the bottom surface adjacent to the GaAs substrate. Using the experimental value of $P_2 = 2k_y d/\pi^2$, we deduce Δp ($p = 2$) to be 0.75. By using both Eqs. (1) and (2), we further determine $K_s \sim 8 \times 10^{-4}$ N/m and $A = 1.4 \times 10^{-11}$ N from the measured dispersion for the SSW with $p = 2$. Then, the values of $p - \Delta p$ for other SSWs are deduced from Eq. (1) to be 0, 1.25, 2.35, and 3.4 for the SSWs with $p = 1$, 2, 3, and 4. Note that the SSW for $p = 1$ determined under such a spin boundary condition coincides with the FMR as found in the experiment, and the observed four resonances at $H > M_0$ are identified as FMR ($p = 0$) and SSWs with $p = 2$, 3, and 4. The calculated intensities of SSWs based on such a spin boundary condition are in good agreement with the experimental results: The intensities of the FMR and the SSW ($p = 2$) are comparable and are both much stronger than the intensities of higher order SSWs, while the intensity of the SSW ($p = 4$) is always stronger than that of the SSW ($p = 3$). Additionally, P_3 is calculated to be about $0.05k_y d/\pi^2 \sim 10^{-4} n$, much smaller than P_2. This explains the result that DESW modes have been observed near neither branch of SSW with $p = 3$.

The precisely determined spin boundary conditions allow us to establish a complete picture for the quantized spin excitations. Figure 3 shows the dispersions of the

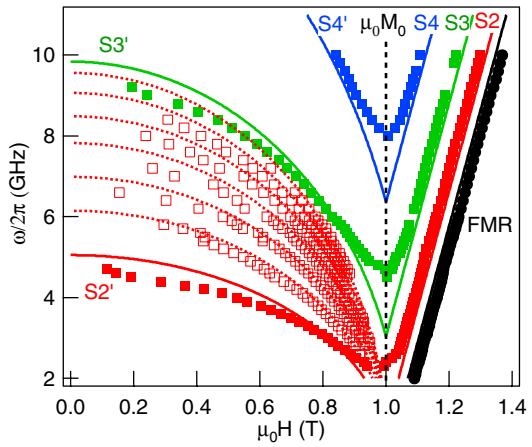

FIG. 3 (color online). Dispersions of FMR ($p = 0$) and SSWs ($p = 2$ for S2 and S2', $p = 3$ for S3 and S3', $p = 4$ for S4 and S4') measured (solid marks) in the entire magnetic field range. Open symbols show the measured lower branches of the DESWs at $H < M_0$. Upper branches at $H > M_0$, which are too close to the FMR and SSW, are not shown here for brevity but are plotted in Fig. 2 instead. Solid lines are calculated for the SSWs with $p = 0$, 2, 3, and 4. Dotted lines are calculated for the DESWs with $p = 2$. The dashed line indicates $H = M_0$.

quantized spin waves in the entire field range. At $H > M_0$, the solid symbols labeled as FMR, S2, S3, and S4 are FMR ($p = 0$) and SSWs with $p = 2$, 3, and 4. Note that the SSWs evolve into the S2', S3', and S4' at $H < M_0$. At $H > M_0$, the fine structures of the quantized MSFVMs ($p = 0$) and DESW ($p = 2$), which appear at the lower field side of the FMR and S2, respectively, are not shown in Fig. 3 for clarity. Their dispersions are displayed in Fig. 2 instead. Oscillations between S2' and S3' found in Fig. 1(c) at $H < M_0$ can now be understood as modes that evolved from the quantized DESW ($p = 2$) near S2 at $H > M_0$. Resonance positions at the minima of these oscillations are displayed by the open symbols in Fig. 3. We obtain an empirical expression describing the complete spin wave modes with the quantized numbers $(p - \Delta p,\ n)$ in the entire field range:

$$\omega^2 = \gamma^2(H_i + 2Ak^2/\mu_0 M_0 + P_p M_0) \times [H_i + 2Ak^2/\mu_0 M_0 + M_0(1 + 2n/\pi^2)(1 - P_p) \times \sin^2\varphi], \quad (3)$$

where $P_0 = k_y d/2$ and $P_2 = 2k_y d/\pi^2$. Results calculated (curves) using Eq. (3) agree well with experimental data [20]. Note that by assuming $n = 0$, Eq. (3) reduces to Eq. (2) describing SSWs in the entire H range, and by assuming $\varphi = 0$, it agrees with Eq. (2) for the DESW modes at $H > M_0$.

In summary, using a highly sensitive photovoltage technique, a comprehensive picture of quantized spin excitations in a single Py microstrip is established. The characteristics of a distinct series of DESW modes allow us to determine precisely the spin boundary condition. The results pave a new way for studying spin dynamics in ferromagnets with finite size, where both the geometrical effect and spin boundary conditions play important roles.

We thank B. Heinrich, G. Williams, H. Kunkel, and X. Z. Zhou for discussions, G. Roy for technical support, D. Heitmann, U. Merkt, and DFG for the loan of equipment. N. M. received additional support from DAAD. This work has been funded by NSERC and URGP.

*Electronic address: ysgui@physics.umanitoba.ca
†Electronic address: hu@physics.umanitoba.ca
Electronic address: http://www.physics.umanitoba.ca/~hu

[1] A. A. Tulapurkar *et al.*, Nature (London) **438**, 339 (2005); J. C. Sankey *et al.*, Phys. Rev. Lett. **96**, 227601 (2006).
[2] G. Prinz and K. Hathaway, Phys. Today **48**, No. 4, 24 (1995); S. A. Wolf *et al.*, Science **294**, 1488 (2001).
[3] J. Jorzick *et al.*, Phys. Rev. B **60**, 15 194 (1999).
[4] J. Jorzick *et al.*, Phys. Rev. Lett. **88**, 047204 (2002).
[5] Z. K. Wang *et al.*, Phys. Rev. Lett. **89**, 027201 (2002).
[6] J. P. Park *et al.*, Phys. Rev. Lett. **89**, 277201 (2002).
[7] T. G. Rappoport *et al.*, Phys. Rev. B **69**, 125213 (2004).
[8] E. V. Tartakovskaya, Phys. Rev. B **71**, R180404 (2005).
[9] Z. K. Wang *et al.*, Phys. Rev. Lett. **94**, 137208 (2005).
[10] M. Sparks, Phys. Rev. B **1**, 3831 (1970); Phys. Rev. Lett. **24**, 1178 (1970).
[11] B. A. Kalinikos and A. N. Slavin, J. Phys. C **19**, 7013 (1986).
[12] R. L. White and I. H. Solt, Phys. Rev. **104**, 56 (1956); J. F. Dillon, Jr., Phys. Rev. **112**, 59 (1958).
[13] M. H. Seavey, Jr. and P. E. Tannenwald, Phys. Rev. Lett. **1**, 168 (1958).
[14] G. T. Rado and G. R. Weertman, J. Phys. Chem. Solids **11**, 315 (1959); P. Pincus, Phys. Rev. **118**, 658 (1960); R. F. Soohoo, J. Appl. Phys. **32**, S148 (1961); R. F. Soohoo, Phys. Rev. **131**, 594 (1963).
[15] A. H. Morrish, *The Physical Principles of Magnetism* (IEEE, New York, 2001); C. Kittel, *Introduction to Solid State Physics* (John Wiley & Sons, New York, 1986) 6th ed.
[16] Y. S. Gui, S. Holland, M. Mecking, and C.-M. Hu, Phys. Rev. Lett. **95**, 056807 (2005).
[17] Y. S. Gui, N. Mecking, X. Z. Zhou, G. Williams, and C.-M, Hu, Phys. Rev. Lett. **98**, 107602 (2007).
[18] *Spin Dynamics in Confined Magnetic Structures I*, edited by B. Hillebrands and K. Ounadjela (Springer, Berlin, 2002).
[19] B. Heinrich, in *Ultrathin Mangnetic Structures III* edited by J. A. C. Bland and B. Heinrich (Springer, Berlin, 2004), Chap. 5, and references therein.
[20] The discrepancy around $H = M_0$ is caused by the simplified calculation of H_i, where we assume a perpendicular field direction by neglecting the small tilting angle of 0.2°. At $H = M_0$, this induces an deviation of 36.5 mT for H_i, which causes a resonance frequency discrepancy of about 1.05 GHz.

6.3 Microwave Photoresistance Measurements in Normally Magnetized Ferromagnetic Films

In this section we want to complete the view on the AMR-induced dc effects by discussing the microwave photoresistance in full detail which was already presented in publication P1 in section 5.1 for in-plane magnetized ferromagnetic film stripes (compare figure 6.2). Here we concentrate on the normal configuration. The AMR-induced photoreistance arises from the permanent misalignment of the precessing magnetization with respect to its equilibrium direction. If the equilibrium magnetization is aligned to the stripe and hence to the current the AMR is maximal without precession and decreases with precession. If the equilibrium magnetization lies perpendicular to the current the AMR is minimal and the opposite effect takes place: The precession raises the AMR. This bipolarity of the microwave photoresistance was already found in publication P1 for in-plane magnetized films (compare figure 6.2). Especially for a normally magnetized ferromagnetic film the current flows perpendicular to the magnetization and hence there a positive microwave photoresistance is found. This is presented in publication P4. There, the emphasis is on its interplay with the bolometric photoresistance. Based on this also a strong non-resonant background signal was identified when discussing the AMR-induced photoresistance in section IV A of publication P1. Here, beside the strong non-resonant background, we also identify a small resonant bolometric microwave photoresistance signal. To distinguish this from its AMR-induced counterpart the response time to microwave intensity changes is used. This lies for the bolometric photoresistance in the order of milliseconds and for the AMR-induced photoresistance in the order of nanoseconds.

Distinguishing the two types of photoresistance has the great advantage that the isolated AMR-induced photoresistance can be used to directly determine the cone angle of the magnetization precession [14] which is of great interest for for example FMR assisted magnetic switching [48]. Another interesting feature, especially in normally magnetized ferromagnetic films, is that the magnetization precesses circularly under FMR excitation and it has not to be accounted for corrections concerning elliptical precession (compare section IV in publication P1).

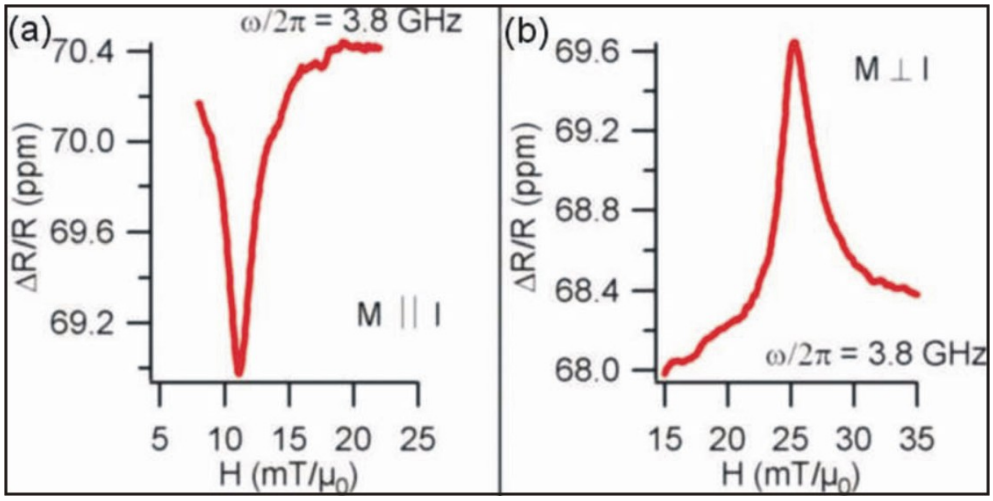

Figure 6.2: Photoresistance measurement from publication P1. For both curves the static magnetic field (and hence also the magnetization) was applied within the ferromagnetic film plane, but for a) parallel to the stripe (and hence to the dc current) and for b) perpendicular. A non-resonant background of about 70 ppm of the total dc resistance is found and identified as bolometric photoresistance. It decreases when the stripe is turned from parallel to perpendicular direction with respect to the static magnetic field. This is caused by the AMR which change R and the bolometric signal proportionally. The most important, however, is the AMR-induced resonant photoresistance signal from the FMR which shows Lorentz line shape and is bipolar with its sign depending on the direction of the magnetization $\mathbf{M}$ with respect to the dc current $\mathbf{I}$. It can be seen that its position is significantly changing when the sample is turned from parallel to perpendicular position what is caused by in-plane demagnetization effects (compare equation (31) in publication P1).

6.3.1 P4: Electrical Detection of the Ferromagnetic Resonance: Spin-Rectification versus Bolometric Effect

Y. S. Gui, N. Mecking, A. Wirthmann, L. H. Bai, and C.-M. Hu

Appl. Phys. Lett. **91**, 082503 (2007)

APPLIED PHYSICS LETTERS **91**, 082503 (2007)

Electrical detection of the ferromagnetic resonance: Spin-rectification versus bolometric effect

Y. S. Gui,[a] N. Mecking, A. Wirthmann, L. H. Bai, and C.-M. Hu
Department of Physics and Astronomy, University of Manitoba, Winnipeg, Manitoba R3T 2N2, Canada

(Received 17 May 2007; accepted 26 July 2007; published online 21 August 2007)

The authors have investigated the dc resistance change of a Permalloy microstrip under microwave irradiation. The experimental results demonstrate that both the spin-rectification and the bolometric effects significantly affect the dc resistance change, and the contribution of each can be precisely determined due to their different dependences on the modulation frequency of the microwave. Therefore, both the cone angle of magnetization precession and the thermal relaxation time following microwave heating are obtained. © *2007 American Institute of Physics*.
[DOI: 10.1063/1.2772764]

Recently, the electrical detection of the ferromagnetic resonance[1–6] (FMR) in a patterned ferromagnetic metallic single-layered structure has attracted intensive interest for the application of spintronics, where the information about the electron spin is converted to a change of electron charge properties. In general, this detectable dc charge signal is based on the bolometric and/or spin-rectification effect. The photoconductivity due to the bolometric effect is historically well known in semiconductors[7] and has been applied to the study of the spin excitations in ferromagnetic metals in the last few years.[1,2] It has been demonstrated that the spin rectification effect can cause the photocurrent/photovoltage[3,4,8,9] in a ferromagnetic metal single layer due to the coupling between the microwave (MW) induced eddy current and the dynamic magnetization. In addition, the spin-rectification effect can also induce the photoconductivity due to the coupling between the external applied dc current and the dynamic magnetization.[5,6] The photocurrent/photovoltage signal due to the spin-rectification effect vanishes for high symmetry measurement configurations.[3] However, it is still an open question regarding how to distinguish the photoconductivity due to the bolometric and spin-rectification effects, respectively. In this letter, we answer this question based on a systematic investigation of the photoconductivity of a Permalloy ($Py=Ni_{80}Fe_{20}$) microstrip under MW irradiation. We demonstrate that the measured nonresonant and resonant changes of the sample resistance are strongly dependent on the modulation frequency (f_{mod}) of the MW. This enables us to precisely discern the spin-rectification signal from the bolometric signal.

A ground-signal-ground coplanar waveguide (CPW) with a 50 Ω characteristic impendence and consisting of a Au/Ag/Cr (5 nm/550 nm/5 nm) multilayer was deposited on a semi-insulating GaAs substrate ($6\times4\times0.5$ mm^3). Two identical Py microstrips were deposited in both centers between the Au/Ag/Cr conductors to maintain the symmetry of the CPW. The dimensions of the Py microstrips were 2.45 mm × 20 μm × 137 nm with a resistance of $R=430$ Ω at room temperature. The saturation magnetization was $\mu_0 M_0=1.0$ T, the resistance change due to the anisotropic magnetoresistance (AMR) was $\Delta R_{AMR}=8.2$ Ω and the magnetoanisotropy $\Delta R_{AMR}/R=0.019$. The MW output power was pulsed with a modulation frequency f_{mod} ranging from 15 Hz to 100 kHz and the width of the MW pulse was chosen to be equal to half of a period. The MW photoconductivity was measured as a function of the applied magnetic field at room temperature using a standard lock-in technique, where the lock-in amplifier is referenced to f_{mod}. In order to suppress the photovoltage signal, which has been discussed in detail in Ref. 3, and only measure the photoconductivity, the external applied magnetic field was aligned exactly perpendicular to the sample surface with an angular resolution as precise as 0.01°. Therefore, the measured resistance change at the FMR is the sum of ΔR_b due to bolometric effect and ΔR_c due to the spin-rectification effect, i.e., $\Delta R_{res}=\Delta R_b+\Delta R_c$.

The bolometric effect relates the high frequency FMR absorption and ΔR_b by $\Delta R_b=(P_0\tau/C)\partial R/\partial T$, where P_0 is the absorbed MW power, τ is, in general, the thermal energy relaxation time, and C is the absolute heat capacity of the sample. However, as will be discussed later, ΔR_b is also strongly dependent on f_{mod} since it cannot fully relax when the modulation period is shorter than the thermal relaxation time. In this case, τ is limited by f_{mod}. Besides the resonant signal ΔR_b, a resistance change ΔR_{BG}, exists in the entire field range due to the nonresonant MW absorption and its value is independent of the external applied magnetic field H. Phenomenologically, ΔR_c, due to the spin-rectification effect, originates from the AMR, which is dependent on the angle between the magnetization **M** and the external applied dc current I_{dc}. The resonant precession causes **M** to deviate from M_0 with a cone angle of θ_c and results in the change of sample resistance. For $M_0 \perp I_{dc}$ it has been found using the first order approximation of the generalized Ohmic law[10] that $\Delta R_c=\Delta R_{AMR}\langle m_x^2\rangle/M_0^2$,[6] where m_x is the component of dynamic magnetization **m** along the strip and $\langle m_x^2\rangle$ is the time average of m_x^2. Obviously, the spin-rectification effect only affects the sample resistance near resonance, where $\langle m_x^2\rangle$ is nonzero. As a detail discussion in Ref. 6, **M** precesses elliptically, in general, because of $m_x \neq m_y$. For simplicity, in this letter we still use the concept of the cone angle θ_c, defined here as $\sin^2\theta_c=\langle m_x^2\rangle/M_0^2$ in order to quantitatively describe the experimental result.

First of all, we will show the determination of ΔR_{res} and ΔR_{BG}. Figure 1(a) focuses on the peak due to the FMR for different values of I_{dc} in order to determine the value of

[a]Electronic mail: ysgui@physics.umanitoba.ca

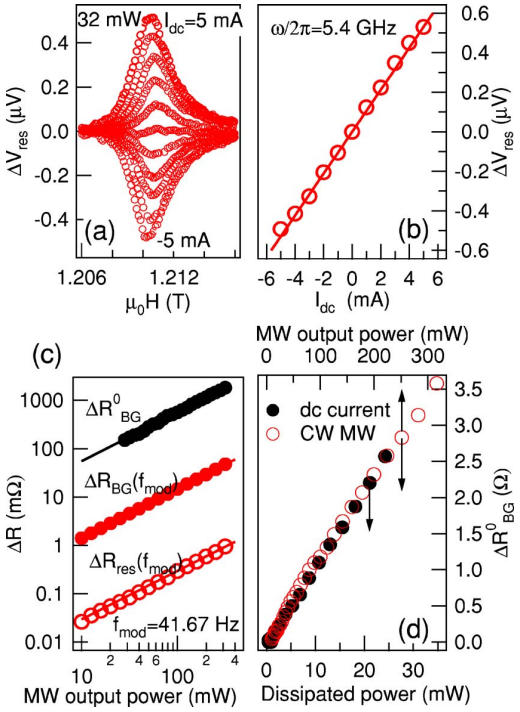

FIG. 1. (Color online) (a) FMR resonance signals for several external applied dc currents I_{dc} ranging from −5 to 5 mA in steps of 1 mA, at a MW frequency of 5.4 GHz, and an output power of 32 mW (15 dB m). The curves are vertically offset by the nonresonant background for clarity. (b) The peak height of the FMR as a function of the I_{dc} and the line is the linear fit of the experimental data. (c) ΔR_{BG} and ΔR_{res} at f_{mod}=41.67 Hz as well as ΔR^0_{BG} as a function of the MW output power. Lines are the linear fit of the experimental data. (d) The comparison between the ΔR^0_{BG} due to the dc current heating and MW continuous wave (cw) mode induced eddy current heating as a function of dissipated energy.

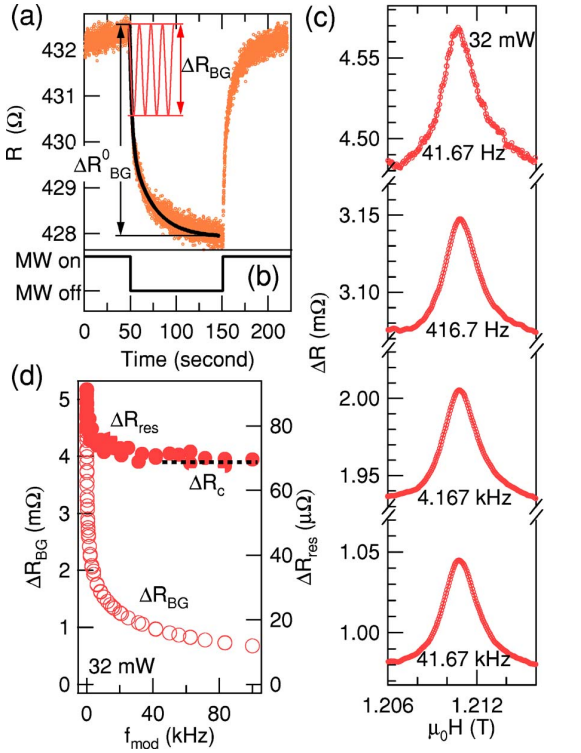

FIG. 2. (Color online) (a) Sample resistance decays at 1.216 T under MW irradiation by the periodic MW pulse shown in (b) at 316 mW (25 dB m). Symbols are experimental data and the thick solid curve is the fit using the second order exponential decay. (c) FMR signals for several modulation frequencies at a MW frequency of 5.4 GHz and an output power of 32 mW (15 dB m). (b) ΔR_{BG} and ΔR_{res} as a function of the MW modulation frequency at 32 mW. Dotted line was used to estimate ΔR_c due to the spin-rectification effect.

ΔR_{res}. The nonresonant background, which is much stronger than the resonant signal and indicates that the bolometric effect is significant, was subtracted for clarity. The MW frequency is 5.4 GHz and the MW output power is 32 mW (15 dB m) with a pulse period of 24 ms and a pulse width of 12 ms, i.e., f_{mod}=41.67 Hz. The height of the FMR peak can be well described by the Ohmic law $\Delta V_{res}=\Delta R_{res} I_{dc}$, as shown in Fig. 1(b), from which we determine ΔR_{res}=0.106 mΩ at 32 mW. ΔR_{BG} due to the nonresonant MW absorption also follows the Ohmic law with ΔR_{BG}=5.55 mΩ. It should be noted that the resonant signal of ~0.5 μV at I_{dc}=5 mA is comparable to the photovoltage signal in the absence of the dc current[3] when the external applied magnetic field H is only deviating by 0.15° from the surface normal toward the easy axis of the Py microstrip.

As expected, Fig. 1(c) shows a linear increase of ΔR_{res} and ΔR_{BG} with MW output power. In comparison, the dc resistance change of the Py microstrip ΔR^0_{BG}, i.e., ΔR_{BG} at f_{mod}=0, was measured as a function of MW output power and plotted in Fig. 1(c). In addition to the Joule heating by the MW induced Eddy current, ΔR^0_{BG} can also be caused by I_{dc}. Therefore, the precise value of ΔR^0_{BG} can be used to quantitatively determine the dissipated MW power in the sample. Figure 1(d) shows good agreement for ΔR^0_{BG} from dc current heating and MW induced Eddy current heating, respectively. This enables us to calibrate that 11% of the MW output power is dissipated in the sample. Interestingly, the resistance of a strip increases, even when only the second neighboring strip, separated by a distance of about 200 μm, is heated by I_{dc}. This implies that the Joule heating increases the temperature of the whole GaAs chip rather than only the single P_y strip.

The fact that ΔR_{BG} at f_{mod}=41.67 Hz and ΔR^0_{BG} differ by a factor of about 30, indicates that the thermal relaxation must be taken into account. Dots in Fig. 2(a) show the dc resistance response to a MW pulse with a width of 100 s [solid line in Fig. 2(b)] at 1.216 T, which is beyond resonance. Obviously, the decay of the resistance under the MW pulse is of the order of several seconds or more. Here, a second order exponential decay, the thick solid curve in Fig. 2(a), was used to fit the experimental data, which showed a good agreement with the experimental data. The two relaxation times, τ_1=2.5±0.1 s and τ_2=22±5 s, were almost identical for a series of samples with different thicknesses of Py microstrips. Since the period of the MW modulation used in Fig. 1 is only 24 ms, which is much shorter than both τ_1 and τ_2, the thermal resistance cannot fully relax and the response of the resistance under the MW irradiation is limited by the MW modulation frequency. Therefore, the resistance change detected by the lock-in technique ΔR_{BG} is, in general, much smaller than ΔR^0_{BG}, as illustrated in Fig. 2(a).

From the temperature dependent resistance of the Py microstrip (not shown here), we found that the temperature of the Py microstrip rose about ΔT=4 K at 316 mW (25 dB m) under continuous MW irradiation and the dissipated MW

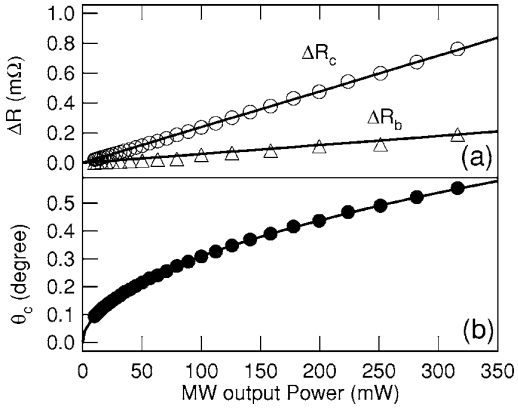

FIG. 3. (a) Resistance changes due to the bolometric effect ΔR_b at $f_{\mathrm{mod}}=41.67$ Hz and due to the spin-rectification effect ΔR_c as a function of the MW output power. Lines are the linear fit of the experimental data. (b) The cone angle of the magnetization precession as a function of the MW output power. The solid curve is the square root fit.

power in the chip was about $P_0=34.8$ mW. It is reasonable to assume that the temperature of the GaAs substrate is identical to the temperature of the Py strip because both Py and GaAs are good heat conductors. Therefore, the relaxation time can be estimated by $\tau=c\rho' V\Delta T/P_0$, where the specific heat capacity $c=0.445$ J/g K, the density $\rho'=5.32$ g/cm^3, and the volume $V=0.012$ cm^3 for the GaAs substrate. The resulting value of $\tau=3.3$ s is in good agreement with the experimental data of $\tau_1=2.5\pm0.1$ s. The origin of τ_2 is unclear at the moment.

The thermal relaxation also determines the signal near resonance, as shown in Fig. 2(c), which demonstrates how the time scale of the measurement affects the bolometric effect by tuning f_{mod} over more than three orders of magnitude. The resulting f_{mod} dependence of ΔR_{BG} and ΔR_{res} are plotted in Fig. 2(d). Both ΔR_{BG} and ΔR_{res} show similar behavior: An abrupt decrease at lower f_{mod} and a gradual decrease at higher f_{mod}. However, in contrast to ΔR_{BG} tending to zero at high f_{mod}, ΔR_{res} saturates to ΔR_c. This enables us to deduce the precise value of ΔR_c due to the spin-rectification effect from ΔR_{res}, from which we can determine the cone angle of the magnetization precession. The dependence of the cone angle on the MW output power is shown in Fig. 3(b), which follows a square root law with the largest cone angle of about 0.5° at 316 mW. This MW output/absorbed power dependence is consistent with the conventional rule of the FMR absorption experiment, where the measured signal of the FMR is linearly proportional to the amplitude of the MW field, i.e., the high frequency field h. Here, the cone angle is linearly proportional to $m=\chi h$ and χ is the high frequency susceptibility. We note that a quantitative agreement has also been found with the conventional estimation of the cone angle: At a 25 dB m (316 mW) MW output power the high frequency current flowing in the signal strip of the CPW is roughly estimated to be about 26 mA using the dissipated MW energy (35 mW) and the characteristic impendence (50 Ω). Using the average distance of 125 μm between the sample and the signal strip, $\mu_0 h\approx 42$ μT is deduced from Ampère's law and then $\mu_0 m\approx 29.4$ mT is obtain by using $\chi\approx 700$ at the FMR at 5.4 GHz.[6] This corresponds to a cone angle of circular precession of about 1.6°. Subtracting ΔR_c from ΔR_{res}, the resistance change due to the bolometric effect ΔR_b was found to be about $0.25\Delta R_c$ at $f_{\mathrm{mod}}=41.67$ Hz. It should be noted that ΔR_b is strongly dependent on f_{mod}. ΔR_b can be as high as $10\Delta R_c$ when the time scale is on the order of a second ($f_{\mathrm{mod}}\sim 1$ Hz), where ΔR_{BG} approaches ΔR_{BG}^0. This implies that in order to precisely determine the cone angle, one should measure the photoconductivity at high modulation frequency to eliminate the contribution from the bolometric effect.

In conclusion, we have investigated the resistance change of a Py microstrip under MW irradiation. The photoresistance is caused by both the bolometric and spin-rectification effects, which distinguish themselves by different characteristic time scales. The precise cone angle of the magnetization precession can be obtained at a short time scale of a few microseconds, where the AMR induced spin-rectification effect dominates the resonant photoresistance ΔR_{res}.

The authors thank G. Williams, H. Kunkel and X. Z. Zhou for discussions, D. Heitmann, U. Merkt, and DFG for the loan of the equipment. One of the authors (N.M.) was supported by a DAAD scholarship. This work has been funded by NSERC and URGP.

[1] Y. S. Gui, S. Holland, N. Mecking, and C.-M. Hu, Phys. Rev. Lett. **95**, 056807 (2005).
[2] S. T. Goennenwein, S. W. Schink, A. Brandlmaier, A. Boger, M. Opel, R. Gross, R. S. Keizer, T. M. Klapwijk, A. Gupta, H. Huebl, C. Bihler, and M. S. Brandt, Appl. Phys. Lett. **90**, 162507 (2007).
[3] Y. S. Gui, N. Mecking, X. Zhou, G. Williams, and C.-M. Hu, Phys. Rev. Lett. **98**, 107602 (2007).
[4] Y. S. Gui, N. Mecking, and C.-M. Hu, Phys. Rev. Lett. **98**, 217603 (2007).
[5] M. V. Costache, S. M. Watts, M. Sladkov, C. H. van der Wal, and B. J. van Wees, Appl. Phys. Lett. **89**, 232115 (2006).
[6] N. Mecking, Y. S. Gui, and C.-M. Hu (unpublished).
[7] F. Neppl, J. P. Kotthaus, and J. F. Koch, Phys. Rev. B **19**, 5240 (1979).
[8] H. J. Juretschke, J. Appl. Phys. **63**, 1401 (1960).
[9] W. G. Egan and H. J. Juretschke, J. Appl. Phys. **34**, 1477 (1963).
[10] J.-P. Jan, *Solid State Physics*, edited by F. Seitz and D. Turbull (Academic, New York, 1957), Vol. 5, p. 2.

Chapter 7

Summary and Outlook

Finally we want to outline our results. We have detected the microwave photovoltage, photocurrent and photoresistance in thin Permalloy film stripes. While the photovoltage and photocurrent are found to arise from rectification based on the temporal oscillations of the AMR due to magnetization precession, the microwave photoresistance is found to arise from the alteration of the AMR by the permanent misalignment of the precessing magnetization with respect to its equilibrium direction. There is, however, also a bolometric contribution in the microwave photoresistance which can be distinguished from the AMR-based due to its very different response time to changes in microwave intensity.

The applicability of the AMR-induced microwave photoresistance arises from the possibility to determine the deflection angle of the magnetization precession, which is circular if the static magnetization lies normal to the film plane and otherwise elliptical. In contrast to this the strength of the AMR-induced microwave photovoltage does not only depend on the strength of the magnetization precession amplitude but also on the microwave induced rf current in the ferromagnetic film plane. As a consequence, the microwave photovoltage can be used to determine more parameters concerning the magnetization precession, namely the direction of the exciting rf magnetic field vector, its phase and the phase of the rf magnetization with respect to the rf current. This enables us to even discuss the application of the microwave photovoltage in rf magnetic field sensing.

The magnetization precession which underlies the microwave photovoltage and photoresistance is typically realized using the coherent spin precession arising from the ferromagnetic resonance. However, also the other ferromagnetic excitations yield - yet spatially inhomogeneous - spin precession. Indeed the microwave photovoltage can be used to detect an especially large number of spin excitations due to its outstanding sensitivity. We detect, for

example, the standing spin waves perpendicular to our ferromagnetic films which have a short wavelength and whose energy is therefore dominated by the exchange interaction. These show a vast frequency difference compared to the ferromagnetic resonance.

But we also detect magnetostatic modes which have a much longer wavelength and therefore derive their energy from the dipole-dipole interaction and whose frequency is much closer to that of the ferromagnetic resonance. Concerning these in normally magnetized ferromagnetic films we detect confined Forward-Volume modes and in in-plane magnetized ferromagnetic films confined Damon-Eshbach modes whereby a large number of orders is found in both cases. It is even possible to visualize several orders of a combined dipole-exchange spin wave mode. These are arranged similarly to those of Forward-Volume modes but not attached to the ferromagnetic resonance. Instead they appear next to a perpendicular standing spin wave resonance.

In conclusion the success of our theoretical description of the ferromagnetic resonance-based microwave photovoltage and photoresistance suggests the extension of this model to the case of perpendicular standing spin waves and magnetostatic modes what could, for example, explain their line shape in detail. A first step in this direction was already done by Moller and Juretschke [7] although this was limited to a rather preliminary level with an only qualitative agreement of the theoretical with the experimental results. This is in contrast to the theoretical results of publication P1 for which also many analogies can be found concerning the spin wave-induced microwave photovoltage, for example the asymmetric line shape and the similar angle dependencies. Hence it is an interesting task for the future to establish a consistent description for the microwave photovoltage and photoresistance from spin wave resonances, too.

Bibliography

[1] S. Datta and B. Das, *Electronic analog of the electro-optic modulator*, Appl. Phys. Lett. **56**, 665 (1990).

[2] M. N. Baibich, J. M. Broto, A. Fert, F. Nguyen Van Dau, F. Petroff, P. Eitenne, G. Creuzet, A. Friederich, and J. Chazelas, *Giant Magnetoresistance of (001)Fe/(001)Cr Magnetic Superlattices*, Phys. Rev. Lett. **61**, 2472 (1988).

[3] A. A. Tulapurkar, Y. Suzuki, A. Fukushima, H. Kubota, H. Maehara, K. Tsunekawa, D. D. Djayaprawira, N. Watanabe, and S. Yuasa *Spin-torque diode effect in magnetic tunnel junctions*, Nature London **438**, 339 (2005).

[4] J. C. Sankey, P. M. Braganca, A. G. F. Garcia, I. N. Krivorotov, R. A. Buhrman, and D. C. Ralph, *Spin-Transfer-Driven Ferromagnetic Resonance of Individual Nanomagnets*, Phys. Rev. Lett. **96**, 227601 (2006).

[5] H. J. Juretschke, *Electromagnetic Theory of dc Effects in Ferromagnetic Resonance*, J. Appl. Phys. **31**, 1401 (1960);

[6] W. G. Egan and H. J. Juretschke, *DC Detection of Ferromagnetic Resonance in Thin Nickel Films*, J. Appl. Phys. **34**, 1477 (1963).

[7] W. M. Moller, and H. J. Juretschke, *Determination of Spin-Wave Boundary Conditions by dc Effects in Spin-Wave Resonance*, Phys. Rev. B **2**, 2651 (1970).

[8] M. V. Costache, M. Sladkov, S. M. Watts, C. H. van der Wal, and B. J. van Wees, *Electrical Detection of Spin Pumping due to the Precessing Magnetization of a Single Ferromagnet*, Phys. Rev. Lett. **97**, 216603 (2006).

[9] J. Grollier, M. V. Costache, C. H. van der Wal, and B. J. van Wees, *Microwave spectroscopy on magnetization reversal dynamics of nanomagnets with electronic detection*, J. Appl. Phys. **100**, 024316 (2006).

[10] E. Saitoh, M. Ueda, H. Miyajima, and G. Tatara, *Conversion of spin current into charge current at room temperature: Inverse spin-Hall effect*, Appl. Phys. Lett. **88**, 182509 (2006).

[11] A. Azevedo, L. H. Vilela Leo, R. L. Rodriguez-Suarez, A. B. Oliveira, and S. M. Rezende, *dc effect in ferromagnetic resonance: Evidence of the spin-pumping effect?*, J. Appl. Phys. **97**, 10C715 (2005).

[12] A. Yamaguchi, H. Miyajima, T. Ono, Y. Suzuki, S. Yuasa, A. Tulapurkar, and Y. Nakatani, *Rectification of radio frequency current in ferromagnetic nanowire*, Appl. Phys. Lett. **90**, 182507 (2007).

[13] A. Yamaguchi, H. Miyajima, T. Ono, Y. Suzuki, S. Yuasa, A. Tulapurkar, and Y. Nakatani, *Self-homodyne rf demodulator using a ferromagnetic nanowire*, Appl. Phys. Lett. **90**, 212505 (2007).

[14] M.V. Costache, S. M. Watts, M. Sladkov, C. H. van der Wal, and B. J. van Wees, *Large cone angle magnetization precession of an individual nanopatterned ferromagnet with dc electrical detection*, Appl. Phys. Lett. **89**, 232115 (2006).

[15] Y. S. Gui, S. Holland, N. Mecking, and C.-M. Hu, *Resonances in Ferromagnetic Gratings Detected by Microwave Photoconductivity*, Phys. Rev. Lett. **95**, 056807 (2005).

[16] L. Berger, *Emission of spin waves by a magnetic multilayer traversed by a current*, Phys. Rev. B **54**, 9353 (1996).

[17] L. Berger, *Generation of dc voltages by a magnetic multilayer undergoing ferromagnetic resonance*, Phys. Rev. B **59**, 11465 (1999).

[18] A. Brataas, Yaroslav Tserkovnyak, Gerrit E. W. Bauer, and Bertrand I. Halperin, *Spin battery operated by ferromagnetic resonance*, Phys. Rev. B **66**, 060404(R) (2002).

[19] Xuhui Wang, Gerrit E. W. Bauer, Bart J. van Wees, Arne Brataas, and Yaroslav Tserkovnyak, *Voltage Generation by Ferromagnetic Resonance at a Nonmagnet to Ferromagnet Contact*, Phys. Rev. Lett. **97**, 216602 (2006).

[20] J. N. Kupferschmidt, Shaffique Adam, and P. W. Brouwer, *Theory of the spin-torque-driven ferromagnetic resonance in a ferromagnet/normal-metal/ferromagnet structure*, Phys. Rev. B **74**, 134416 (2006).

[21] *Electrically detected ferromagnetic resonance*, S. T. Goennenwein, S. W. Schink, A. Brandlmaier, A. Boger, M. Opel, R. Gross, R. S. Keizer, T. M. Klapwijk, A. Gupta, H. Huebl, C. Bihler, and M. S. Brandt, Appl. Phys. Lett. **90**, 162507 (2007).

[22] K. Bittkau, N. Mecking, Y. S. Gui, Ch. Heyn, D. Heitmann, and C.-M. Hu, *Photoconductivity of $In_xAl_{1x}As$ parabolic quantum wells in the optical-phonon regime*, Phys. Rev. B **71**, 035337 (2005).

[23] S. Holland, Ch. Heyn, D. Heitmann, E. Batke, R. Hey, K. J. Friedland, and C.-M. Hu, *Quantized Dispersion of Two-Dimensional Magnetoplasmons Detected by Photoconductivity Spectroscopy*, Phys. Rev. Lett. **93**, 186804 (2004)

[24] K. Bittkau, Ch. Menk, Ch. Heyn, D. Heitmann, and C.-M. Hu, *Far-infrared photoconductivity of electrons in an array of nanostructured antidots*, Phys. Rev. B **68**, 195303 (2003).

[25] C.-M. Hu, C. Zehnder, Ch. Heyn, and D. Heitmann, *THz collective spin-flip excitation of a two-dimensional electron system*, Phys. Rev. B **67**, 201302(R) (2003).

[26] L. H. Bai, Y. S. Gui, A. Wirthmann, E. Recksiedler, N. Mecking, C.-M. Hu, Z. H. Chen, and S. C. Shen, *The rf magnetic-field vector detector based on the spin rectification effect*, Appl. Phys. Lett. **92**, 032504 (2008).

[27] S. I. Kiselev, J. C. Sankey, I. N. Krivorotov, N. C. Emley, R. J. Schoelkopf, R. A. Buhrman, and D. C. Ralph, *Microwave oscillations of a nanomagnet driven by a spin-polarized current*, Nature (London) 425, 380 (2003).

[28] C. Kittel, *Introduction to Solid State Physics* (John Wiley & Sons, Inc., New York, 1986) 6th ed.

[29] A. H. Morrish, *The Physical Principles of Magnetism* (IEEE, New York, 2001).

[30] T. McGuire, and R. Potter, *Anisotropic magnetoresistance in ferromagnetic 3d alloys*, IEEE Trans. on Magn. **11**, 1018 (1975).

[31] K. L. Yau, and J. T. H. Chang, *The planar Hall effect in thin foils of Ni-Fe alloy*, J. Phys. F **1**, 38 (1971).

[32] H. Ebert, A. Vernes, and J. Banhart, *Anisotropic electrical resistivity of ferromagnetic Co-Pd and Co-Pt alloys*, Phys. Rev. B **54**, 8479 (1996).

[33] C. Kittel, *On the Theory of Ferromagnetic Resonance Absorption*, Phys. Rev. **73**, 155 (1948).

[34] L. Landau, and L. Liftshitz, Physik Z. Sowjet. **8** 153 (1935).

[35] D. Polder, *On the Theory of Ferromagnetic Resonance*, Philosophical Magazine **40**, 99 (1949).

[36] J. D. Jackson, *Classical Electrodynamics* (John Wiley & Sons, New York, 1998) 3rd ed.

[37] J. Jorzick, S. O. Demokritov, C. Mathieu, B. Hillebrands, B. Bartenlian, C. Chappert, F. Rousseaux, and A. N. Slavin, *Brillouin light scattering from quantized spin waves in micron-size magnetic wires*, Phys. Rev. B **60**, 15194 (1999).

[38] *Spin Dynamics in Confined Magnetic Structures I* edited by B. Hillebrands and K. Ounadjela (Spinger, Berlin, 2002).

[39] C. Herring, and C. Kittel, *On the theory of Spin Waves in Ferromagnetic Media*, Phys. Rev. **81**, 869 (1950).

[40] L. R. Walker, *Magnetostatic Modes in Ferromagnetic Resonance*, Phys. Rev. **105**, 390 (1957).

[41] B. A. Kalinikos, and A. N. Slavin, *Theory of dipole-exchange spin wave spectrum for ferromagnetic films with mixed exchange boundary conditions*, J. Phys. C **19**, 7013 (1986).

[42] R. W. Damon, and J. R. Eshbach, *Magnetostatic Modes of a Ferromagnetic Slab*, J. Appl. Phys. **31**, S104 (1960).

[43] R. W. Damon, and H. van de Vaart, *Propagation of Magnetostatic Spin Waves at Microwave Frequencies in a Normally-Magnetized Disk*, J. Appl. Phys. **11**, 3453 (1965).

[44] N. D. J. Miller, *Magnetostatic volume wave propagation in a dielectric layered structure*, Phys. Stat. Sol. (a) **37**, 83 (1976).

[45] B. S. Guru and H. R. Hiziroglu, *Electromagnetic Field Theory Fundamentals, 2nd Edition* (Cambridge University Press, 2004).

[46] P.W. Anderson and H. Suhl, *Instability in the Motion of Ferromagnets at High Microwave Power Levels*, Phys. Rev. **100**, 1788 (1955).

[47] T. L. Gilbert, *A Phenomenological Theory of Damping in Ferromagnetic Materials*, IEEE Trans. on Magn. **40**, 3443 (2004).

[48] C. Thirion, W. Wernsdorfer, and D. Mailly, *Switching of magnetization by nonlinear resonance studied in single nanoparticles*, Nat. Mater. **2**, 524 (2003)

Conference Contributions

- N. Mecking, K. Bittkau, Y.S. Gui, Ch. Heyn, D. Heitmann und C.-M. Hu, *Photoleitungsspektroskopie an InAlAs/InAs/InAlAs/GaAs- Halbleiterstrukturen im Bereich der GaAs-Reststrahlenbande*, DPG Frühjahrstagung, Berlin (2005).

- K. Rachor, S. Groth, N. Mecking, A. Wittmann, C. Heyn, and D. Heitmann, *AFM Nanolithography on metallic and semiconductor structures*, 14th International Winterschool on New Developments in Solid State Physics in Mauterndorf, Austria (2006).

- K. Rachor, S. Groth, N. Mecking, C. G. v. Westarp, C.-M. Hu, Ch. Heyn, and D.Heitmann, *FIR Spectroscopy of Nano Structures fabricated fabricated by AFM Lithography*, DPG Frühjahrstagung, Dresden (2006).

- C.-M. Hu, Y. S. Gui, N. Mecking, A. Wirthmann, C. Zehnder, K. Bittkau, S. Holland, and D. Heitmann, *Spin, Charge and Lattice Excitations Investigated by Photoconductivity Spectroscopy*, Joint 31st International Conference on Infrared and Millimeter Waves and 14th International Conference on Terahertz Electronics, Shanghai, China (2006).

- S. Groth, K. Rachor, N. Mecking, T. Krohn, C. G. v. Westarp, Ch. Heyn, and D. Heitmann, *FIR Spectroscopy of Nanostructured Meandering Conducting Stripes Fabricated by AFM Nanolithography*, DPG Frühjahrstagung, Regensburg (2007).

- Nikolai Mecking, Yongsheng Gui, Tobias Krohn, Niels Ruhe, Detlef Heitmann, And Can-Ming Hu, *AMR-induced microwave photoresistance and photovoltage in ferromagnetic films*, 15th International Winterschool on New Developments in Solid State Physics in Bad Hofgastein, Austria (2008).

- Nikolai Mecking, Yongsheng Gui, and Can-Ming Hu, *AMR-induced microwave photoresistance and photovoltage in ferromagnetic films*, DPG Frühjahrstagung, Berlin (2008).

- Tobias Krohn, Nikolai Mecking, André Wirthmann, and Detlef Heitmann, *Photovoltage Induced by Microwave Radiation on AlGaAs/GaAs Hall Bars*, DPG Frühjahrstagung, Berlin (2008).

Publications

- K. Bittkau, N. Mecking, Y. S. Gui, Ch. Heyn, D. Heitmann, and C.-M. Hu, *Photoconductivity of $In_xAl_{1-x}As$ parabolic quantum wells in the optical-phonon regime*, Phys. Rev. B **71**, 035337 (2005).

- Y. S. Gui, S. Holland, N. Mecking, and C.-M. Hu, *Resonances in Ferromagnetic Gratings Detected by Microwave Photoconductivity*, Phys. Rev. Lett. **95**, 056807 (2005).

- Y. S. Gui, N. Mecking, X. Zhou, Gwyn Williams, and C.-M. Hu, *Realization of a Room-Temperature Spin Dynamo: The Spin Rectification Effect*, Phys. Rev. Lett **98**, 107602 (2007).

- Y. S. Gui, N. Mecking, and C.-M. Hu, *Quantized Spin Excitations in a Ferromagnetic Microstrip from Microwave Photovoltage Measurements*, Phys. Rev. Lett **98**, 217603 (2007).

- Y. S. Gui, N. Mecking, A. Wirthmann, L. H. Bai, and C.-M. Hu, *Electrical Detection of the Ferromagnetic Resonance: Spin-Rectification versus Bolometric Effect*, Appl. Phys. Lett. **91**, 082503 (2007).

- N. Mecking, Y. S. Gui, and C.-M. Hu, *Microwave Photovoltage and Photoresistance Effects in Ferromagnetic Microstrips*, Phys. Rev. B **76**, 224430 (2007).

- L. H. Bai, Y. S. Gui, A. Wirthmann, E. Recksiedler, N. Mecking, C.-M. Hu, Z. H. Chen, and S. C. Shen, *The rf magnetic-field vector detector based on the spin rectification effect*, Appl. Phys. Lett. **92**, 032504 (2008).

Acknowledgements

I would like to thank the following people and institutions who supported me during my work:

- Prof. Dr. Detlef Heitmann for giving me the opportunity to prepare my dissertation in his group, enabling my stay abroad and supporting me after my return.
- Prof. Dr. Can-Ming Hu for being the referee for my dissertation, for supervising me during my stay at the University of Manitoba and for his tremendous support at all times in Winnipeg as well as in Hamburg.
- Prof. Dr. Oepen for being the referee for my disputation and for supporting the application for my stay abroad at the University of Manitoba.
- Dr. Yongsheng Gui for the very productive cooperation and his excellent supervising of my work.
- Dr. André Wirthmann and Lihui Bai for the successful cooperation in the group of Can-Ming Hu.
- Gilles Roy for the excellent technical assistance and guidance during my stay at the University of Manitoba and Grant Mollard for the important support from his workshop.
- The Deutsche Akademische Austauschdienst DAAD for enabling and financing my stay at Winnipeg.
- Kevin Rachor, Tobias Krohn, Steffen Groth, Carsten Graf von Westarp, Thomas Raab, and Carsten Zehnder from the FIR group for their help.
- Group H for the good atmosphere during my working at the Institut für angwandte Physik.
- The mechanical, electrical and Helium shop at the Institut für angewandte Physik.
- My girlfriend Olga for proof reading this work.
- My parents and brother for their support.